

**AEDC-TR-79-39**

C.1

**ARCHIVE COPY  
DO NOT LOAN**



**Application of the Multistage Axial-Flow Compressor  
Time-Dependent Mathematical Modeling Technique  
to the TF41-A-1 Modified (Block 76) Compressor**

C. E. Chamblee  
ARO, Inc.

**September 1979**

**Final Report for Period January 1978 — March 1979**

Approved for public release; distribution unlimited.

Property of U. S. Air Force  
AEDC LIBRARY  
F40500-77-C-0003

**ARNOLD ENGINEERING DEVELOPMENT CENTER  
ARNOLD AIR FORCE STATION, TENNESSEE  
AIR FORCE SYSTEMS COMMAND  
UNITED STATES AIR FORCE**

AEDC TECHNICAL LIBRARY



5 0720 00034 3915

## NOTICES

When U. S. Government drawings, specifications, or other data are used for any purpose other than a definitely related Government procurement operation, the Government thereby incurs no responsibility nor any obligation whatsoever, and the fact that the Government may have formulated, furnished, or in any way supplied the said drawings, specifications, or other data, is not to be regarded by implication or otherwise, or in any manner licensing the holder or any other person or corporation, or conveying any rights or permission to manufacture, use, or sell any patented invention that may in any way be related thereto.

Qualified users may obtain copies of this report from the Defense Documentation Center.

References to named commercial products in this report are not to be considered in any sense as an indorsement of the product by the United States Air Force or the Government.

This report has been reviewed by the Information Office (OI) and is releasable to the National Technical Information Service (NTIS). At NTIS, it will be available to the general public, including foreign nations.

## APPROVAL STATEMENT

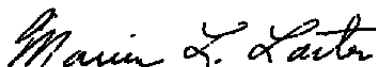
This report has been reviewed and approved.



SALVADOR REZA, 2d Lt, USAF  
Project Manager, Analysis and Evaluation Division  
Directorate of Test Engineering

Approved for publication:

FOR THE COMMANDER



MARION L. LASTER  
Director of Test Engineering  
Deputy for Operations

# UNCLASSIFIED

REPORT DOCUMENTATION PAGE		READ INSTRUCTIONS BEFORE COMPLETING FORM
1. REPORT NUMBER <b>AEDC-TR-79-39</b>	2. GOVT ACCESSION NO.	3. RECIPIENT'S CATALOG NUMBER
4. TITLE (and Subtitle) <b>APPLICATION OF THE MULTISTAGE AXIAL-FLOW COMPRESSOR TIME-DEPENDENT MATHEMATICAL MODELING TECHNIQUE TO THE TF41-A-1 MODIFIED (BLOCK 76) COMPRESSOR</b>	5. TYPE OF REPORT & PERIOD COVERED <b>Final Report for Period - January 1978 - March 1979</b>	
	6. PERFORMING ORG. REPORT NUMBER	
7. AUTHOR(s) <b>C. E. Chamblee, ARO, Inc., a Sverdrup Corporation Company</b>	8. CONTRACT OR GRANT NUMBER(s)	
9. PERFORMING ORGANIZATION NAME AND ADDRESS <b>Arnold Engineering Development Center/DOTA Air Force Systems Command Arnold Air Force Station, Tennessee 37389</b>	10. PROGRAM ELEMENT, PROJECT, TASK AREA & WORK UNIT NUMBERS <b>Program Element 27121F</b>	
11. CONTROLLING OFFICE NAME AND ADDRESS <b>Arnold Engineering Development Center/DOS Air Force Systems Command Arnold Air Force Station, Tennessee 37389</b>	12. REPORT DATE <b>September 1979</b>	
	13. NUMBER OF PAGES <b>97</b>	
14. MONITORING AGENCY NAME & ADDRESS (if different from Controlling Office)	15. SECURITY CLASS. (of this report)  <b>UNCLASSIFIED</b>	
	15a. DECLASSIFICATION/DOWNGRADING SCHEDULE <b>N/A</b>	
16. DISTRIBUTION STATEMENT (of this Report)  <b>Approved for public release; distribution unlimited.</b>		
17. DISTRIBUTION STATEMENT (of the abstract entered in Block 20, if different from Report)		
18. SUPPLEMENTARY NOTES  <b>Available in DDC</b>		
19. KEY WORDS (Continue on reverse side if necessary and identify by block number) <b>high pressure compressors performance (engineering) TF41-A-1 turbofan engines mathematical models</b>		
20. ABSTRACT (Continue on reverse side if necessary and identify by block number) <b>The overall objective of the work described herein was to construct a validated mathematical model of the high-pressure compressor of the TF41-A-1 turbofan engine and to provide thereby a new analysis tool for assessing influences of external disturbances and com- pressor modifications on performance and stability. These objec- tives were accomplished through the development of a one- dimensional, steady-state TF41-A-1 compressor mathematical model</b>		

# UNCLASSIFIED

# UNCLASSIFIED

## 20. Abstract (Continued)

for stability assessment with undisturbed flow, and a three-dimensional, time-dependent TF41-A-1 compressor mathematical model for analysis of distorted inflows and transient and dynamic disturbances. Example problems and comparisons to experimental results are presented for both models. The problems using the one-dimensional, steady-state model consisted of determination of the steady-state stability limits (surge lines) with undisturbed flow for three distinct inlet guide vane schedules. Those problems using the three-dimensional, time-dependent model included determination of the stability limit (surge line) reduction caused by pure radial pressure inlet distortion, pure circumferential pressure, and pure circumferential temperature inlet distortion. The effects of rapid upward ramps of inlet temperature on compressor stability were also investigated. The TF41-A-1 compressor models computed the compressor stability limits with reasonable accuracy.

## **PREFACE**

The research reported herein was conducted by the Arnold Engineering Development Center (AEDC), Air Force Systems Command (AFSC), at the request of the Aeronautical Systems Division (ASD). The work and analysis for this research were done by personnel of ARO, Inc. (a Sverdrup Corporation Company), contract operator for AEDC, AFSC, Arnold Air Force Station, Tennessee, under ARO Project Nos. E43P-78A, E43Y-84, and E43P-79. The Air Force project manager was Lt. S. Reza, DOTA. The manuscript was submitted for publication on April 27, 1979.

The author wishes to acknowledge William F. Kimzey, ARO, Inc., for his assistance during the model development; Grant T. Patterson, ARO, Inc., for his assistance in modifying computer programs required for this effort; William R. Warwick, ARO, Inc., for his assistance in obtaining compressor stage characteristics; and Virgil K. Smith, University of Tennessee Space Institute, for assistance provided during the course of this work.

## CONTENTS

	<u>Page</u>
1.0 INTRODUCTION .....	7
2.0 TF41-A-1 TURBOFAN ENGINE ALTITUDE AEROMECHANICAL TEST AND RESULTS	
2.1 Engine Description .....	8
2.2 Instrumentation .....	9
2.3 Procedure for High-Pressure Compressor Stability Assessment .....	10
2.4 Experimental Results .....	10
3.0 DESCRIPTION OF ONE-DIMENSIONAL, STEADY-STATE MODEL	
3.1 Model Concepts .....	11
3.2 TF41-A-1 High-Pressure Compressor Steady-State Stage Characteristics .....	17
3.3 Model Verification .....	19
4.0 DESCRIPTION OF THREE-DIMENSIONAL, TIME-DEPENDENT MODEL	
4.1 Model Concepts .....	20
4.2 Three-Dimensional, Time-Dependent Model Refinements .....	23
4.3 Model Verification .....	24
5.0 SUMMARY OF RESULTS .....	27
REFERENCES .....	28

## ILLUSTRATIONS

### Figure

1. TF41-A-1 Turbofan Engine Schematic .....	31
2. Installation Schematic TF41-A-1 in Propulsion Development Test Cell (T-4) .....	32
3. TF41-A-1 (Block 76) HP Compressor Schematic .....	33
4. HP Compressor Interstage Instrumentation .....	34
5. TF41-A-1 IGV Schedules .....	35
6. Effects of IGV Schedule on TF41-A-1 HP Compressor Stability Limit at 30,000 ft, Mach Number 0.7 with Seventh-Stage Bleed Valve Closed .....	36

<u>Figure</u>	<u>Page</u>
7. Effects of IGV Schedule on TF41-A-1 HP Compressor Stability Limit at Sea-Level-Static Conditions with Seventh-Stage Bleed Valve Open .....	37
8. Surge Induced by Inbleed at $NH = 11,500$ rpm with Axial IGV Schedule .....	38
9. Radial Total Pressure Profiles with Uniform Engine Inlet Flow .....	39
10. Radial Total Temperature Profiles with Uniform Engine Inlet Flow .....	42
11. Station Locations (Computational Planes) for One- Dimensional, Steady-State Compressor Model .....	45
12. Elemental Control Volume with Application of Mass, Momentum, and Energy Conservation Principles .....	46
13. Typical Temperature and Pressure Coefficients as Functions of Flow Coefficient at Constant Rotational Speed .....	47
14. TF41-A-1 HP Compressor Stage Characteristics .....	48
15. Comparison of Model Computed Speed Characteristics and Stability Limits with Experimental Measurements at 30,000 ft, $MO = 0.7$ .....	59
16. Model Computed Effect of Corrected Rotor Speed Variation for -0.3-deg IGV Line with Axial IGV Schedule at 30,000 ft, $MO = 0.7$ .....	62
17. Comparison of Model Computed Speed Characteristics and Stability Limits with Experimental Measurements with Seventh-Stage Bleed Valve Open at sea-level-static conditions .....	63
18. Comparison of Model Computed Stage Flow Coefficients Near Compressor Stability Limit with Experimental Measurements, IGV at Full Axial Position ( $-5.0 \pm 0.5$ deg) .....	66
19. Comparison of Model Computed Stage Pressure Ratios Near Compressor Stability Limit with Experimental Measurements, IGV at Full Axial Position ( $-5.0 \pm 0.5$ deg) .....	69

<u>Figure</u>	<u>Page</u>
20. Comparison of Model Computed Stage Temperature Ratios Near Compressor Stability Limit with Experimental Measurements, IGV at Full Axial Position ( $-5.0 \pm 0.5$ deg) .....	72
21. Division of Compressor into Control Volumes .....	75
22. Control Volume Velocities and Fluxes .....	76
23. Schematic of Three-Dimensional, Time-Dependent Solution Procedure for TF41-A-1 HP Compressor Model .....	77
24. Illustration of Effect of Incremental Averaging on Numerical Instability .....	78
25. TF41-A-1 HP Compressor Model Loaded to Stall, $NH/\sqrt{\theta} = 92.6$ percent, IGV = 12 deg, No Distortion .....	79
26. TF41-A-1 HP Compressor Model Flow Breakdown in Terms of Computed Stage Inlet Total Pressures Leading to Instability, $NH/\sqrt{\theta} = 92.6$ percent, IGV = 12 deg, No Distortion .....	80
27. Computed Radial Distortion Influences on Stability, TF41-A-1 HP Compressor .....	81
28. Comparison of TF41-A-1 HP Compressor Model Radial Distortion Computations with Experimental Results .....	83
29. Model Computed Influence of Circumferential Pressure Distortion on Stability, TF41-A-1 HP Compressor .....	84
30. Comparison of TF41-A-1 HP Compressor Model Circumferential Distortion Computations with Experimental Results .....	85
31. Model Computed Influence of Circumferential Temperature Distortion on Stability, TF41-A-1 HP Compressor .....	86
32. Comparison of Circumferential Temperature Distortion Model Computations with Experimental Results .....	87
33. Effect of 5,000°R/sec Uniform Inlet Temperature Ramp on Compressor Stability as Computed by TF41-A-1 HP Compressor Model .....	88
34. TF41-A-1 HP Compressor Model Flow Breakdown with 5,000°R/sec Inlet Temperature Ramp, Nominal IGV Schedule, No Distortion .....	89
35. TF41-A-1 HP Compressor Model Computed Influence of Uniform Inlet Temperature Ramp Rates on Compressor Stability .....	90



<u>Figure</u>	<u>Page</u>
36. Effect of 5,000°R/sec Uniform Inlet Temperature Ramp on Compressor Inlet Corrected Airflow as Computed by TF41-A-1 HP Compressor Model .....	91
37. Effect of 5,000°R/sec Inlet Temperature Ramp (Imposed on 90-deg-Arc Circumferential Section) on Compressor Stability as Computed by TF41-A-1 HP Compressor Model .....	92
NOMENCLATURE .....	93

## 1.0 INTRODUCTION

Stable, aerodynamic operation of the compression system of a gas turbine engine is essential for the engine to perform satisfactorily. "Aerodynamically stable operation" refers to the condition existing when the compressor delivers a desired quantity of airflow on a continuous basis, compressed to a desired pressure, free of excessively large amplitude fluctuations in the flow properties throughout the compressor. The aerodynamic stability limit (surge line)—most commonly defined as a locus of points denoting maximum pressure ratio for stable operation as a function of corrected airflow rate—is typically determined from experimental results. However, only limited amounts of experimental compressor steady-state, transient, and stability limit data can be obtained during test programs because of test hardware and economic constraints. A validated mathematical model based on the limited experimental data is needed to make performance and stability computations at operating conditions with inlet distortion patterns and with subcomponent hardware configurations different from those actually tested. The use of such a model would significantly enhance the usefulness of data from any given compressor test.

The objectives of the work described herein were to construct a validated mathematical model of the high-pressure compressor of the TF41-A-1 turbofan engine and to provide thereby a new analysis tool for assessing the influence of external disturbances and compressor modifications on performance and stability. The objectives were accomplished through development of a one-dimensional, steady-state mathematical model for stability assessment with undisturbed flow and a three-dimensional, time-dependent mathematical model for analysis of distorted inflows and transient and dynamic disturbances.

For both models, example problems are presented and compared to experimental results. The problems using the one-dimensional, steady-state model consisted of determination of the steady-state stability limits (surge lines) with undisturbed flow for three distinct inlet guide vane schedules. Those problems using the three-dimensional, time-dependent model included determination of the stability limit (surge line) reduction caused by pure radial inlet pressure distortion, pure circumferential inlet pressure, and pure circumferential inlet temperature distortion. The effects of rapid upward ramps of inlet temperature on compressor stability were also investigated. The models compute compressor stability limits with reasonable accuracy.

An altitude evaluation of the TF41-A-1 turbofan engine with a highly instrumented, modified (Block 76) high-pressure compressor was conducted at the Arnold Engineering Development Center during the period September 15, 1977 through January 26, 1979. Pressure and temperature measurements obtained during this evaluation provided

experimental data for formulation of the compressor stage characteristics and validation of the models.

The technology required to construct compressor models applicable to predicting compressor stability margin loss caused by external disturbance in flow conditions was developed in Ref. 1. This demonstrated the validity of the multidimensional form of a mathematical model for a four-stage, fixed-geometry compressor at one value of corrected rotor speed. In this program, refinements were introduced to the basic (Ref. 1) model. These refinements were introduced to improve the generality of the model, to accommodate the variable rotor speed and the variable-geometry features of the TF41-A-1 high-pressure compressor, to increase accuracy, and to accommodate the inherently unstable numerical solutions caused by error buildup in the model calculations. This report describes the manner in which the models were constructed and the results obtained.

## **2.0 TF41-A-1 TURBOFAN ENGINE ALTITUDE AEROMECHANICAL TEST AND RESULTS**

Because the information derived from the TF41-A-1 turbofan engine altitude test is such an integral part of the effort reported herein, a description of the engine and instrumentation and pertinent results is presented.

### **2.1 ENGINE DESCRIPTION**

The TF41-A-1, manufactured by the Detroit Diesel Allison (DDA) Division of the General Motors Corporation, is a two-spool, low-bypass-ratio, nonaugmented turbofan engine (Fig. 1) in the 14,500-lbf-thrust class. The engine incorporates a three-stage fan and a two-stage, intermediate compressor driven by a two-stage, low-pressure turbine and an eleven-stage, high-pressure compressor driven by a two-stage, high-pressure turbine. The engine incorporates a can-annular combustor, an engine-controlled, high-pressure compressor interstage (seventh-stage) bleed system, and an annular fan duct. A schematic of the engine installation in the T4 test cell is presented in Fig. 2.

The fan, intermediate compressor, and high-pressure compressor pressure ratios at sea-level-static, intermediate power are 2.48, 1.41, and 6.20, respectively, for an overall pressure ratio of 21.7 at a rated engine airflow of 260 lbm/sec, a high-pressure rotor speed,  $N_{H_2}$ , of 12,840 rpm, and a fan rotor speed,  $N_L$ , of 8,940 rpm. Airflow is split at the fan exit, and the bypass air passes through the annular fan duct and mixes again with the gas generator airflow aft of the low-pressure turbine exit at the tailpipe inlet. The gas generator air passes

through the intermediate compressor and into the high-pressure compressor through the variable-position inlet guide vanes. The high-pressure compressor incorporates a bleed manifold at the compressor exit in the outer compressor case for extraction of air for aircraft services. The fan has no inlet guide vanes, and the bulletnose rotates; there are no anti-icing provisions.

### **2.1.1 High-Pressure Compressor Modifications**

The engine (S/N 141683/3) utilized a production high-pressure compressor that had been modified to include: (1) full-chord, clapperless, first-stage rotor blades with increased thickness-to-chord ratio and revised taper, (2) "Eiffel Tower" stator vanes for stages 4, 5, and 6 having increased thickness near the root, looser dovetails, and glass bead peened surfaces, and (3) modified spacer between stages 9 and 10. The first two modifications are referred to as "Block 76" design modifications. A detailed schematic of the high-pressure compressor is presented in Fig. 3.

### **2.1.2 High-Pressure Compressor Variable-Geometry Control System**

The high-pressure compressor incorporates a hydromechanical control system to position the inlet guide vanes (IGV's) and the compressor bleed valve (BVP) by a common actuator through a system of linkages.

The inlet guide vanes are scheduled as functions of engine inlet air temperature and high-pressure rotor speed. The bleed valve is fully open when the guide vanes are at 35 deg and fully closed when the guide vanes reach 24 deg.

## **2.2 INSTRUMENTATION**

Instrumentation was provided to measure dynamic stresses and aerodynamic pressures and temperatures; rotor speeds; fuel system pressures, temperatures, and flow rates; lube oil and hydraulic system pressures and temperatures; and other engine and test cell system parameters required for proper operation of the engine.

The instrumentation providing data for this study was located in the high-pressure (HP) compressor. The HP compressor was heavily instrumented since one of the objectives of the altitude test program was to determine the detailed aerodynamic characteristics of the HP compressor throughout the TF41-A-1 engine operating envelope. In addition to the array of steady-state instrumentation, the HP compressor was also instrumented with high-response, wall-static pressure transducers. A diagram showing the type, number, and location of the HP compressor interstage instrumentation is presented in Fig. 4.

## 2.3 PROCEDURE FOR HIGH-PRESSURE COMPRESSOR STABILITY ASSESSMENT

Following setting of the desired simulated flight conditions the high-pressure rotor speed was adjusted to yield a selected inlet guide vane position, IGV, thereby establishing the baseline point. The HP compressor was then slowly back-pressured by opening the inbleed air system valve until surge occurred; steady-state and transient data were obtained along the constant IGV line from baseline to the surge point. The power lever was moved during compressor loading to maintain the selected HP IGV angle at a constant value. When the HP compressor surged, the inbleed air system valve was closed to relieve the compressor and to permit recovery.

The surge testing of interest to this report was conducted at 30,000 ft, Mach number 0.7 in the range of operation where the seventh-stage bleed valve was closed and, at sea-level-static, where open seventh-stage bleed valve performance was obtained. To evaluate the effects of severely off-schedule, HP compressor IGV geometry, three IGV schedules were selected, representing extremes beyond which the TF41-A-1 engine is not expected to operate. These IGV schedules are defined as:

1. "Nominal," M72-3 vane schedule (Ref. 2),
2. "Axial," open approximately 10 deg at a given NH, and
3. "Cambered," closed approximately 10 deg at a given NH.

These schedules are shown in Fig. 5. For each IGV schedule, a HP compressor map was obtained by inbleeding high-pressure air into the exit diffuser by the previously stated procedure.

## 2.4 EXPERIMENTAL RESULTS

The following are results obtained during the TF41-A-1 altitude test pertinent to this report. The normal operating and surge lines for the HP compressor at 30,000 ft, Mach number 0.7, with nominal, axial, and cambered IGV schedules are presented in Fig. 6. The compressor surge margin was 26 percent at 46.0 lbm/sec corrected airflow. Misscheduling the IGV approximately 10 deg axial and cambered had no measurable effect on the Block 76 compressor surge margin.

The normal operating and surge lines for the HP compressor at sea-level-static conditions with nominal, axial, and cambered IGV schedules at low rotor speeds at which the seventh-stage bleed valve is open are presented in Fig. 7. Compressor exit airflow corrected to compressor inlet conditions was used as the abscissa of this curve because no provision was made to calculate seventh-stage bleed flow rate, and high-pressure compressor inlet airflow is therefore undefined since compressor airflow was computed downstream by assuming choked flow in the HP turbine vanes. The compressor surge margin with the bleed valve 100 percent open was 41 percent at 24.5 lbm/sec corrected airflow with the nominal IGV schedule and at 27 lbm/sec with the cambered IGV schedule. Surge could not be induced with the bleed valve 100 percent open with the axial IGV schedule.

Interstage dynamic pressures during a typical surge sequence are presented in Fig. 8. That the surge originated near the sixth stage is indicated by the pressure traces reflecting the increase in dynamic pressure at stages 1, 2, and 4 and by the corresponding decrease in dynamic pressure at stages 8 and 10 following the initiation of surge.

The aerodynamic pressures and temperatures from the HP compressor vane interstage instrumentation (Fig. 4) are presented, respectively, in Figs. 9 and 10 as typical examples of the total-pressure and total-temperature profiles existing during uniform engine inlet-flow conditions.

Experimental data and results presented are compared to the mathematical model predictions in following sections.

### **3.0 DESCRIPTION OF ONE-DIMENSIONAL, STEADY-STATE MODEL**

A one-dimensional, steady-state model of the TF41-A-1 HP compressor was developed, based on compressor geometry provided by the engine manufacturer and on stage characteristics formulated from the experiment data. The steady-state model makes use of individual stage characteristics of pressure and temperature rise as functions of mass flow to predict the quasi-steady uniform flow performance of the compressor.

#### **3.1 MODEL CONCEPTS**

A steady-state compressor model is simply a mathematical representation of the compressor performance. Sufficient data are necessary to determine the total-pressure and total-temperature ratios for the compressor as functions of corrected airflow and rotor speed. Thus, modeling the overall steady-state performance of a compressor can be as

simple as reading a compressor map. However, for the model to predict stage performance as well as overall performance, it is necessary to analyze the components or stages of the compression system to account for stage interactions. The steps for development of the one-dimensional, steady-state model are (1) defining control volumes, (2) writing governing equations, and (3) giving the method of solution.

### 3.1.1 Control Volume Analysis

The TF41-A-1 HP compressor system (overall control volume) was divided into twenty elemental control volumes consisting of four inlet duct, eleven compressor, and five exit duct elemental control volumes (Fig. 11). The division of the inlet and exit ducting permitted calculation of the flow properties in the ducting by applying conservation of mass, momentum, and energy laws. The division of the compressor into elemental control volumes representing stage lengths in the axial direction was made because the pressure and temperature rise between stage entry and exit were obtained from experimentally determined stage characteristics as discussed in Section 3.2. For the one-dimensional, steady-state analysis, all flow properties are "bulked" in the radial and circumferential directions, and variations with the axial coordinate only are considered.

### 3.1.2 Governing Equations

An axial-flow compressor imparts kinetic energy to the flow of a fluid by a direct interaction between that fluid and the rotating machine elements. The fluid is then diffused through the diverging flow passages between the blades, reducing the kinetic energy and increasing the static pressure. The divergence of each passage is determined by the inlet and exit air angles. Since the blades are most often closely spaced, the exit-air angle is approximately equal to the trailing-edge angle of the blades. The inlet-air angle, however, is a function of the axial velocity entering the blades and their rotational speed. Thus, a stage flow coefficient ( $\phi$ ), as defined in Ref. 1,

$$\phi = \frac{U}{U_{wh}} \quad (1)$$

where  $U$  = axial velocity and  $U_{wh}$  = wheel speed, was used to represent the inlet-air angle at the entry of each compressor elemental control volume.

The flow coefficient,  $\phi$ , is related to the blade angle of attack,  $\alpha$ , by the stagger angle,  $\lambda$ , which is a constant for any given blade row through the relationship

$$\phi \approx \cot(\lambda + \alpha) \quad (2)$$

Thus,  $\phi$  serves the same purpose in the compressor stage as  $\alpha$  does for aircraft wing aerodynamics. It decreases with increasing  $\alpha$ ; therefore, small  $\phi$  means large  $\alpha$ , and vice versa.

The temperature rise across each compressor elemental control volume was represented by the stage temperature coefficient,  $\psi^T$ , expressed as

$$\psi^T = \frac{C_p (TR - 1)}{U_{wh}^2 / T_1} \quad (3)$$

where TR is the stage or compressor elemental control volume temperature ratio,  $C_p$  is specific heat at constant pressure, and T is the stagnation (total) temperature.

The temperature ratio of Eq. (3) for an ideal compressor stage is the isentropic temperature ratio defined from stage entry and exit stagnation pressure. Using this ratio, another stage parameter, the stage pressure coefficient,  $\psi^P$ , is defined,

$$\psi^P = \frac{C_p \left[ \frac{\gamma - 1}{PR^\gamma} - 1 \right]}{U_{wh}^2 / T_1} \quad (4)$$

where PR is the stage or compressor elemental control volume pressure ratio,

$$\gamma = \frac{C_p}{C_v} = \frac{C_p}{C_p - R/J} \quad (5)$$

and where  $\gamma$  is the ratio of specific heats,  $C_v$  is the specific heat at constant volume, and  $R/J$  is the gas constant/mechanical equivalent of heat. For this model, the specific heat at constant pressure,  $C_p$ , was computed as a function of temperature from the empirical equation:

$$C_p = 0.2318 + 0.104 \times 10^{-4}T + 0.7166 \times 10^{-8}T^2 \quad (6)$$

where the constants are based on the specific heats of the constituents of air.



The temperature and pressure coefficients ( $\psi^T$  and  $\psi^P$ ) are primarily functions of the flow coefficient,  $\phi$ , and the flow direction (Ref. 1). Thus, a set of curves

$$\left. \begin{aligned} \psi^T &= f(\phi) \\ \psi^P &= f(\phi) \end{aligned} \right\} \quad (7)$$

is referred to as "stage characteristics," and, with flow direction information, fully defines a stage's performance from a one-dimensional standpoint.

In principle, theoretical or experimental lift and drag coefficients could be used, along with stage geometry, to compute the stage characteristics. However, corrections for blade row interference losses and secondary flows would be required. The method used in this study was to compute directly  $\psi^T$ ,  $\psi^P$ , and  $\phi$  by Eqs. (1), (3), and (4) from the experimental measurements of stage total temperature, flow rate, and total pressure at the stage entry and exit. A discussion of the stage characteristics obtained is presented in Section 3.2.

Friction losses in the inlet and exit ducting, internal bleeds, and the forces acting on the fluid in the compressor must satisfy mass, momentum, and energy conservation principles as they relate to any elemental control volume (Fig. 12).

### 3.1.2.1 Mass

Application of the mass conservation principle to the elemental control volume yields

$$\underbrace{W + \frac{\partial W}{\partial z} dz + WB}_{\text{mass leaving control volume}} = \underbrace{W}_{\text{mass entering control volume}} \quad (8)$$

where  $W$  is the mass flow rate and  $z$  is the axial component.

Equation (8) reduces to

$$W_{\text{exit}} = W_{\text{entrance}} - WB \quad (9)$$

where bleed flow,  $WB$ , is assumed to cross the control volume boundary normal to the axial direction.

### 3.1.2.2 Momentum

The summation of all forces in a given direction is equal to the change of momentum in that direction, and gives

$$\begin{aligned}
 & \underbrace{F \, dz + PS \, A - \left[ PS \, A + \frac{\partial (PS \, A)}{\partial z} \, dz \right] + PS \left[ \left( A + \frac{\partial A}{\partial z} \, dz \right) - A \right]}_{\text{axial forces acting on control volume}} \\
 &= \underbrace{\left[ WU + \frac{\partial (WU)}{\partial z} \, dz \right]}_{\text{momentum leaving control volume}} - \underbrace{WU}_{\text{momentum entering control volume}}
 \end{aligned} \tag{10}$$

where  $F$  is the force of compressor blading and cases acting on fluid, including wall pressure area force;  $PS$  is the static pressure; and  $A$  is the area.

Equation (10) may be reduced to give

$$\frac{\partial (IMP)}{\partial z} = F + PS \frac{\partial A}{\partial z} \tag{11}$$

where the impulse function,  $IMP$ , is defined as

$$IMP = WU + PS \, A \tag{12}$$

The resultant axial force,  $F$ , is defined as

$$F = \underbrace{IMP}_{\text{impulse leaving control volume}} - \underbrace{IMP}_{\text{impulse entering control volume}} \tag{13}$$

and in the case of ducting control volumes, assuming adiabatic flow conditions, reduces to a simple friction loss expressed as

$$F = -C_d \, \gamma \, PS \, A \, M^2 \tag{14}$$

where  $C_d$  is the duct pressure loss coefficient and  $M$  is the Mach number. The value of  $C_d$  was adjusted to give a reasonable stagnation pressure loss in the ducting.

### 3.1.2.3 Energy

Energy conservation gives

$$\underbrace{H + \frac{\partial H}{\partial z} dz}_{\text{enthalpy leaving control volume}} = \underbrace{H}_{\text{enthalpy entering control volume}} + \underbrace{WS dz}_{\text{shaft work done on fluid in control volume}} - \underbrace{Q dz}_{\text{heat added to fluid in control volume}} \quad (15)$$

where  $H$  is the total enthalpy flux,  $WS$  is the stage shaft work added to fluid in control volume, and  $Q$  is the rate of heat addition to control volume. Equation (15) may be reduced to

$$\frac{\partial H}{\partial z} = WS + Q \quad (16)$$

where

$$H = W C_p T \quad (17)$$

The shaft work,  $WS$ , is defined as

$$WS = W C_p T (TR - 1) \quad (18)$$

and is zero in the ducting control volumes.

### 3.1.2.4 State and Additional Equations

Additional equations required include the perfect-gas equation of state,

$$p = \rho R T, \quad (19)$$

where  $p$  is the density and  $R$  is the gas constant; stagnation (total) state temperature equation,

$$T = TS + \frac{U^2}{2C_p} \quad (20)$$

and stagnation (total) state pressure equation,

$$P = PS \left[ \frac{T}{TS} \right]^{\frac{\gamma}{\gamma-1}} \quad (21)$$

Also required is the Mach number,

$$M = \frac{U}{a} \quad (22)$$

where the acoustic velocity,  $a$ , is

$$a = \sqrt{\gamma R TS} = \sqrt{\gamma \frac{PS}{\rho}} \quad (23)$$

### 3.1.3 Method of Solution

The one-dimensional, steady-state model uses a "stacking" procedure to determine flow properties throughout the compressor and associated ducting. The one-dimensional model of the TF41-A-1 HP compression system uses segmented inlet and exit ducting as indicated in Fig. 11. The solution is begun with known air properties at the compressor inlet (total pressure, total temperature, and airflow), ducting geometry, and a coefficient of friction. Flow properties throughout the inlet ducting are calculated using the one-dimensional, steady-state conservation laws (see Section 3.1.2). Since the exit of one duct segment is the entrance to the next segment, the solution is marched upstream from the compressor inlet to the duct inlet by an iterative procedure. For the compressor segments, with compressor inlet flow properties known, a stage-by-stage calculation downstream through the compressor using the stage characteristics formulated from experimental data gives individual stage pressure and temperature ratios so that overall compressor performance can be calculated. Compressor aft-ducting flow properties are then calculated using the one-dimensional, steady-state conservation laws.

## 3.2 TF41-A-1 HIGH-PRESSURE COMPRESSOR STEADY-STATE STAGE CHARACTERISTICS

Representative stage characteristics (temperature and pressure coefficients as functions of flow coefficient) are presented schematically in Fig. 13 for a fixed-geometry compressor operating at a single value of compressor corrected rotor speed.

Several problems had to be resolved because of the variable geometry of the TF41-A-1 HP compressor:

1. To allow investigation of off-nominal schedules, the model had to account for variable IGV effects without relating IGV position to rotor speed.
2. To determine the stage flow rates during bleed-valve open operation the seventh-stage bleed flow rate had to be estimated.
3. Interpolation of stage characteristics between lines of the chosen dependent variables had to reflect the experimentally determined results.

Assumptions were made, and procedures were established and incorporated into the TF41-A-1 HP compressor models to meet these requirements. The steady-state stage characteristics are utilized both in the one-dimensional, steady-state model and in the three-dimensional, time-dependent model; therefore, the following discussion will apply to both models.

The variation of the steady-state stage characteristics with rotor speed was assumed to be second order, with primary effect attributed to the IGV position. This relates the stage characteristics to the single dependent variable, the IGV, and greatly simplifies their formulation.

An empirical relationship between bleed valve position, BVP, and bleed flow rate, WB, was developed, based on the reactions of various static-to-total-pressure ratios determined from the interstage instrumentation (Fig. 4). This estimation of the seventh-stage bleed flow rate permitted calculation of the stage characteristics from experimental data during open bleed-valve operation (see Section 2.1.2).

The stage characteristic parameters  $\psi^T$ ,  $\psi^P$ , and  $\phi$  were computed from measurements of rotor speed, flow rate, total pressure, and total temperature for each stage entry by use of Eqs. (3), (4), and (1) respectively for all data obtained during the TF41-A-1 test. The stage characteristics were then generalized along lines of constant IGV angle over the full range of IGV operation (from -5.5 to 36 deg). The TF41-A-1 HP compressor stage characteristics developed from this analysis are presented in Fig. 14.

The stage characteristics were incorporated by means of a series of second-order curve fits. Frequently, a prediction of compressor performance is required at some value of IGV that is not equal to any of the values used to formulate the stage characteristics. Hence,

interpolation of the required parameter ( $\psi^T$  or  $\psi^P$ ) from the values of stage characteristics between higher and lower guide vane positions is required. The interpolation procedure used in the models is based on a fixed value of  $\phi$ . This procedure was adopted because the variation of compressor mass flow with rotor speed is effectively represented by  $\phi$ . Hence, the same  $\phi$  can be used to determine  $\psi^T$  or  $\psi^P$  at the higher and lower guide vane positions. The  $\psi^T$  or  $\psi^P$  can then be interpolated linearly to define the value at the desired IGV for a given value of  $\phi$ .

### 3.3 MODEL VERIFICATION

Figure 15 presents steady-state model computations of compressor performance at 30,000 ft and Mach number 0.7, with nominal, cambered, and axial inlet guide vane schedules over the corrected rotor-speed range from 90 to 100 percent and compares them to experimental results. The steady-state model computes compressor surge pressure ratios within 2.4 percent of the experimental stability limits for the nominal, cambered, and axial guide vane schedules. For these results (Fig. 15) the model computations represent constant corrected rotor-speed lines at a constant IGV, whereas the experimental data were obtained with nearly constant IGV (+0.4 deg) while corrected HP rotor speed,  $NH/\sqrt{\theta_{24}}$ , varied as much as 3.6 percent. The procedure used to obtain the experimental data (see Section 2.3), by maintaining constant IGV during the HP compressor loading, resulted in near constant  $NH$  ( $\pm 1.0$  percent). However, the increase in energy to the engine turbines resulted in increased fan rotor speed,  $NL$ . Thus, the inlet temperature,  $T_{24}$ , delivered to the HP compressor increased from the baseline point to the stall point with corresponding decreases in  $NH/\sqrt{\theta_{24}}$ . Therefore, the model and experimental data represent different paths from baseline to stall point. This is illustrated in Fig. 16 in which the steady-state model predictions are presented at the corresponding corrected rotor-speeds of the experimental data points for the -0.3-deg IGV line on the axial IGV schedule (Fig. 15c).

Steady-state model computations of overall compressor performance with seventh-stage bleed valve open at sea-level-static conditions with nominal, cambered, and axial inlet guide vane schedules, over the corrected rotor-speed range from 85 to 92 percent are presented and compared to experimental results in Fig. 17. The steady-state model computes compressor surge pressure ratios within 4.0 percent of the experimental stability limits for the nominal, cambered, and axial guide vane schedules with seventh-stage bleed valve open.

The large quantity of steady-state temperature and pressure measurements made on the TF41-A-1 HP compressor during testing allows detailed model-to-experiment comparisons on a stage-by-stage basis. Figures 18, 19, and 20 show model computed and experimentally determined stage flow coefficients, pressure ratios, and temperature ratios,

respectively, as functions of corrected rotor speed near the compressor stability limit. Good agreement was obtained (within 0.5 percent).

It is evident from Fig. 18 that the TF41-A-1 HP compressor operates with forward stages (1 through 3) below the stall value of stage flow coefficient at corrected rotor speeds below approximately 91 percent. This operation reinforces previous theories and experiment observations (Refs. 1, 3, 4, and 5). At low corrected rotor speeds, the forward stages cannot deliver their intended pressure ratio. The flow density provided to the aft stages is therefore lower than that for which the compressor axial area distribution was designed. Thus, to maintain steady mass flow continuity, the flow coefficients (axial velocity) in the aft stages must increase with decreasing corrected rotor speed. Indeed, at sufficiently low corrected rotor speeds, the aft stages are even choked. At low corrected rotor speeds, as the load on the compressor (the demanded pressure ratio) is increased by back-pressuring, the compressor flow reduces, and the following occur: Initially the aft stages may increase their pressure ratio in response to the flow reduction at a greater rate than the rate of decrease in pressure ratio occurring in the forward stages; thus, the increased load may be satisfied. However, as the loading continues, the forward stages become more and more stalled, and a point is eventually reached at which the aft stages can no longer compensate. At that point, overall compressor instability occurs.

It is necessary to distinguish stage stalling from overall compressor stalling or instability. Instability is always preceded by stage stall but is not always simultaneous with stage stall.

#### **4.0 DESCRIPTION OF THREE-DIMENSIONAL, TIME-DEPENDENT MODEL**

The three-dimensional, time-dependent model detailed in Ref. 1 was converted to the TF41-A-1 high-pressure compressor system by the incorporation of TF41-A-1 compressor geometry and stage characteristics formulated during the steady-state model investigation discussed in Section 3. The time-dependent model utilizes a finite control volume, integral approach to solve the full nonlinear form of the three-dimensional conservation laws of mass, momentum, and energy by means of a finite difference technique. Thus, the model is capable of computing the influences of transient and dynamic disturbances with either uniform or distorted inflow.

#### **4.1 MODEL CONCEPTS**

A detailed description of the concepts involved in the three-dimensional, time-dependent model development is presented in Ref. 1 and summarized in this section.

The compressor was divided radially, circumferentially, and axially on a stage-by-stage basis into control volumes (Figs. 21 and 22). The governing equations were developed from the three-dimensional, time-dependent mass, momentum, and energy equations for a finite control volume. The force and shaft work applied to the fluid are determined from empirical steady-state stage characteristics modified for unsteady cascade airfoil effects. For simplification empirical crossflow relationships were used to replace the radial and circumferential momentum equations. The radial work distribution variation effect necessary for treatment of radial distortion was approximated using average stage characteristics modified as a function of radius by empirical total pressure and total temperature profile correction. Crossflow and unsteady cascade effects for circumferential distortion were also built into the model.

#### 4.1.1 Method of Solution

The three-dimensional, time-dependent compressor model is formulated as an initial condition problem. The values of the dependent variables (mass, momentum, and energy) are specified for every control volume location (axial, radial, and circumferential coordinate) to start the solution. For simplicity, the solution is always started from a steady, uniform flow condition, thus allowing determination of the initial conditions by use of the one-dimensional, steady-state model. With dependent variables,  $\rho$ ,  $\rho U$ , and  $X$  (representing mass, momentum, and energy) specified for every control volume location,  $ijk$ , for time equal zero, the time derivatives are computed from the following equations:

##### 4.1.1.1 Mass

$$\frac{\partial \rho_{ipjk}}{\partial t} = \frac{1}{vol_{ijk}} \left[ WZ_{ijk} + WR_{ijk} + WC_{ijk} - WB_{ijk} - WZ_{ipjk} - WR_{ijpk} - WC_{ijkp} \right] \quad (24)$$

##### 4.1.1.2 Axial Momentum

$$\frac{\partial (\rho U)_{ijk}}{\partial t} = \frac{1}{VOL_{ijk}} \left[ F_{ijk} + IMP_{ijk} - IMP_{ipjk} \right] \quad (25)$$

The force,  $F$ , is obtained from stage characteristic information modified for unsteady cascade airfoil effects. The impulse terms are

$$IMP = PS AZ + WZ U \quad (26)$$

where  $AZ$  is the control volume area normal to axial direction and  $WZ$  is the mass flux across radially-facing control volume boundary.



#### 4.1.1.3 Energy

$$\frac{\partial X_{ipjk}}{\partial t} = \frac{1}{Vol_{ijk}} \left[ WS_{ijk} + Q_{ijk} + HZ_{ijk} - HZ_{ipjk} \right] \quad (27)$$

where WS is the stage shaft work added to fluid in control volume, Q is the rate of heat addition to control volume, HZ is the total enthalpy flux transported across control volume axial-facing boundary, and where

$$\chi = \rho \left[ e + \frac{U^2}{2} \right] \quad (28)$$

The radial and circumferential impulse and velocity terms neglected in Eqs. (25) and (28) are second-order terms determined respectively by nondimensionalization and order-of-magnitude analysis of the equations; therefore, their influence on the solution would have been small. Also, including these terms caused the numerical solutions to be generally less stable and to oscillate with small amplitude when a steady-state condition was reached. Once these calculations of the time derivatives of the dependent variables,  $\rho$ ,  $\rho U$ , and  $X$ , are carried out for all the volumes, the solution can be advanced in time through use of a fourth-order Runge-Kutta numerical integration method (Ref. 6) that provides values of the variables at the next time step. The sequence is then repeated, with boundary conditions changing in accordance with the specified event simulation for as many time steps as are required. A schematic of the computational process is presented in Fig. 23.

The system of equations constituting the model is for time-dependent, three-dimensional subsonic flow and is hyperbolic in nature, with specified boundary conditions and initial conditions. Thus, each integration step to compute the dependent variables at the new time ( $t + \Delta t$ ) must be made within the region of influence of the known values at time,  $t$ : The Courant-Friedrichs-Lewy maximum time step criterion (Ref. 7)

$$\Delta t_{max} = \frac{\Delta Z_{min}}{a + U_{max}} \quad (30)$$

must be observed. For  $\Delta Z_{min} = 0.111$  ft,  $a = 1,625$  ft/sec (values at TS = 1,100°R),  $U_{max} = a$ ,

$$\Delta t_{max} = 3.4 \times 10^{-5} \text{ sec}$$

A time step of  $1.0 \times 10^{-5}$  sec was used for the TF41-A-1 HP compressor model.

## **4.2 THREE-DIMENSIONAL, TIME-DEPENDENT MODEL REFINEMENTS**

Before this study, the three-dimensional, time-dependent model concepts (Ref. 1) summarized in the previous section had only been applied to a four-stage, fixed-geometry compressor operating at a single rotor speed. During this investigation, a number of refinements were introduced to the basic model to accommodate variable rotor speed and variable-geometry features of the TF41-A-1 HP compressor. In addition, refinements were incorporated to improve accuracy, and to handle numerical solutions that were inherently unstable. (This instability was caused by error buildup in the model calculations.) These refinements are discussed in the following paragraphs.

### **4.2.1 Variable Rotor Speed and Variable Geometry**

The variable-rotor-speed and variable geometry requirements were met by incorporating the IGV-dependent, steady-state stage characteristics formulated during the one-dimensional, steady-state model investigation (Section 3.2). With both NH and IGV specified as inputs (boundary conditions), stage shaft work and forces could be determined for all IGV schedules.

### **4.2.2 Real-Gas Properties**

As was done in the one-dimensional, steady-state model development, real-gas properties were approximated by incorporation of an empirical relationship for the specific heat at constant pressure,  $C_p$ , as a function of temperature and gas composition.

### **4.2.3 Modified Fourth-Order Runge-Kutta Numerical Integration Method**

Conversion of the three-dimensional, time-dependent model to the TF41-A-1 HP compressor form with incorporation of the previously discussed refinements resulted in a mathematical model that was numerically unstable at all conditions. All attempts to start the model resulted in unsteady conditions that produced a model computation abort similar in nature to a compressor surge. An analysis of the instability revealed that the fourth-order Runge-Kutta numerical integration method was not convergent when applied to the hyperbolic equations constituting the TF41-A-1 HP compressor model. Further analysis revealed that the divergence was of a series form, alternating around the desired solution. Therefore, an average of the oscillations over at least one cycle approximates the desired solution.

A technique was developed and incorporated to average the oscillations of the dependent variables (mass, momentum, and energy) over a predetermined time interval and restarting the solution at the average value of the dependent variables. The averaging technique was investigated for convergence by running various time intervals to determine the minimum interval at which convergence could be maintained. The minimum time interval for satisfactory convergence was determined to be approximately  $0.2 \times 10^{-3}$  sec. This time interval was also effective at the time of actual compressor surge since the instabilities that occur during the surge event fully develop and produce model computation abort within  $0.2 \times 10^{-3}$  sec. An illustration of the effect of the incremental averaging technique on numerical instability is presented in Fig. 24.

### 4.3 MODEL VERIFICATION

The TF41-A-1 HP compressor model was loaded to the stability limit by increasing the exit static pressure until flow breakdown was indicated. Inlet stagnation pressure and temperature were constant. Corrected rotor speed was 92.6 percent of design, and IGV angle was 12 deg (nominal IGV schedule). Figure 25 illustrates the loading and the resulting stall process. Exit static pressure was ramped at a rapid rate to minimize the computer time necessary for the computations. The rate was slow enough, however, that transient effects were very small. Airflow at any stage never differed from compressor inlet airflow by more than 0.6 percent during loading. As the load on the compressor increased, compressor pressure ratio increased, and airflow decreased until flow breakdown was indicated.

Figure 26 presents the model computed stage inlet total pressures on an expanded time scale covering the flow breakdown. Initiation of surge is indicated at  $t = 76.78$  msec by observation of the sixth- and seventh-stage inlet total pressures. The inlet total pressure at stage seven decreases because stage six stalls, thereby limiting pumping capacity. The inlet total pressure of stage six increases in response to the sudden blockage to the flow produced by the stalling in stage six. The indication that compressor surge originated in the sixth stage agrees with the experimental results reported in Section 2.4

The model solution thus indicated the following sequence leading to compressor instability: The compressor is loaded and mass flow decreases until a stage somewhere in the compressor reaches its stall point (its maximum pressure coefficient point). The ability of that stage to continue to pump flow (i.e., to help support the pressure gradient over the length of the compressor imposed by the back pressure load) begins to diminish. As the flow reduction continues, the ability of the stage to pump diminishes even further because of the increased load. Eventually, a point is reached where the flow into the stage becomes fully

stalled; thus, little force on the fluid is provided to pump the flow, and the flow path through the compressor becomes blocked because of the highly separated condition of the stalled flow in the channels.

In terms of the solution of the model equations, as the loading is increased, a point is reached where no stable solution to the governing equations exists that will satisfy the imposed load (boundary conditions); thus, the solution, like the flow through the compressor, becomes unstable. However, the behavior of the model quickly becomes nonrepresentative of the compressor shortly after flow breakdown because the stage characteristics are not valid for deeply stalled, dynamic situations.

### 4.3.1 Pure Radial and Circumferential Distortion Patterns

Three types of distortion patterns were computed to see the influence of pattern severity and shape variations on the TF41-A-1 HP compressor. The patterns considered were pure radial pressure distortion, pure circumferential pressure distortion, and pure circumferential temperature distortion. No specific experimental data for the TF41-A-1 HP compressor were available for these cases. Therefore, only comparisons to experimental results from other compressors could be made.

#### 4.3.1.1 Radial Pressure Distortion

Figure 27a illustrates the results of loading (by increasing exit static pressure) the TF41-A-1 HP compressor model to the stability limit with tip radial distortion (low pressure in the tip region). Pattern severities ( $P_{\max} - P_{\min}/P_{\text{avg}}$ ), of 5, 10, and 20 percent were considered. Figure 27b shows the results for the hub radial case and indicates that the TF41-A-1 HP compressor would be more sensitive to tip radial distortion than to hub radial distortion. Figure 28 compares of the TF41-A-1 HP compressor model results with experimental data from a J85-13 engine test (Ref. 8). Similar results were obtained, except that the J85-13 engine was even less tolerant of tip radial distortion than the TF41-A-1 HP compressor was computed to be.

#### 4.3.1.2 Circumferential Pressure Distortion

The effect of increasing the severity of a 180-deg-arc circumferential pressure distortion pattern is presented in Fig. 29. Compressor surge limit in terms of pressure ratio decreased 3.1, 4.8, and 7.9 percent, respectively, from the uniform flow (no distortion) surge limit at pattern severities of 5, 10, and 20 percent. Figure 30 shows the TF41-A-1 HP compressor

model results compared to a range of experimental data from other compressors (Refs. 8 and 9). The trend and magnitude predicted by the model agree well with the experimental data.

#### 4.3.1.3 Circumferential Temperature Distortion

Figure 31 shows the effect of varying the severity of 180-deg-arc total temperature distortion on compressor stability. Temperature distortion destabilizes the compressor in much the same manner as does pressure distortion. The higher temperature region operates at reduced airflow, thus, at reduced flow coefficients compared to the low temperature region of the compressor. As the load on the compressor is increased, the high temperature region stalls first, eventually causing the entire compressor to become unstable.

For the example presented in Fig. 31, corrected rotor speed was held constant during the loading (exit static pressure increase) by maintaining constant average temperature over the face of the compressor.

Figure 32 shows a comparison of the TF41-A-1 HP compressor model computed stability limit pressure ratio reduction caused by circumferential temperature distortion to test results with other compressors (Refs. 8 and 10). The trend and magnitude predicted by the model agree well with the experimental data.

#### 4.3.2 Rapid Inlet Temperature Ramp to Stall

The TF41-A-1 HP compressor model was subjected to a series of uniform inlet temperature ramp rates of 2,000, 5,000 and 10,000°R/sec to simulate ingestion of hot gases from gun or rocket fire. The effects of inlet temperature ramps were investigated for three IGV schedules of the TF41-A-1 HP compressor. Guide vane schedules investigated were nominal, cambered (+ 10 deg from nominal), and axial (-10 deg from nominal). Mechanical rotor speed and inlet total pressure were held constant while exit static pressure was maintained at the level corresponding to experimentally determined operating line condition for the respective guide vane angle investigated. The initial corrected rotor speed was 92.6 percent. Figure 33 shows the effect of 5,000°R/sec uniform inlet temperature ramps with the nominal, cambered (+ 10 deg from nominal), and axial (-10 deg from nominal). mechanical no significant changes in transient surge limit with IGV schedule; this is expected since both steady-state model and experimental results indicated that misscheduling the inlet guide vane had no measurable effect on the TF41-A-1 compressor steady-state surge margin.

Analysis of the model computations (Fig. 34) indicate that the forward stages are rapidly driven into stall by the reduction in airflow accompanying the rapid temperature rise at the compressor inlet. Initiation of surge and associated flow breakdown occurred in the second stage and propagated back through the compressor.

Figure 35 shows the TF41-A-1 HP compressor model computed influence of uniform inlet temperature ramp rates on compressor stability with nominal, cambered and axial IGV schedules. The model results from Fig. 36 indicate that the nominal schedule produces slightly less reduction in airflow for a given temperature rise at the inlet than the cambered or axial schedules. This allowed stable compressor model operation with the nominal schedule at approximately 15°R higher inlet temperatures than could be obtained with the cambered or axial schedules for a given ramp rate.

Figure 37 shows the model predicted effect on compressor stability if the 5,000°R/sec inlet temperature ramp is imposed only on a 90-deg-arc circumferential section of the compressor inlet. This case illustrates a combined effect of the temperature ramp and the associated inlet temperature distortion. Model results presented in Fig. 37 indicate that compressor surge occurs 15.2 percent below the steady-state stability limit at an inlet temperature distortion level of 18.4 percent.

## 5.0 SUMMARY OF RESULTS

Validated TF41-A-1 HP compressor mathematical models capable of aerodynamic stall prediction were developed. The following summarize the specific efforts and analyses:

1. A one-dimensional, steady-state model of the TF41-A-1 high-pressure compressor was developed based on compressor geometry and stage characteristics formulated from experimental data for use in analyzing steady-state compressor phenomena and compressor improvement.
2. The one-dimensional, steady-state model computes compressor surge pressure ratios within 2.4 percent of that observed experimentally for nominal, cambered, and axial IGV schedules over the corrected rotor-speed range of from 90 to 100 percent.
3. The one-dimensional, steady-state model computes compressor surge pressure ratios within 4.0 percent of the experimental stability limits for nominal, cambered, and axial IGV schedules with seventh-stage bleed-valve-open operation.

4. A three-dimensional, time-dependent TF41-A-1 HP compressor model was developed for use in analyzing transient and dynamic disturbances with uniform or distorted inflow.
5. The TF41-A-1 three-dimensional, time-dependent model was subjected to pure radial pressure distortion, pure circumferential pressure distortion, and pure circumferential temperature distortion patterns of varying severity. Their influences on stability were computed. No specific experimental data for the TF41-A-1 HP compressor subjected to these specific distortion patterns were available. Therefore, comparisons were made to experimental results from other compressors. Trends and general magnitudes computed by the model agreed with the experimental results.
6. The TF41-A-1 three-dimensional, time-dependent model was driven to instability by ramping inlet temperature at rates of 2,000, 5,000, and 10,000°R/sec to simulate ingestion of hot gases from gun or rocket fire. Ramp heights varied from 74 to 108°R with the 2,000 and 10,000°R/sec inlet temperature ramp rates, respectively, at the cambered IGV schedule.
7. The aerodynamic instabilities that were encountered during model loading simulations occurred in test surges and exhibited characteristics representing the actual physical instability.

## REFERENCES

1. Kimzey, William F. "An Analysis of the Influence of Some External Disturbances on the Aerodynamic Stability of Turbine Engine Axial Flow Fans and Compressors." AEDC-TR-77-80 (AD-A043543), August 1977.
2. "Maintenance Instructions, Intermediate, Technical Manual 2J-TF41-6." Detroit Diesel Allison, October 1977.
3. Cohen, Henry, Rogers, G. F. C., and Saravanamuttoo, H.I. H. *Gas Turbine Theory*. Longman, London, 1972.
4. Pearson, H. and Bowmer, T. "Surging of Axial Compressors." *The Aeronautical Quarterly*, Vol. 1, No. 11, November 1949.

5. Goethert, B. H., Kimzey, William F., Huebschmann, Eugene C., Braun, Gerhard W., and Snyder, William T. "Research and Engineering Studies and Analyses of a Fan Engine Stall, Dynamic Interaction with Other Subsystems and System Performance." AFAPL-TR-70-51 (AD-872872), July 1970.
6. Cannahan, Brice, Luther, H. A., and Wilkes, James O. *Applied Numerical Methods*. John Wiley and Sons, New York, 1969.
7. Roache, Patrick J. *Computational Fluid Dynamics*. Hermosa Publishers, Albuquerque, New Mexico, 1972.
8. *Distortion Induced Engine Instability*. Neuilly Surseine (France), Advisory Group for Aerospace Research and Development, 1974.
9. Calogeras, James E., Mehalic, Charles M., and Burstadt, Paul L. "Experimental Investigation of the Effect of Screen-Induced Total-Pressure Distortion on Turbojet Stall Margin." NASA-TMX-2239, March 1971.
10. Mehalic, Charles M. and Lottig, Roy A. "Steady-State Inlet Temperature Distortion Effects on the Stall Limits of a J85-GE-13 Turbojet Engine." NASA-TMX-2290, February 1974.



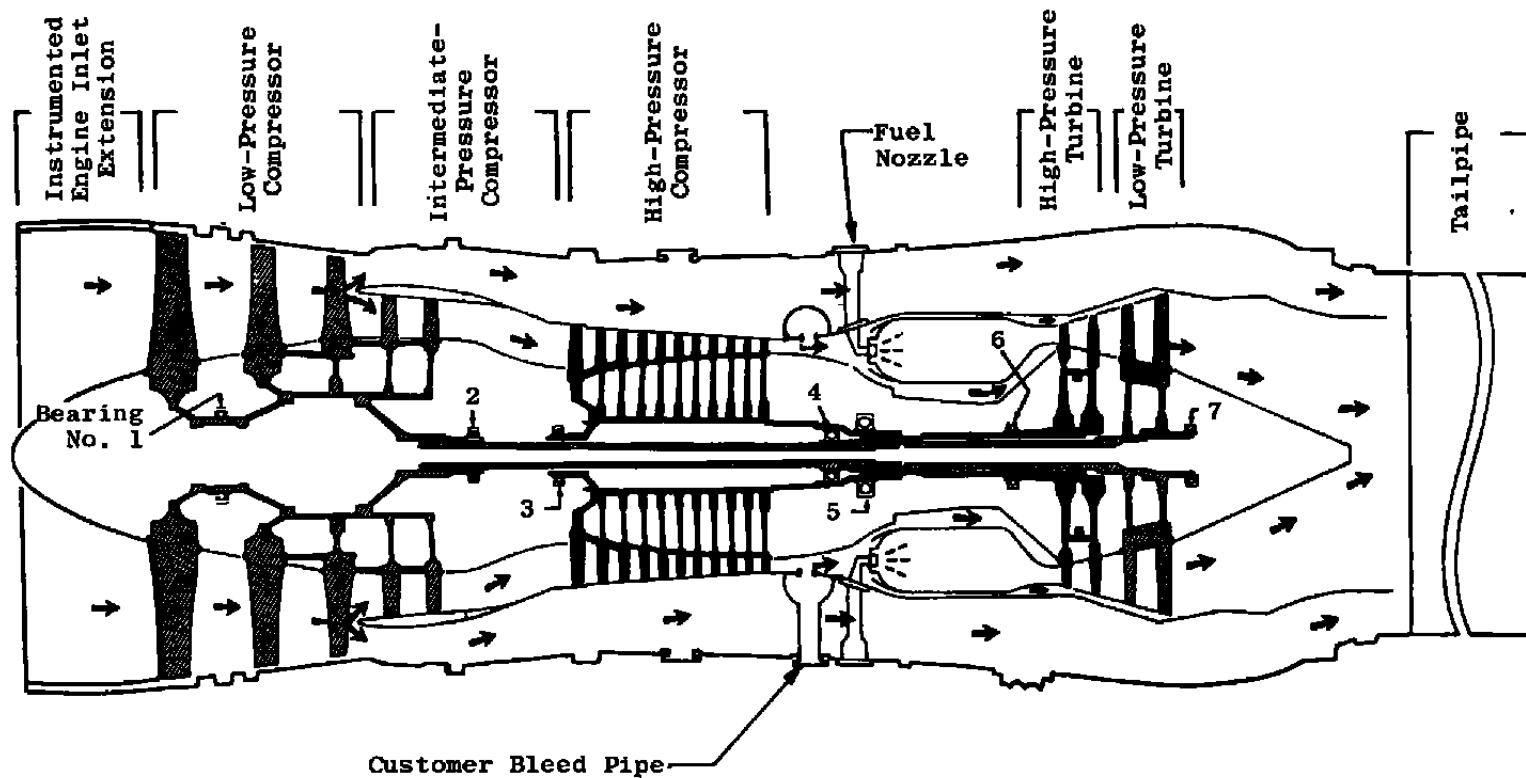


Figure 1. TF41-A-1 turbofan engine schematic.

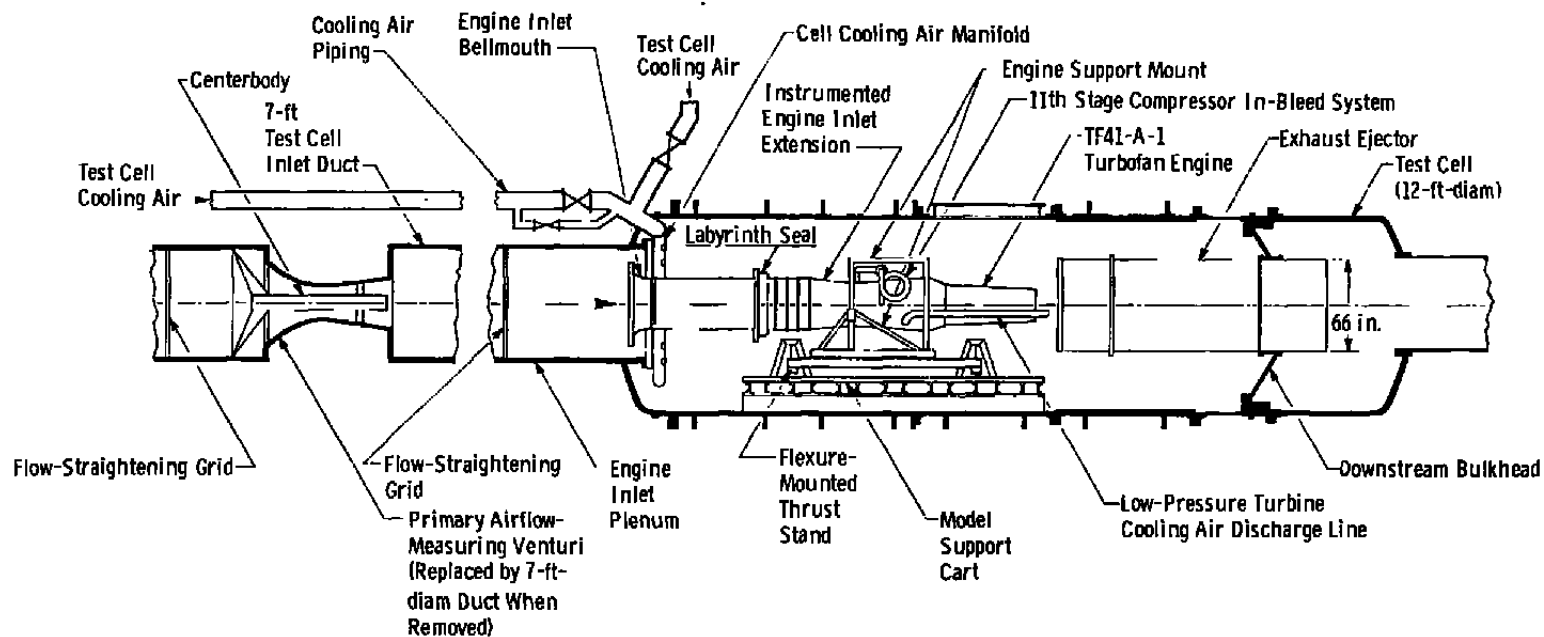


Figure 2. Installation schematic TF41-A-1 in Propulsion Development Test Cell (T-4).

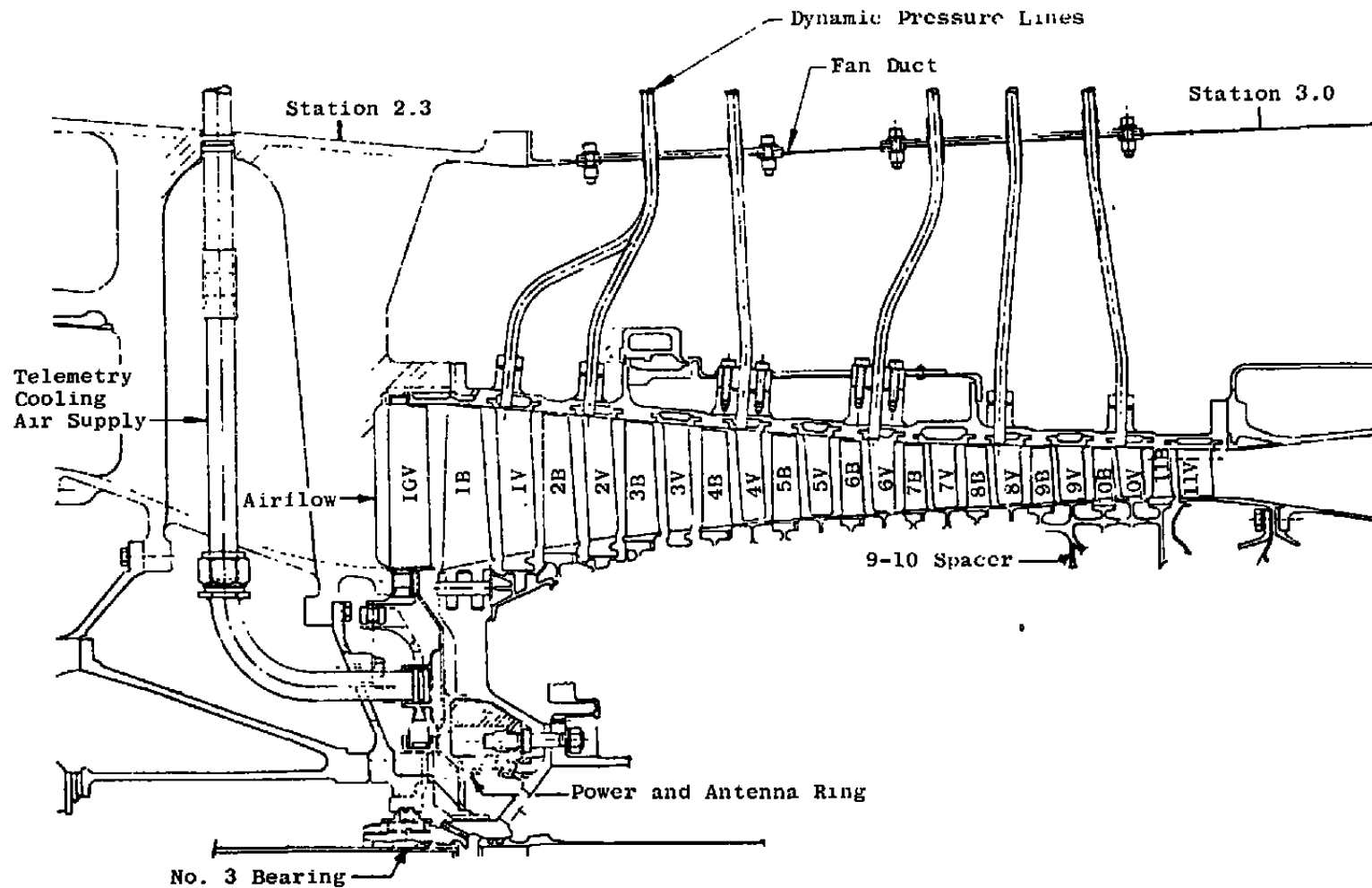
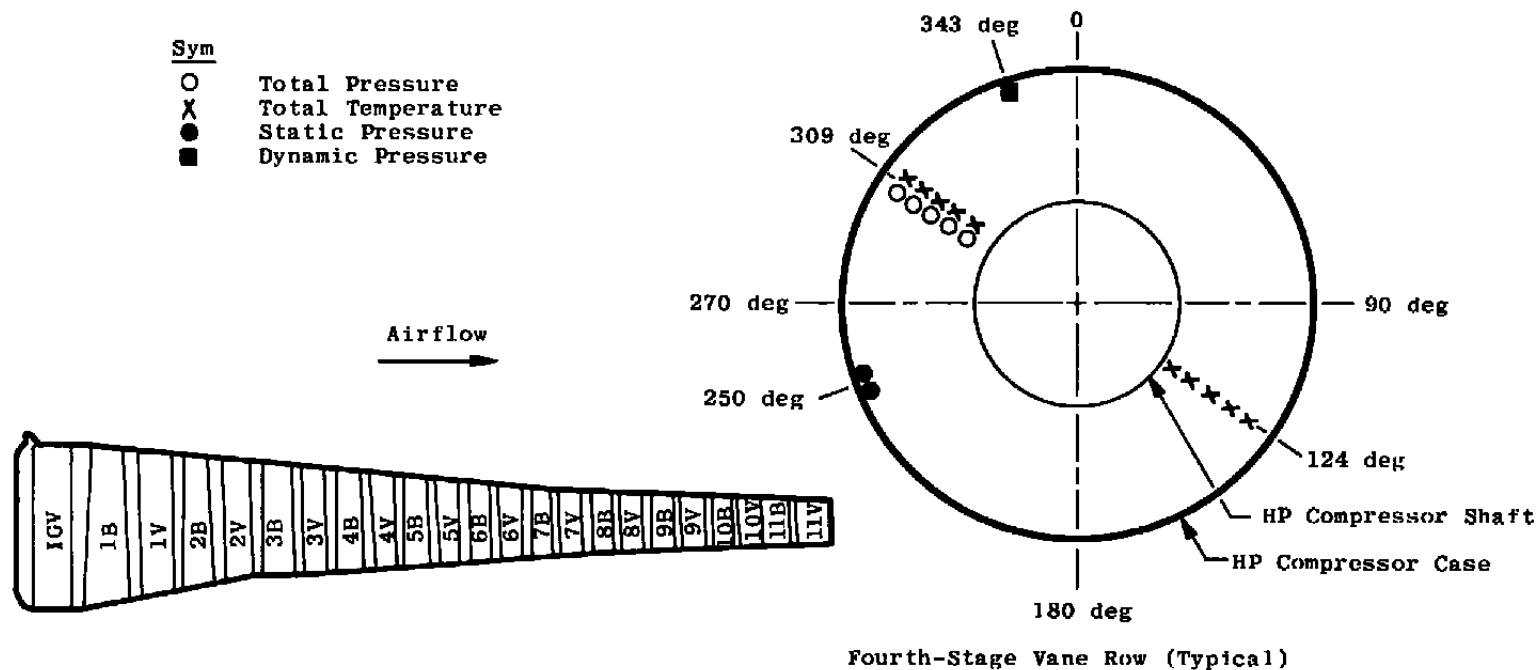


Figure 3. TF41-A-1 (Block 76) HP compressor schematic.



	High-Pressure Compressor											
	IGV	1	2	3	4	5	6	7	8	9	10	11
Vane Total Pressure (Leading Edge)		5	5	5	5	5	6	6	6	6	6	6
Vane Wall Static Pressure		2	2	2	2	2	2	2	2	2	2	2
Vane Total Temperature (Leading Edge)		10	10	10	10	10	6	6	6	6	6	6
Vane High Response Wall Static Pressure		1	1		1		1		1		1	

Figure 4. HP compressor interstage instrumentation.

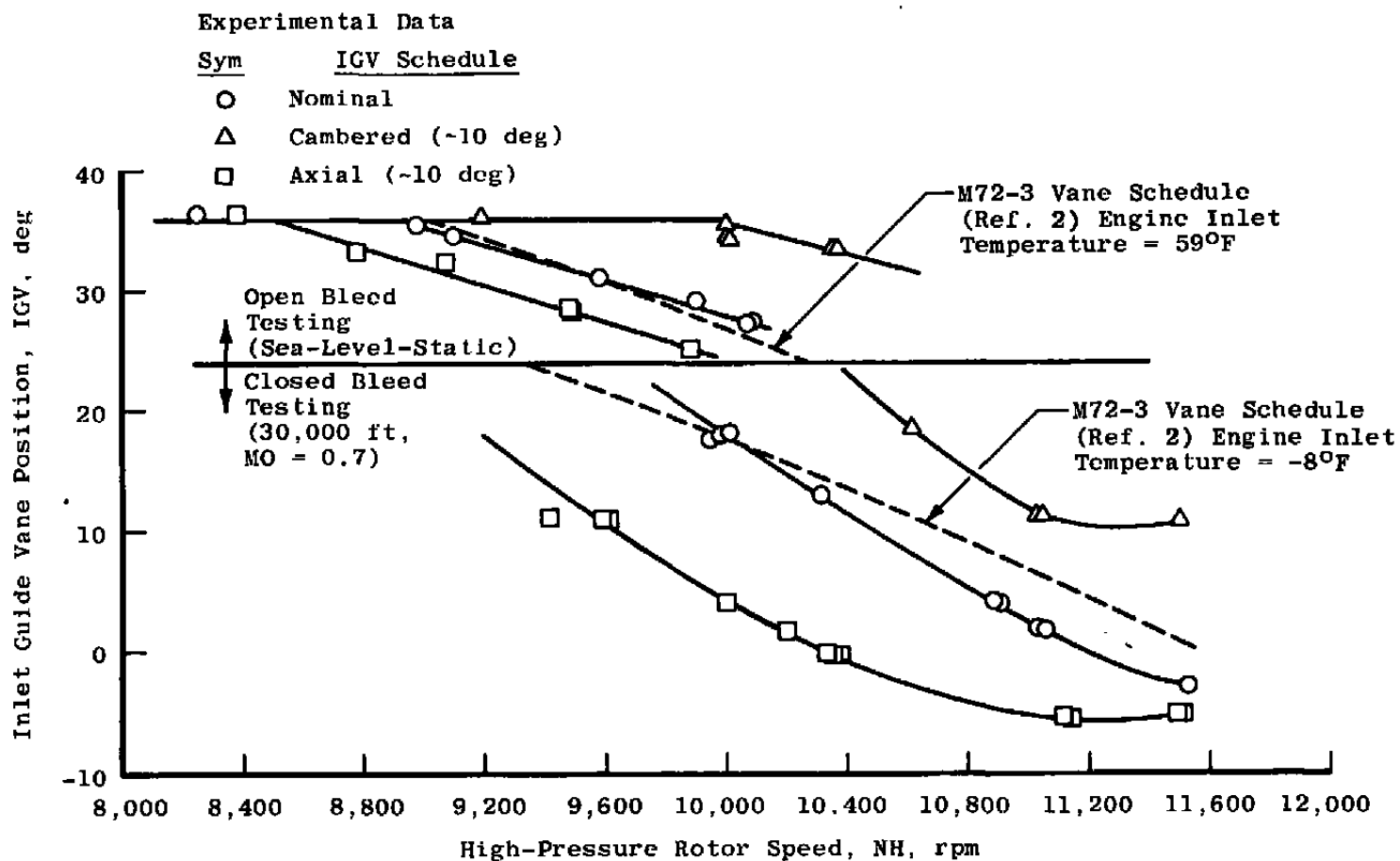


Figure 5. TF41-A-1 IGV schedules.

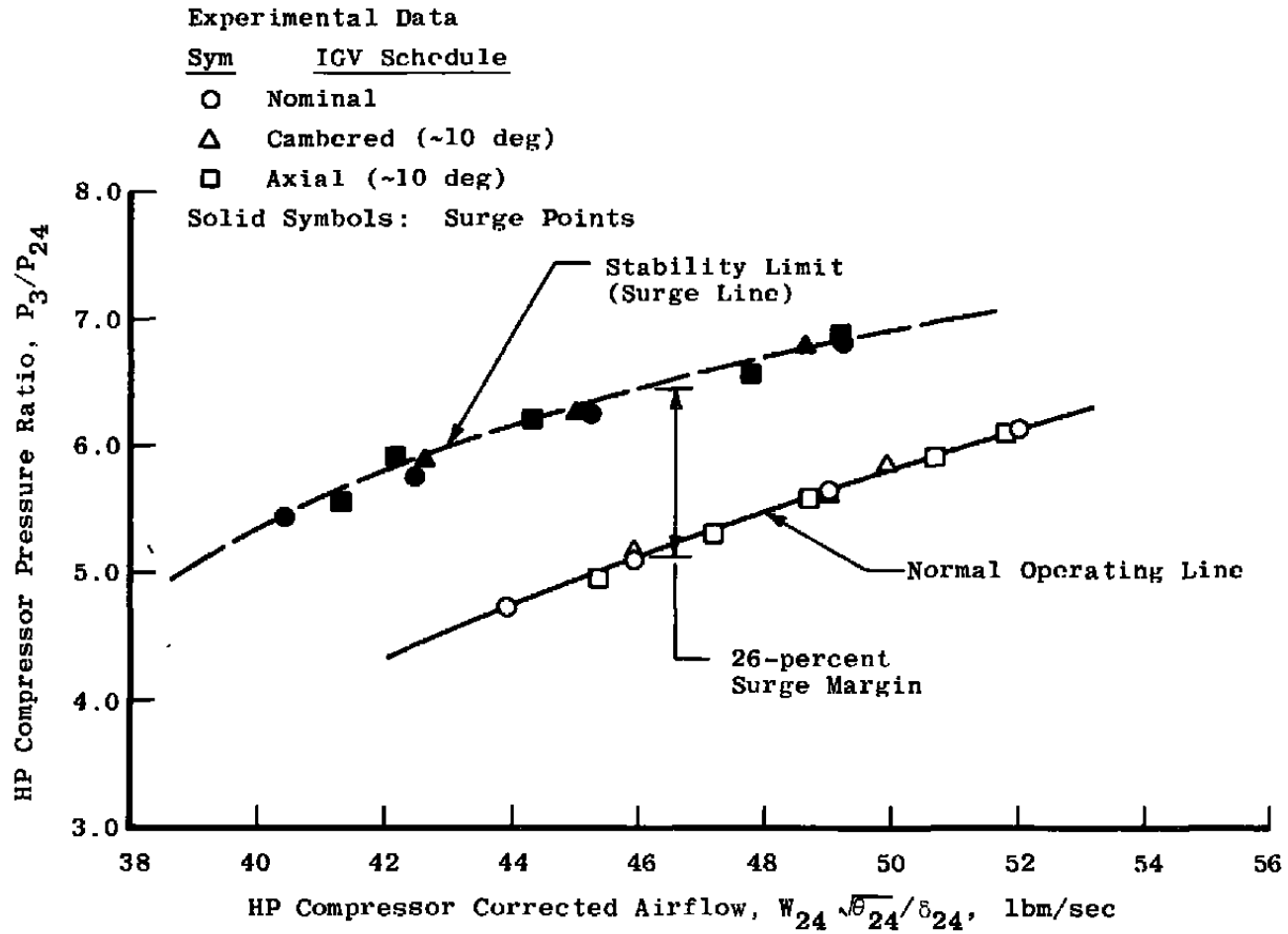


Figure 6. Effects of IGV schedule on TF41-A-1 HP compressor stability limit at 30,000 ft, Mach number 0.7 with seventh-stage bleed valve closed.

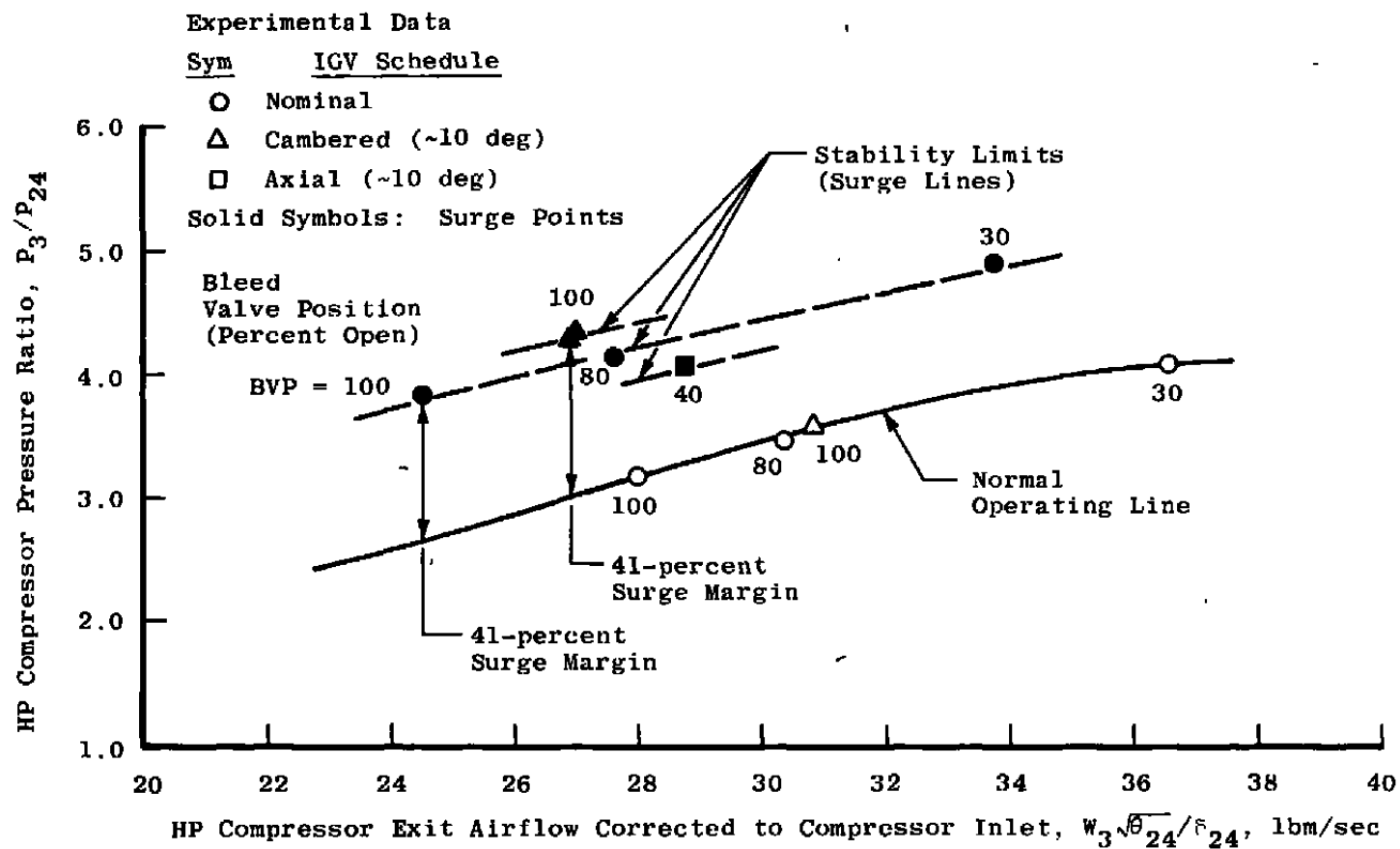


Figure 7. Effects of IGV schedule on TF41-A-1 HP compressor stability limit at sea-level-static conditions with seventh-stage bleed valve open.

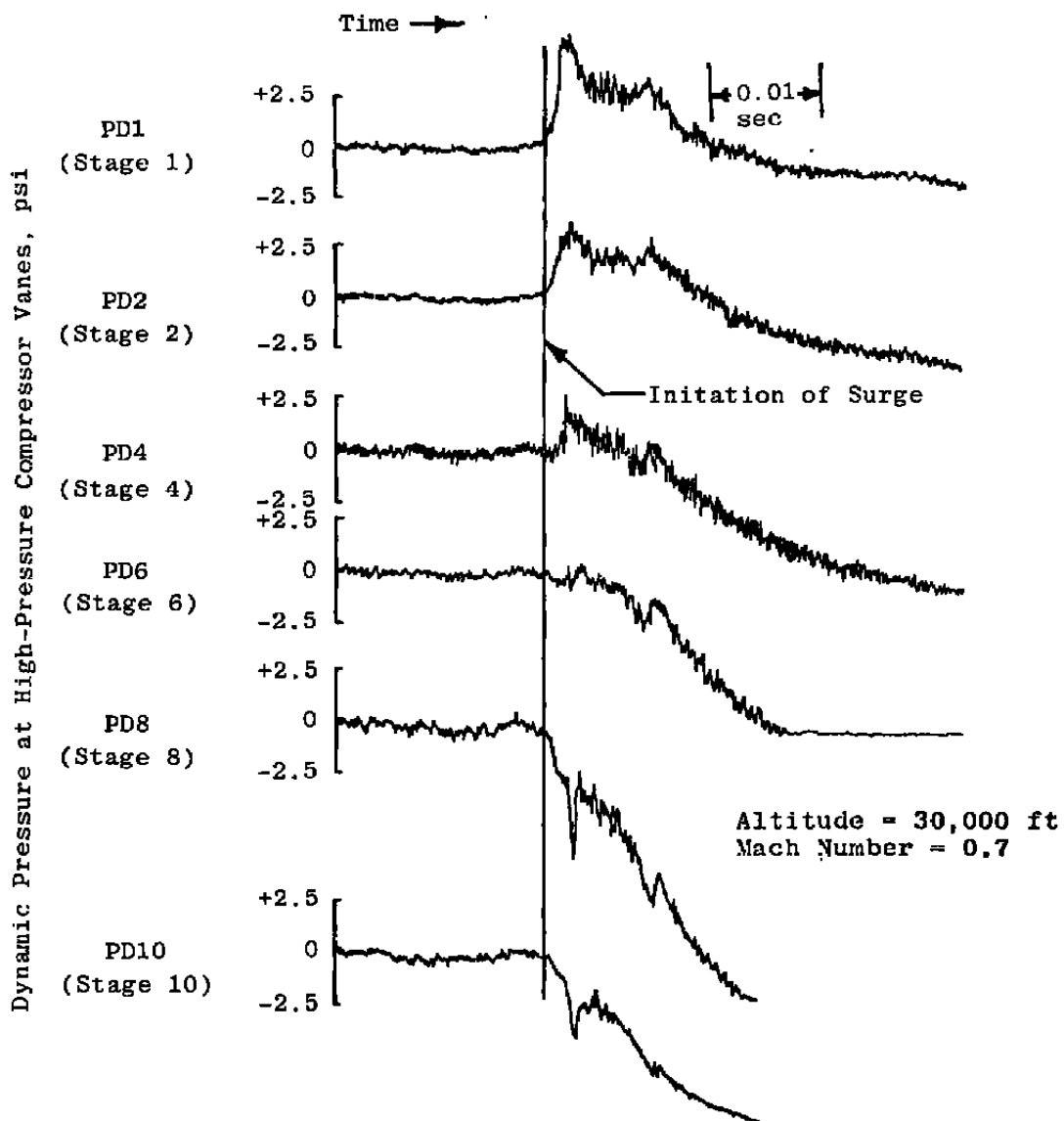
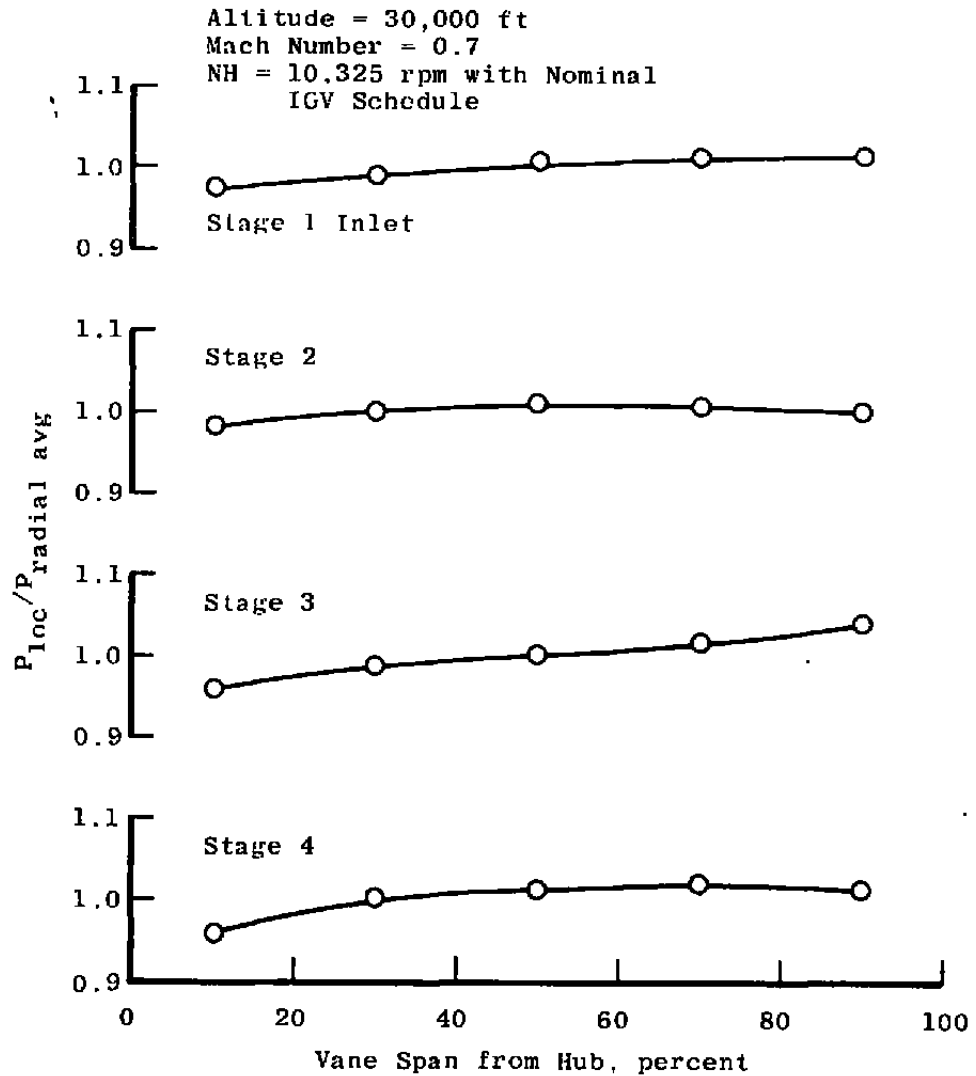


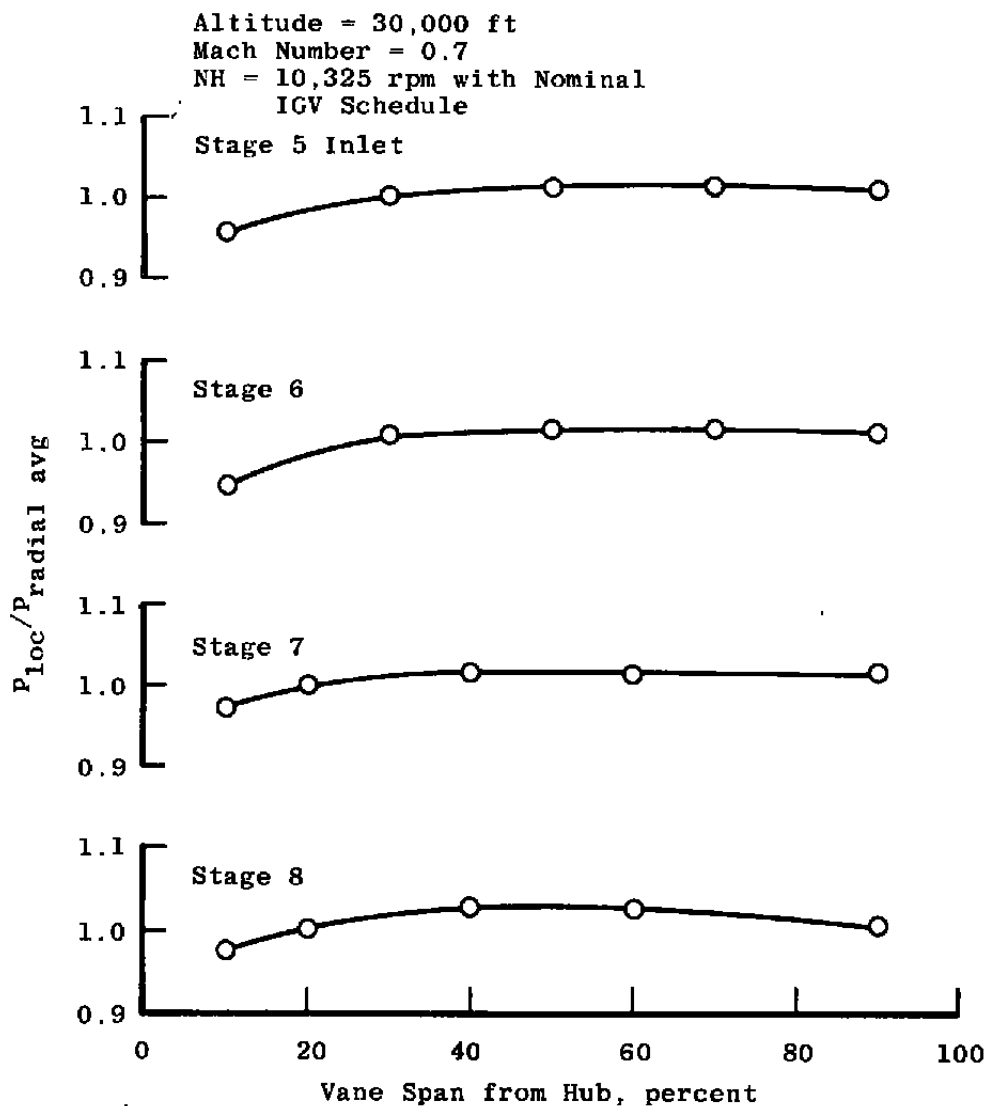
Figure 8. Surge induced by inbleed at  $NH = 11,500$  rpm with axial IGV schedule.



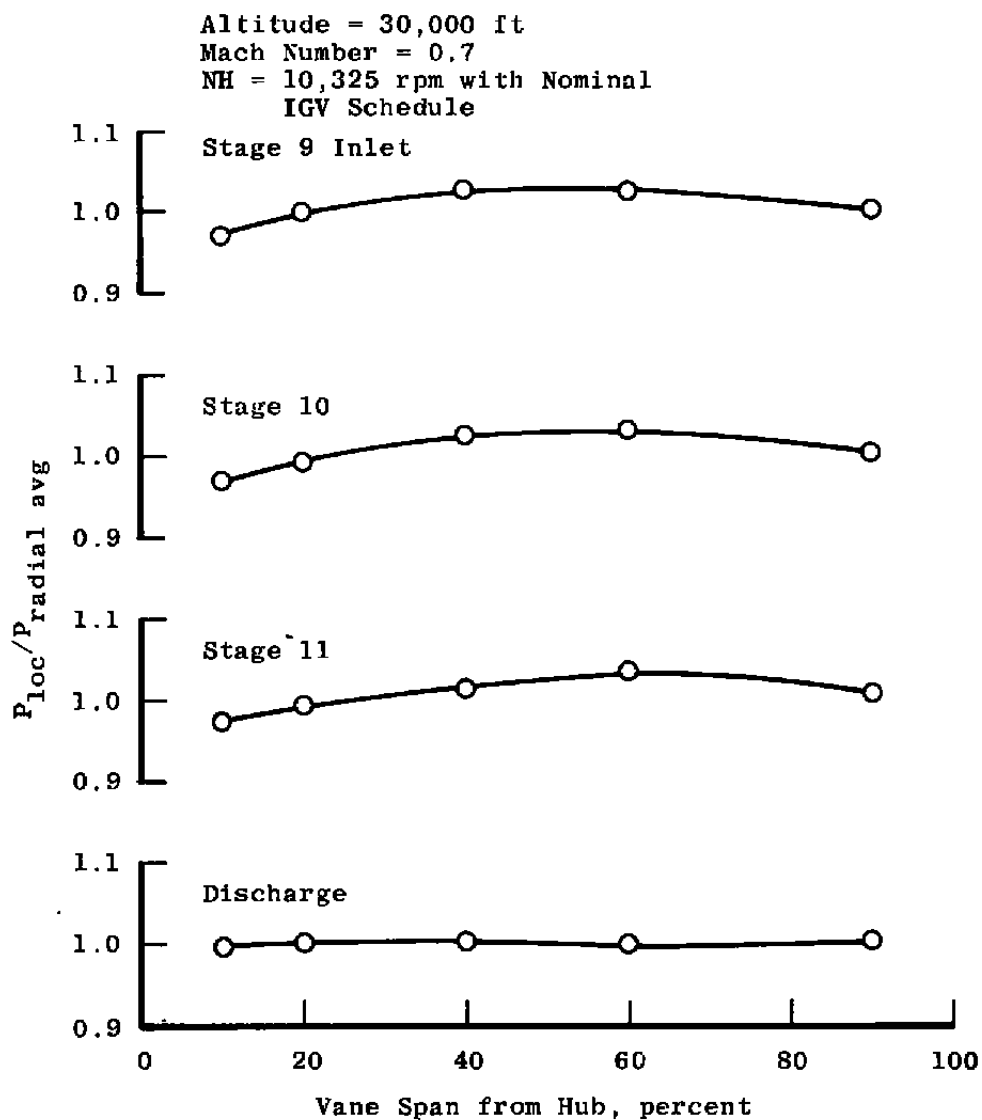


a. Stages 1 through 4

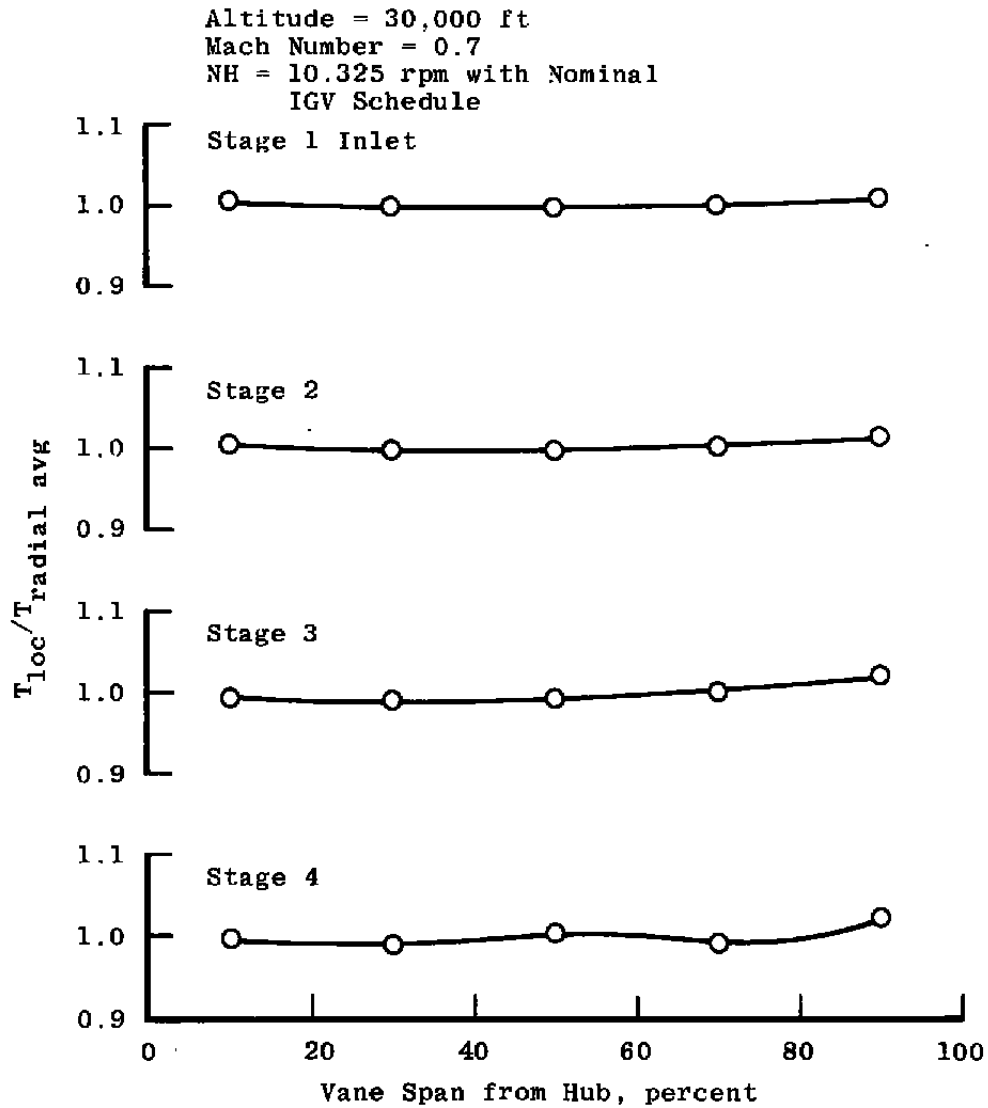
Figure 9. Radial total pressure profiles with uniform engine inlet flow.



b. Stages 5 through 8  
Figure 9. Continued.

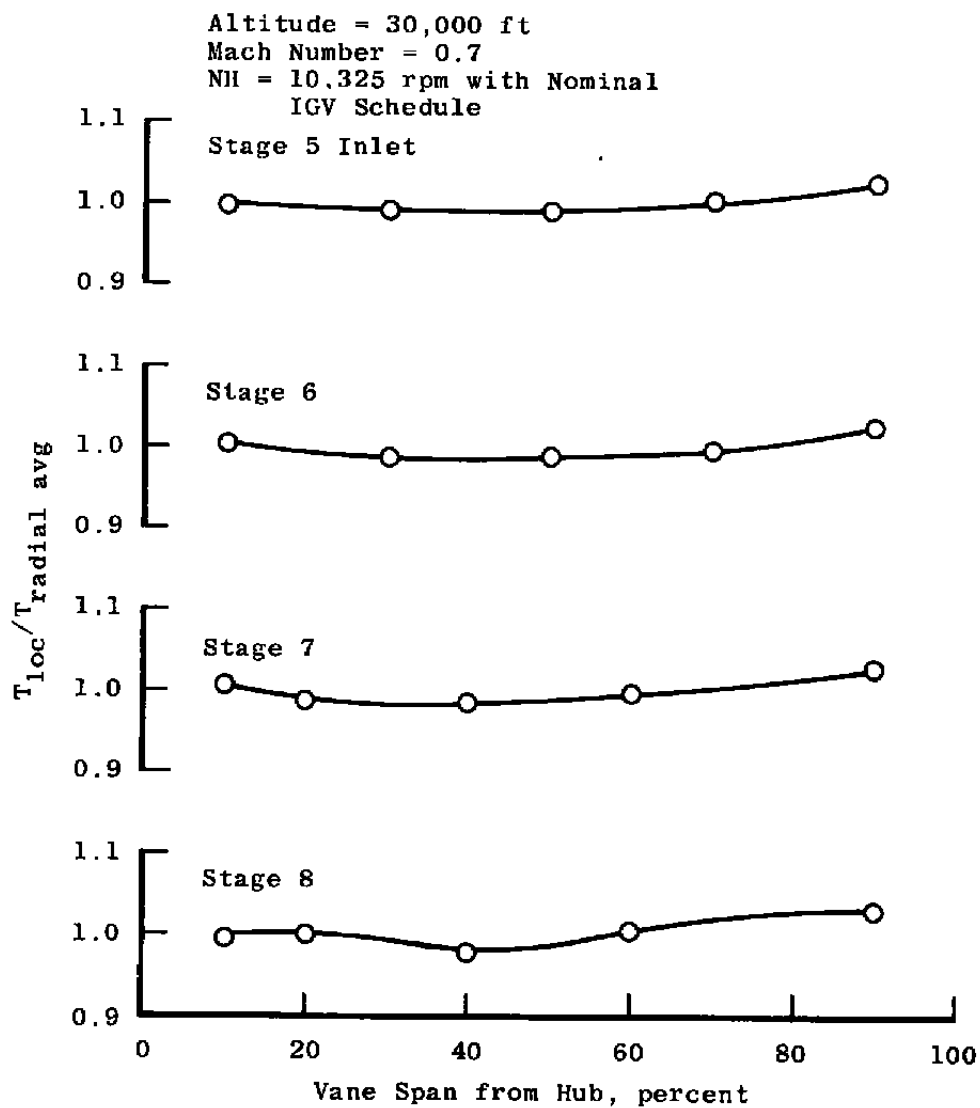


c. Stages 9 through discharge  
 Figure 9. Concluded.

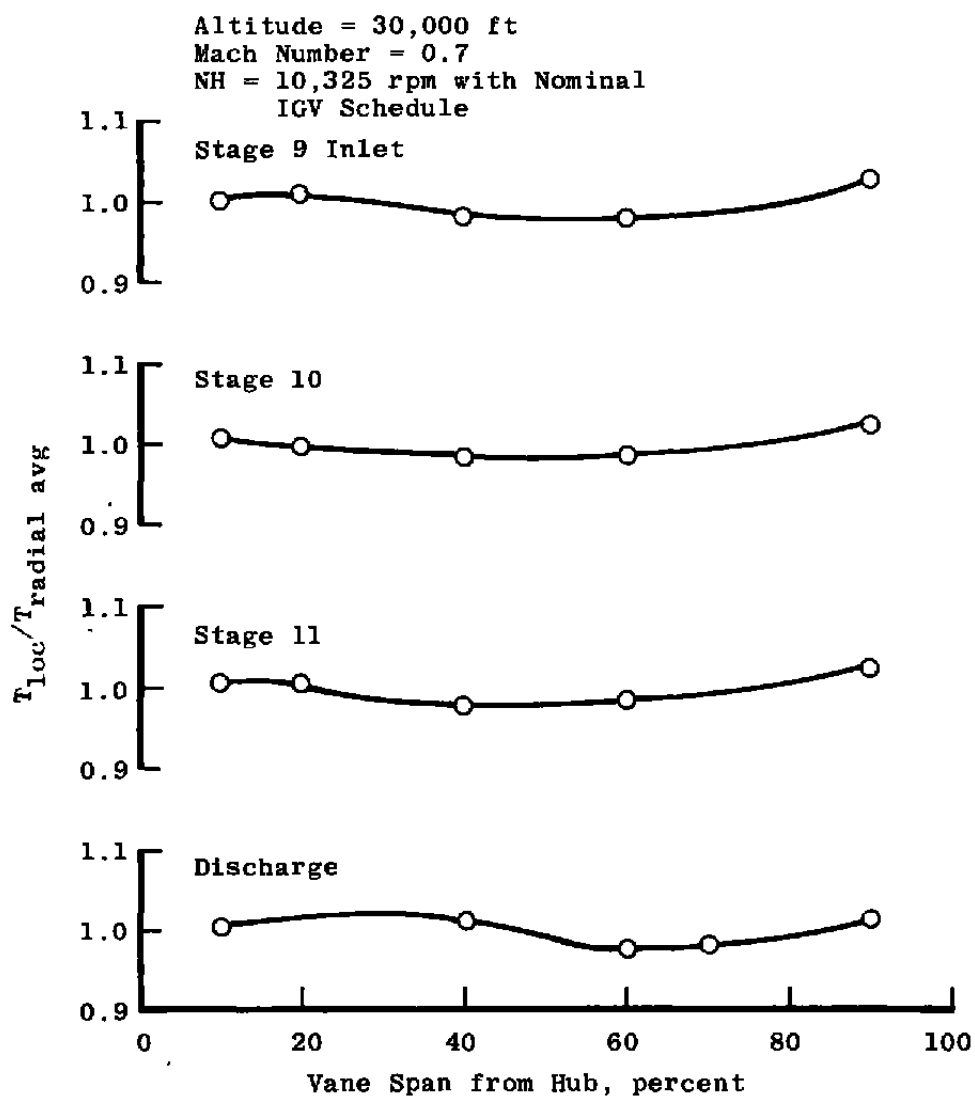


a. Stages 1 through 4

Figure 10. Radial total temperature profiles with uniform engine inlet flow.



b. Stages 5 through 8  
Figure 10. Continued.



c. Stages 9 through discharge  
Figure 10. Concluded.

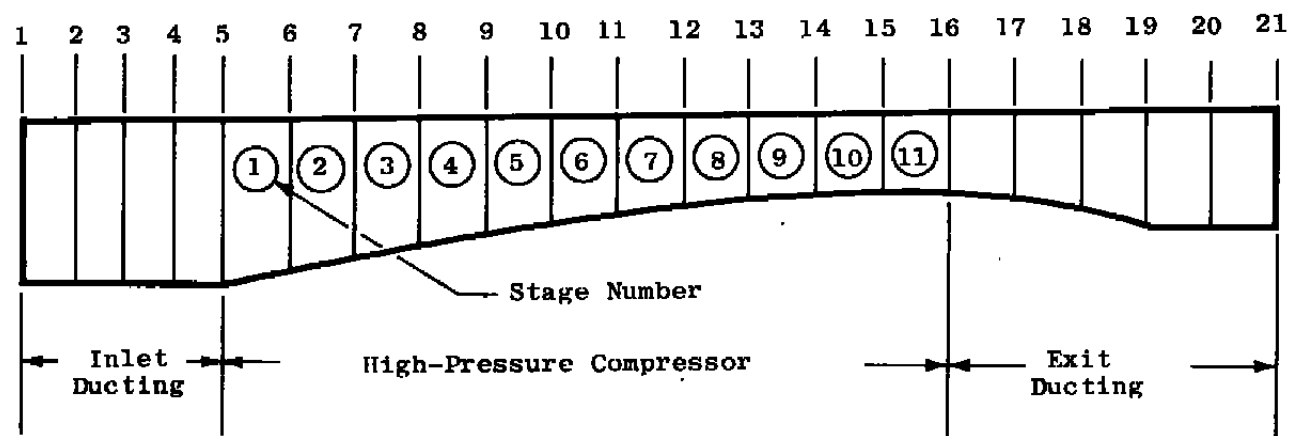


Figure 11. Station locations (computational planes) for one-dimensional, steady-state compressor model.

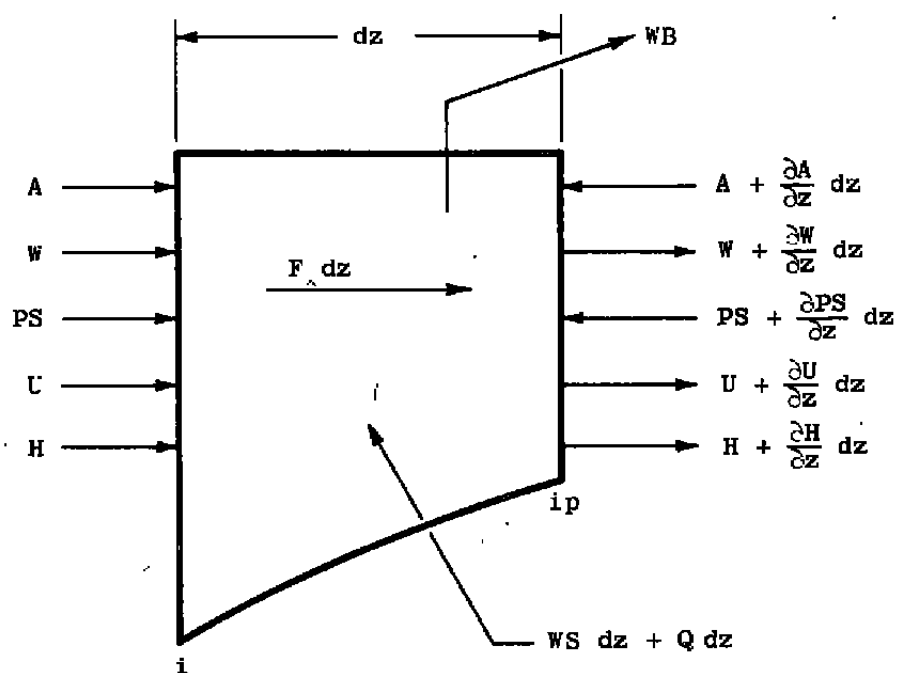


Figure 12. Elemental control volume with application of mass, momentum, and energy conservation principles.



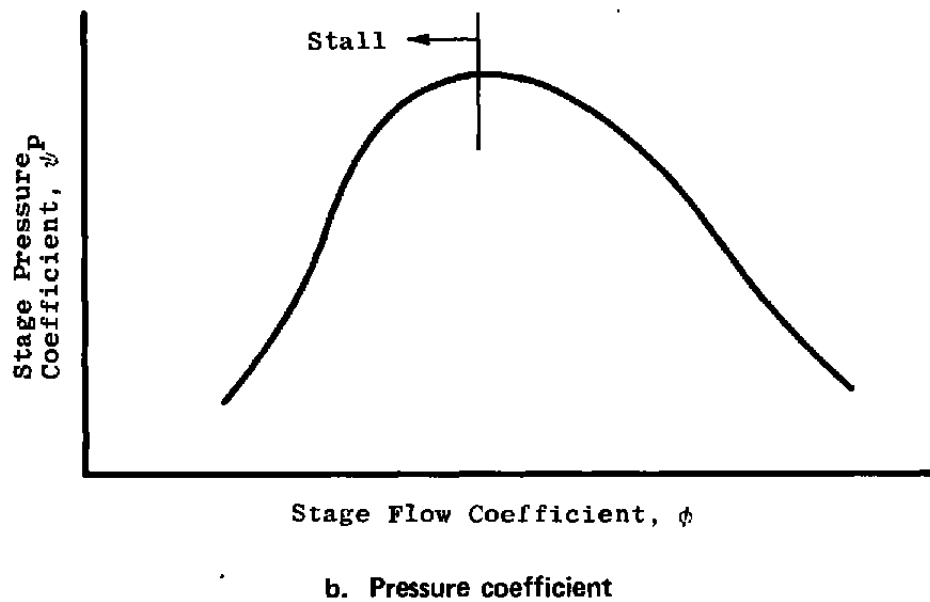
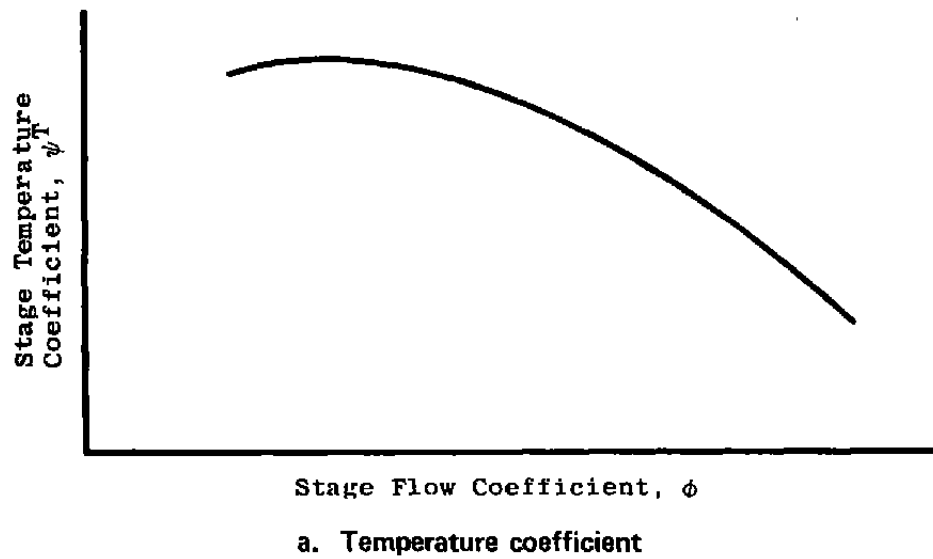
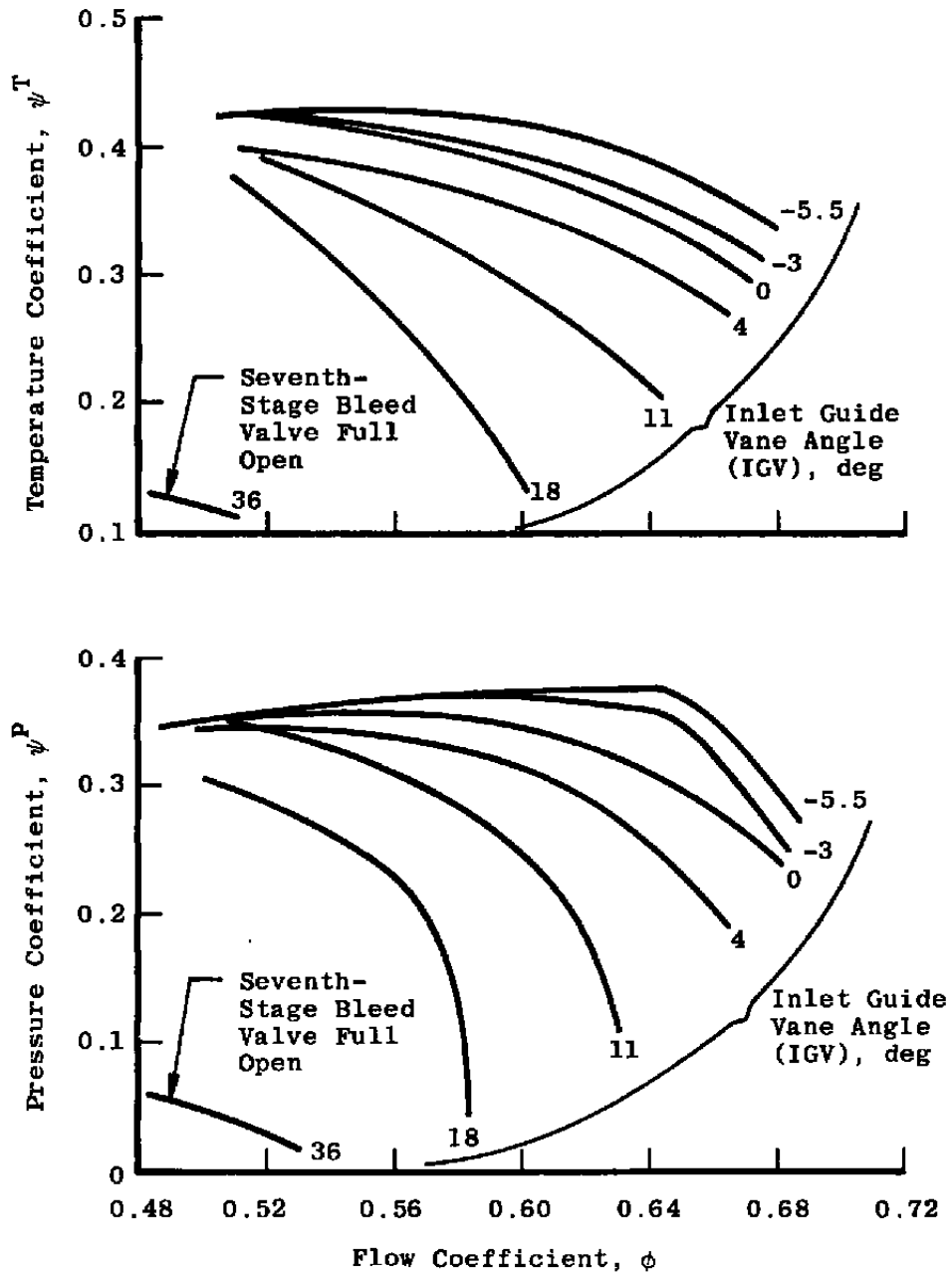
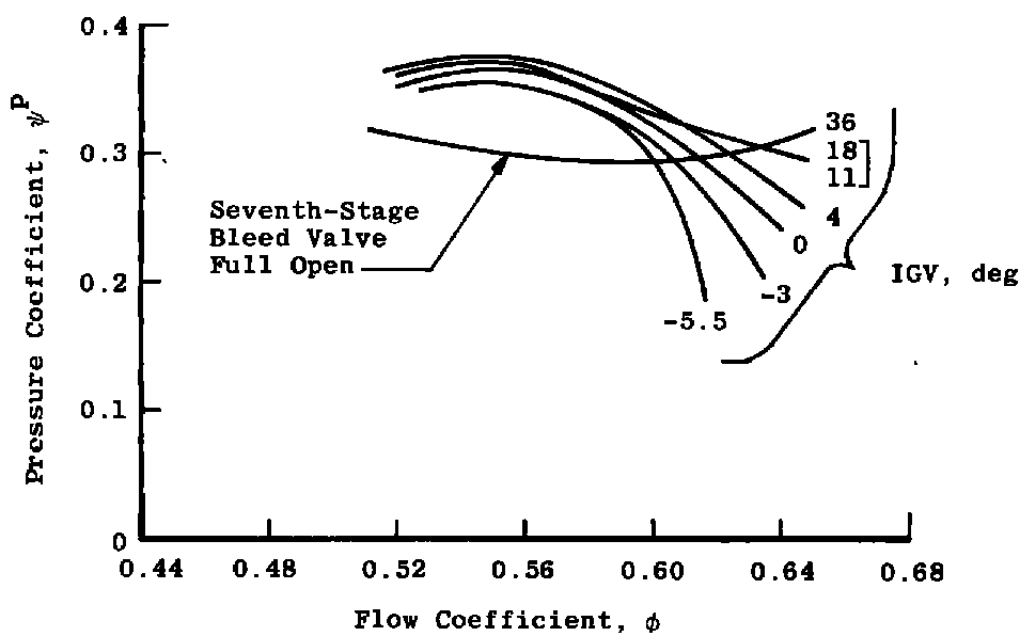
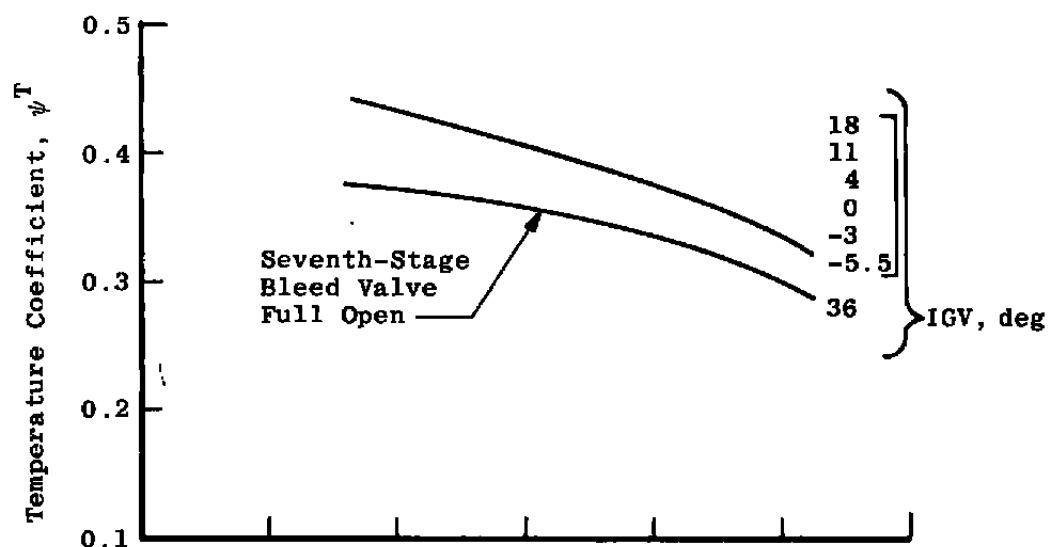


Figure 13. Typical temperature and pressure coefficients as functions of flow coefficient at constant rotational speed.

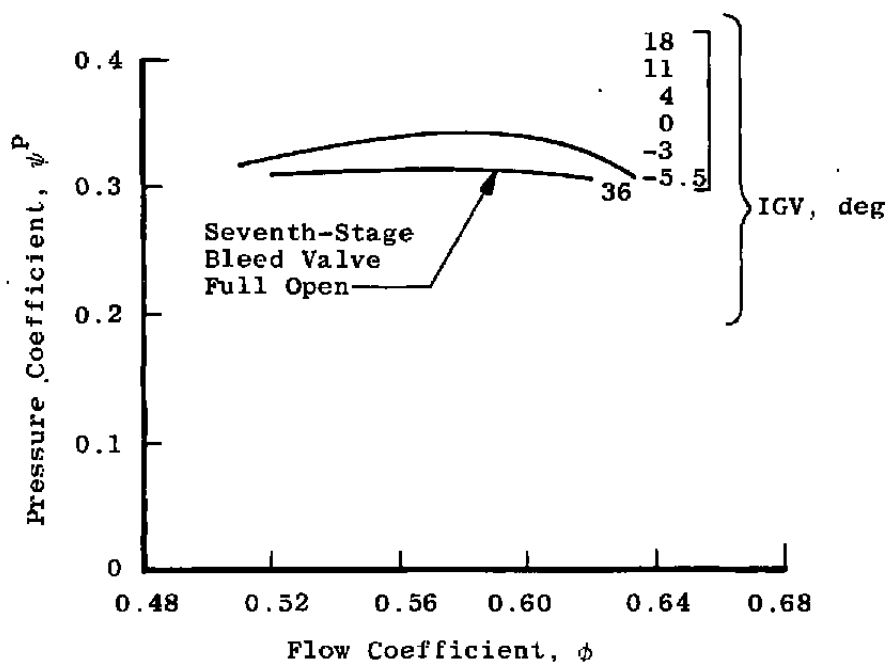
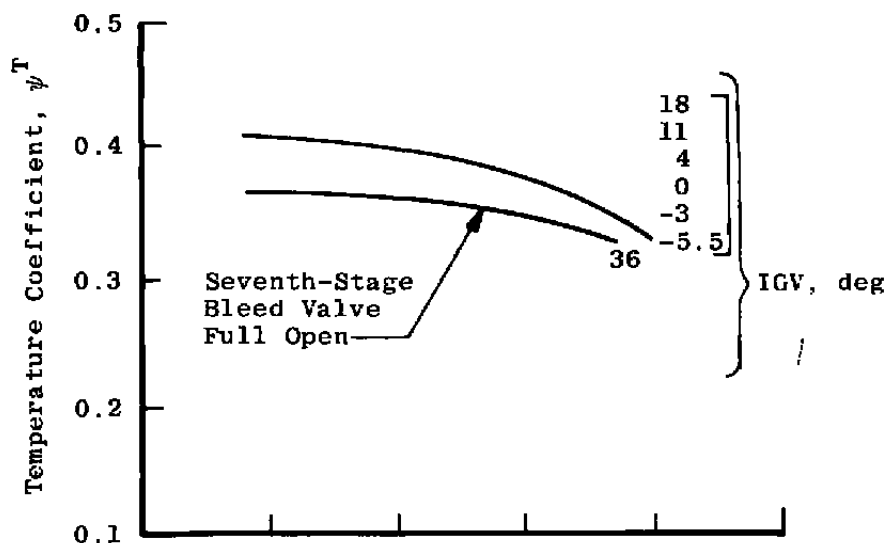


a. Stage 1

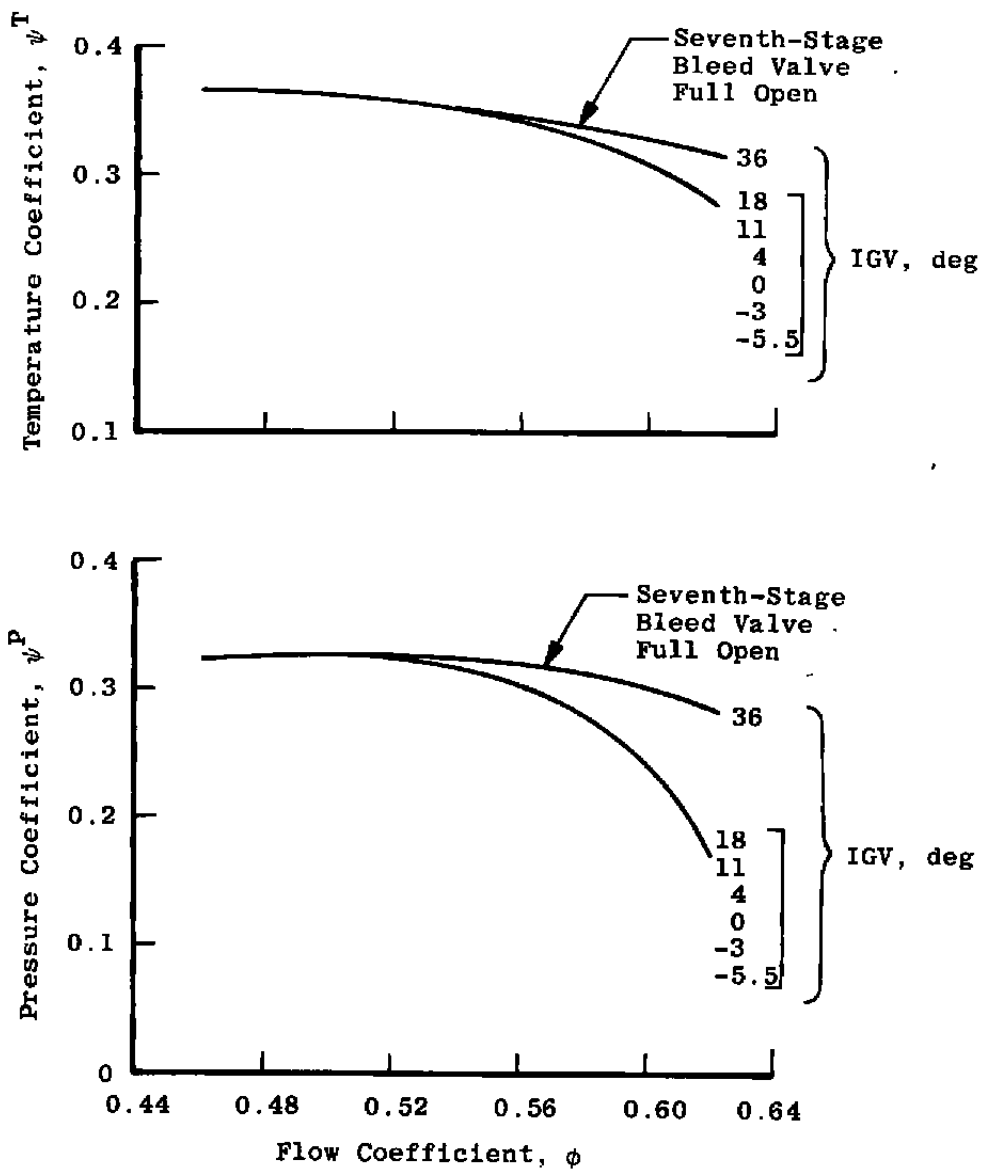
Figure 14. TF41-A-1 HP compressor stage characteristics.



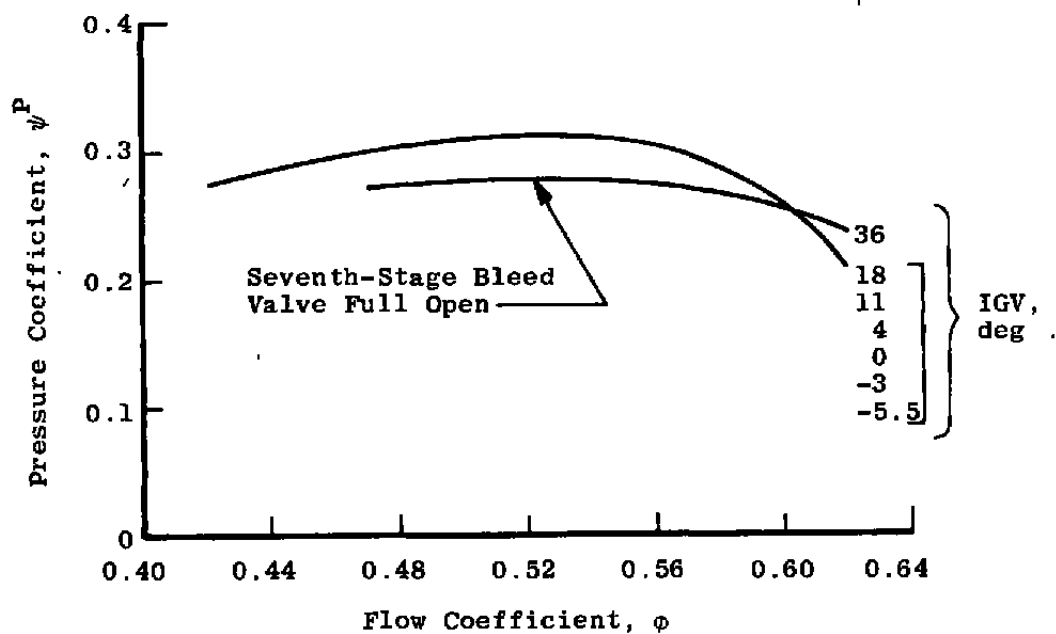
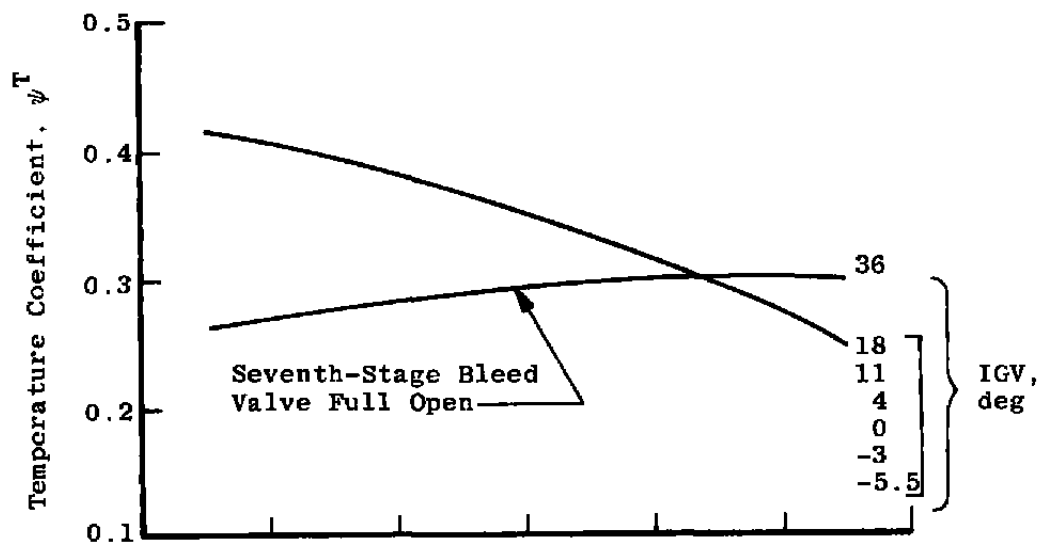
b. Stage 2  
Figure 14. Continued.



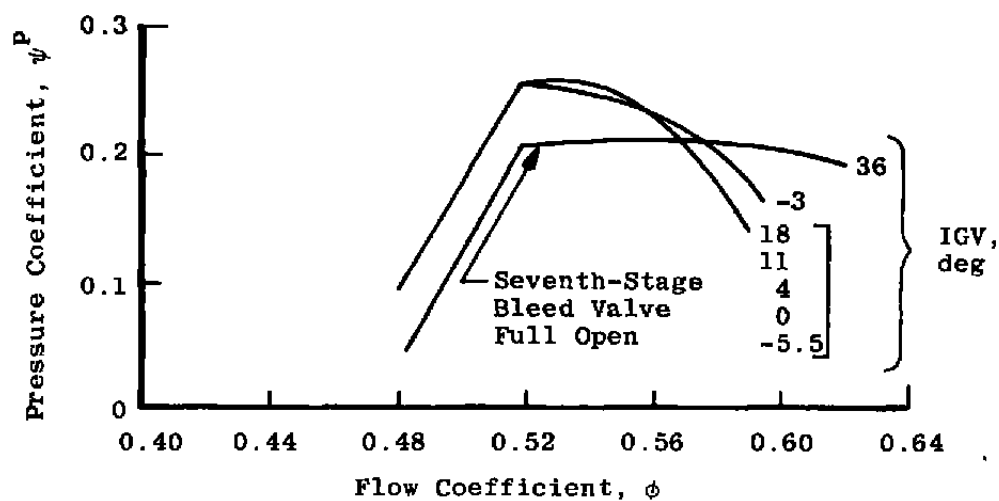
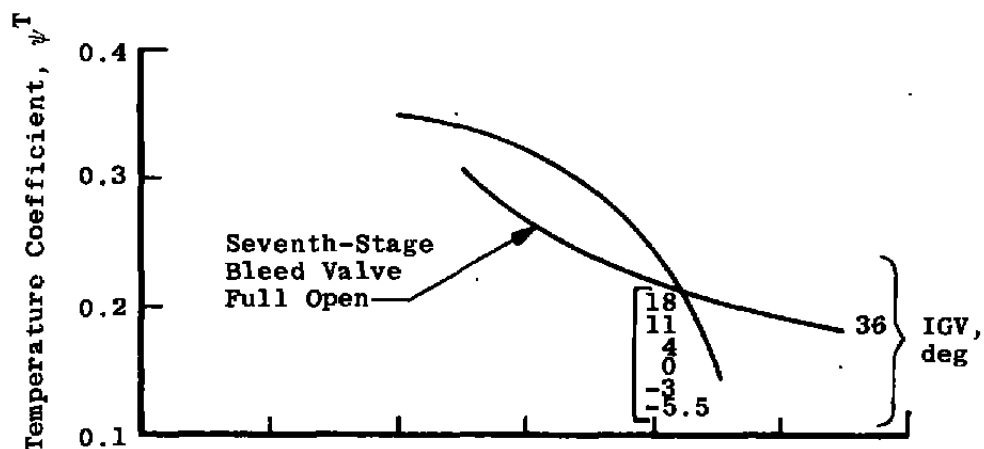
c. Stage 3  
Figure 14. Continued.



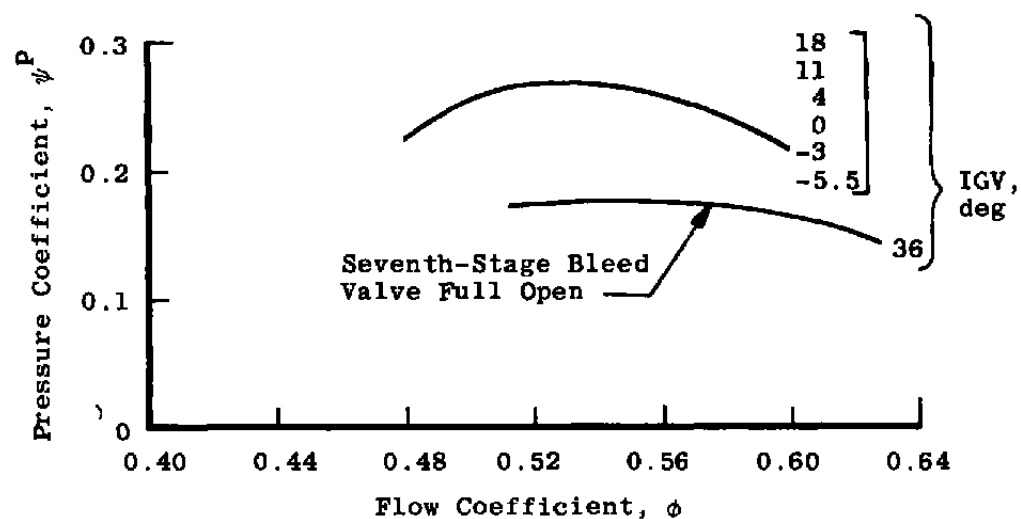
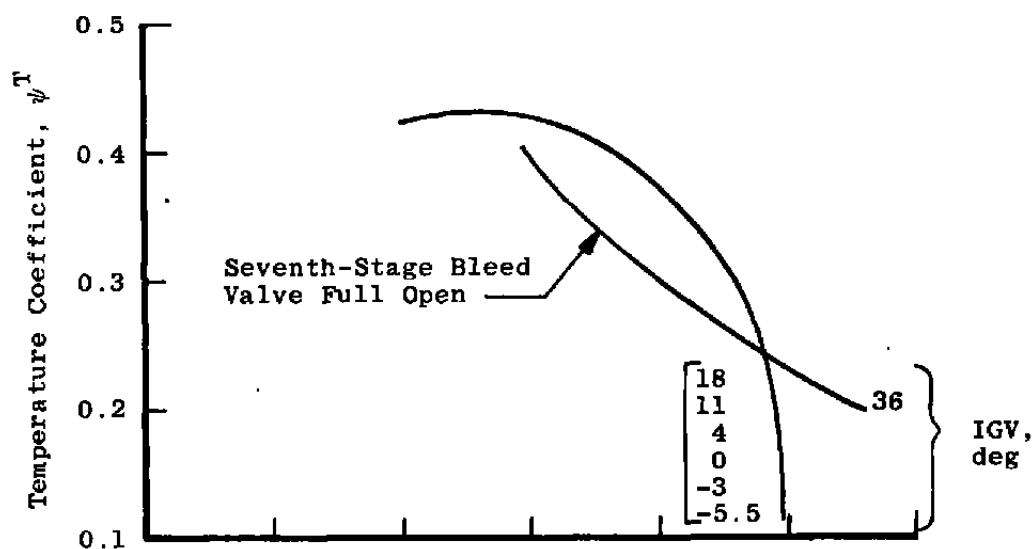
d. Stage 4  
Figure 14. Continued.



e. Stage 5  
Figure 14. Continued.

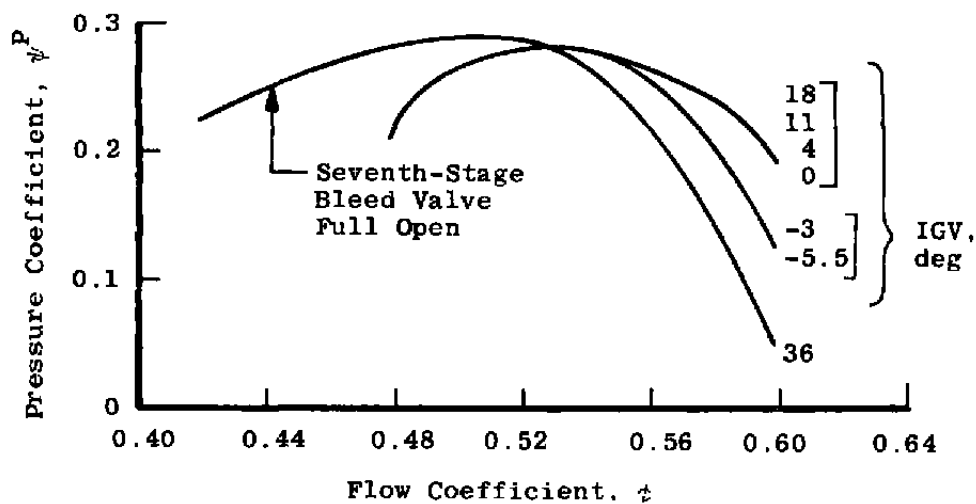
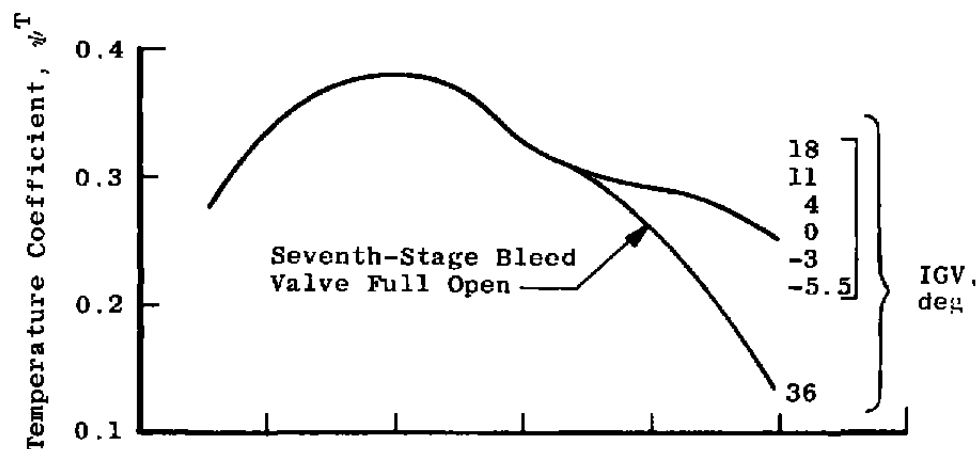


f. Stage 6  
Figure 14. Continued.

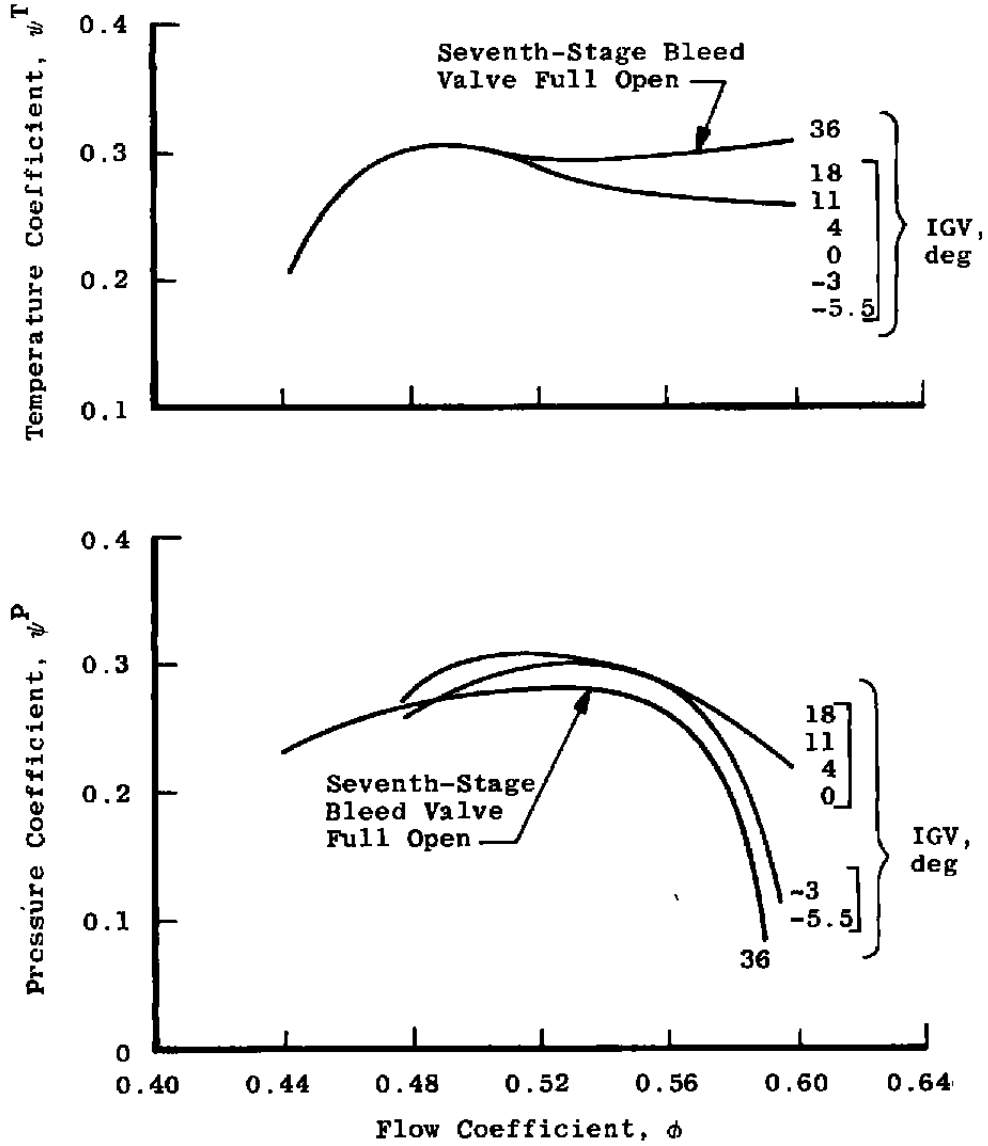


g. Stage 7  
Figure 14. Continued.

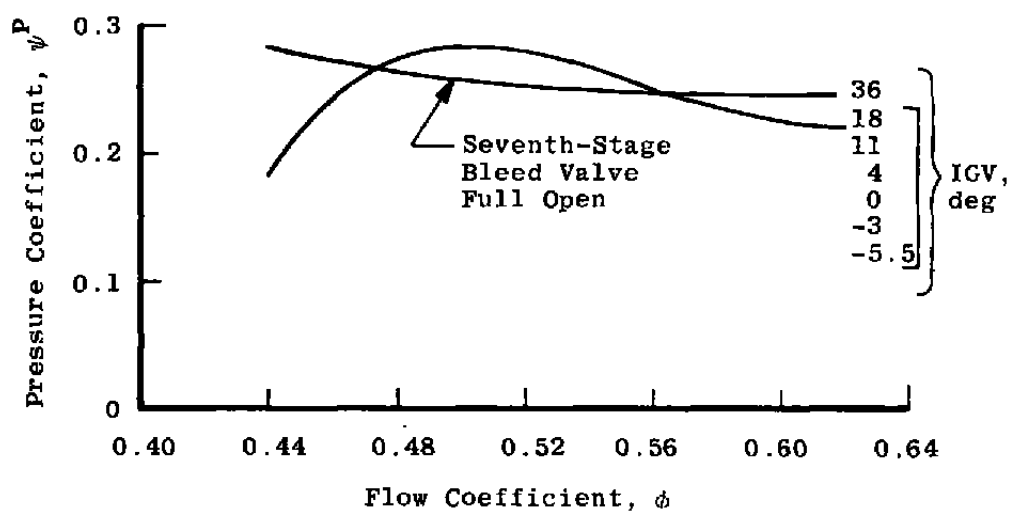
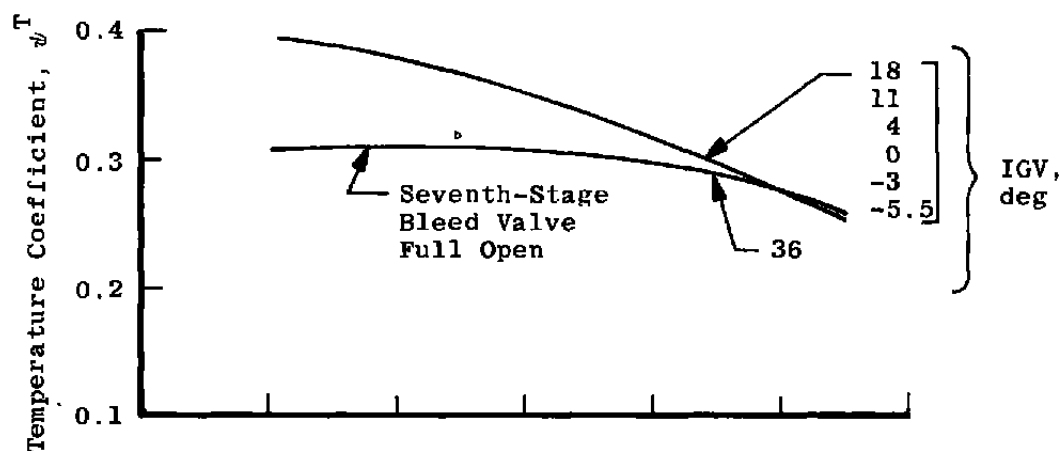




h. Stage 8  
Figure 14. Continued.

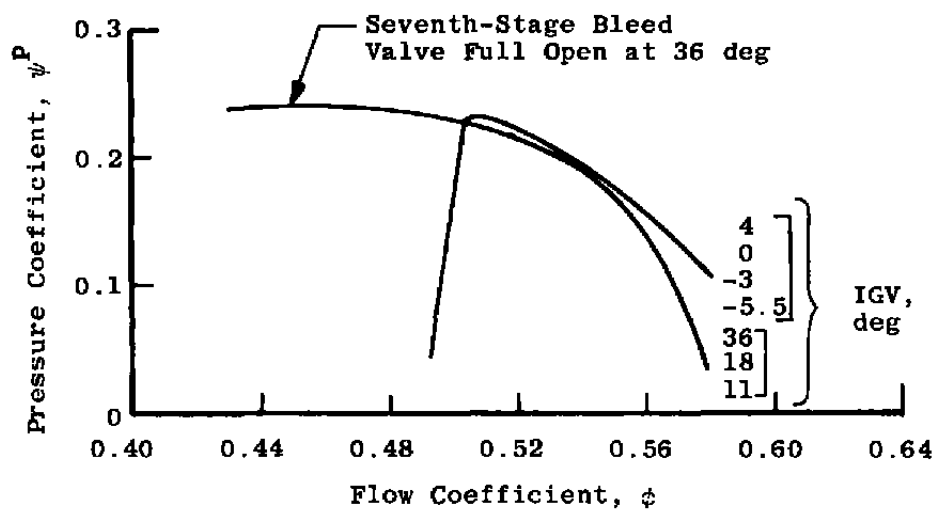
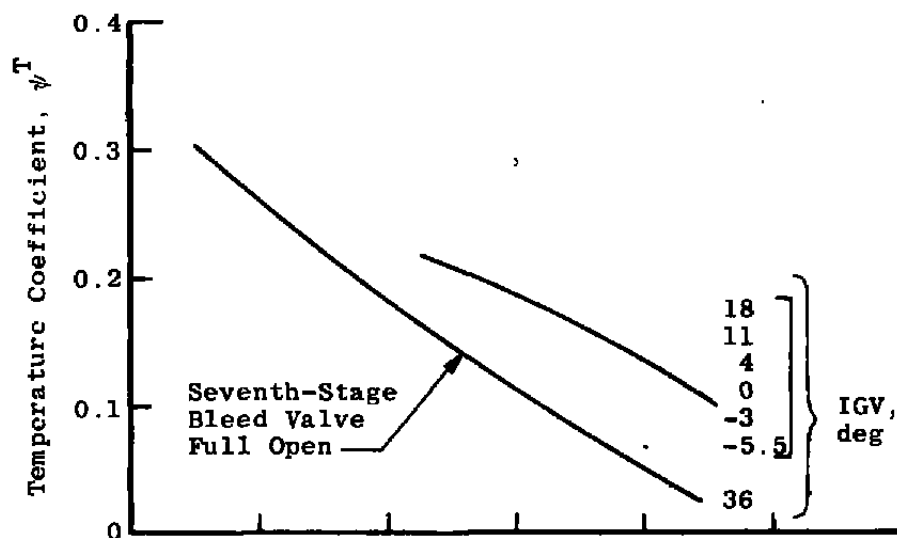


i. Stage 9  
Figure 14. Continued.



j. Stage 10

Figure 14. Continued.



k. Stage 11  
Figure 14. Concluded.

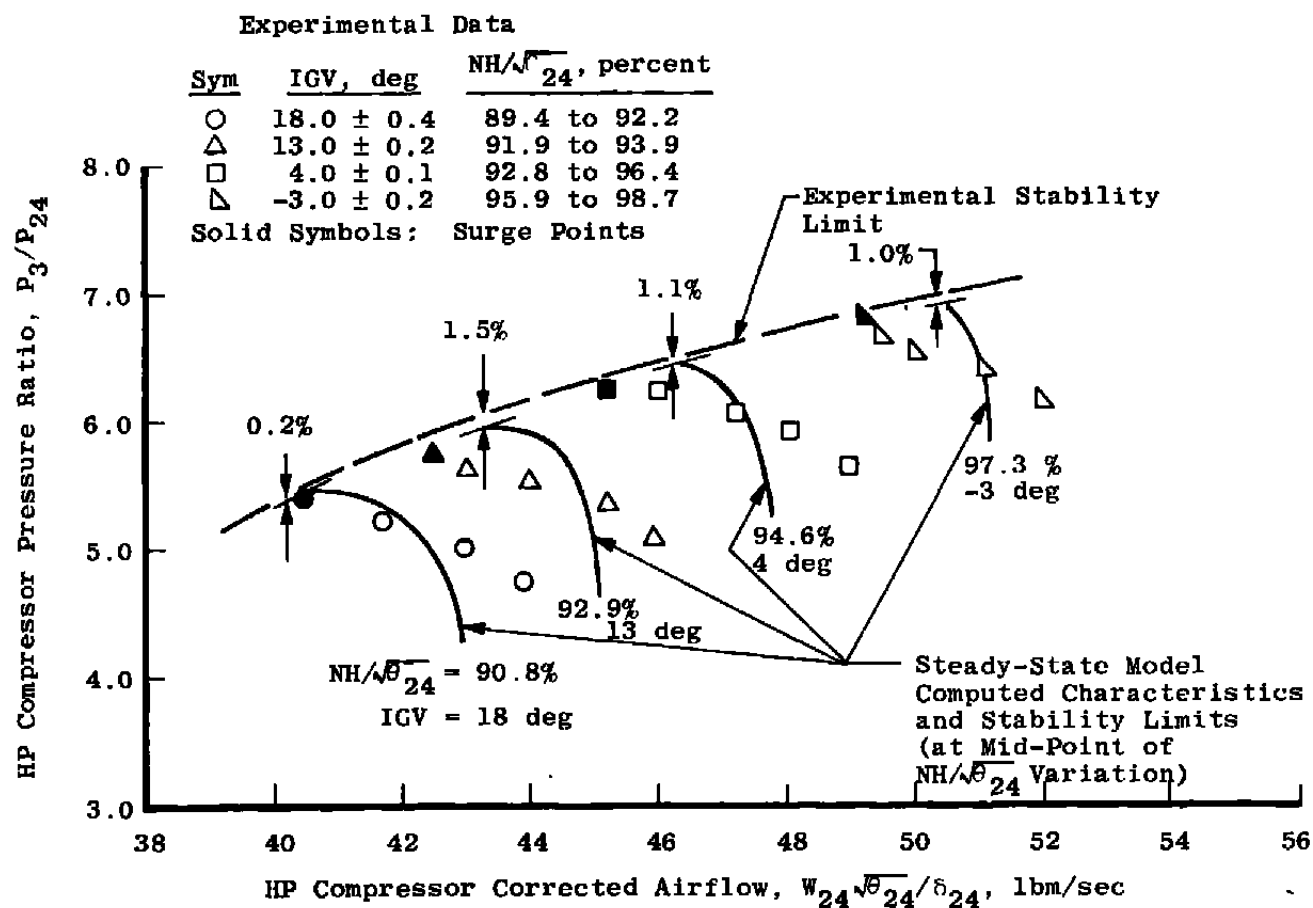
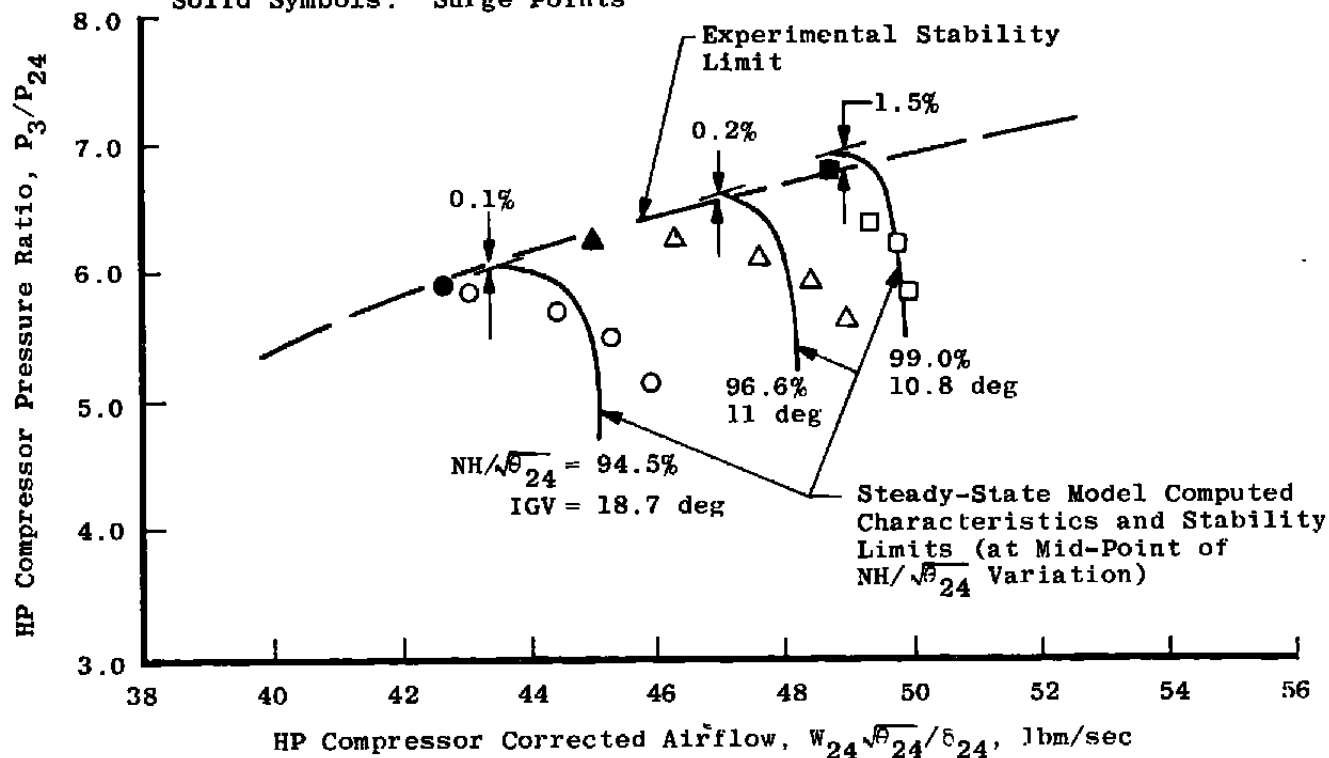


Figure 15. Comparison of model computed speed characteristics and stability limits with Experimental measurements at 30,000 ft, MO = 0.7.

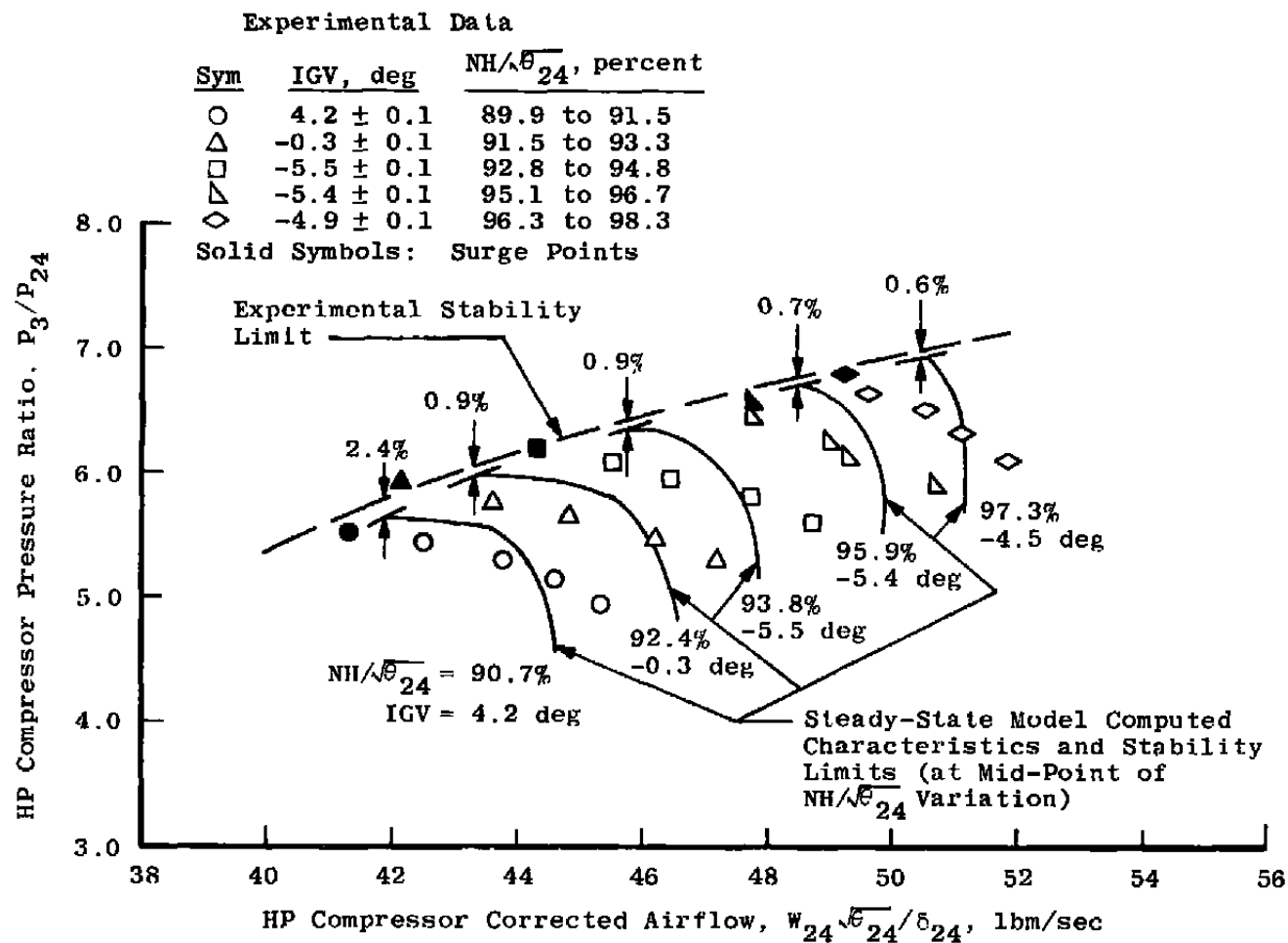
## Experimental Data

Sym	IGV, deg	$NH/\sqrt{\theta_{24}}$ , percent
○	$18.7 \pm 0.1$	93.1 to 95.9
△	$11.0 \pm 0.2$	95.4 to 97.8
□	$10.8 \pm 0.1$	98.0 to 100.0

Solid Symbols: Surge Points



b. Cambered IGV schedule  
Figure 15. Continued.



c. Axial IGV schedule  
Figure 15. Concluded.

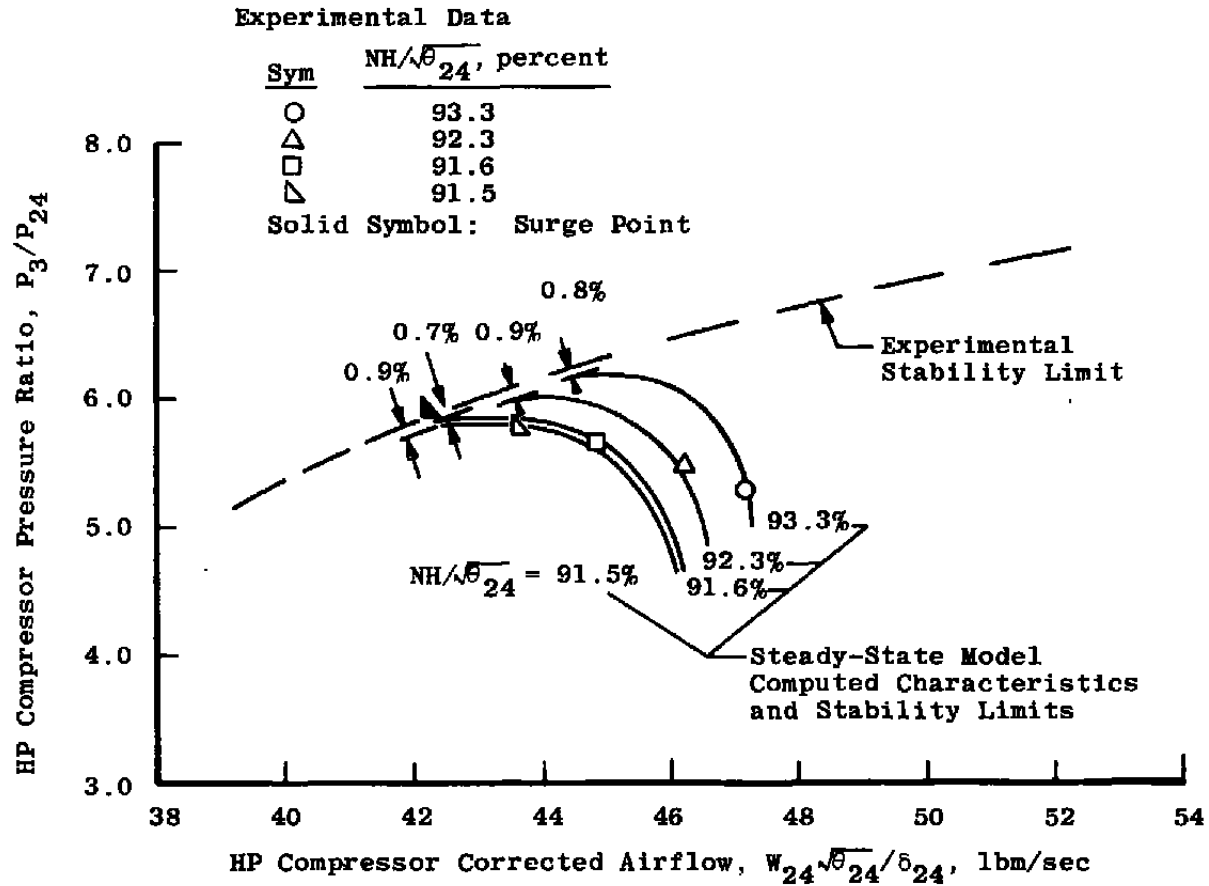


Figure 16. Model computed effect of corrected rotor speed variation for -0.3-deg IGV line axial IGV schedule at 30,000 ft,  $MO = 0.7$ .



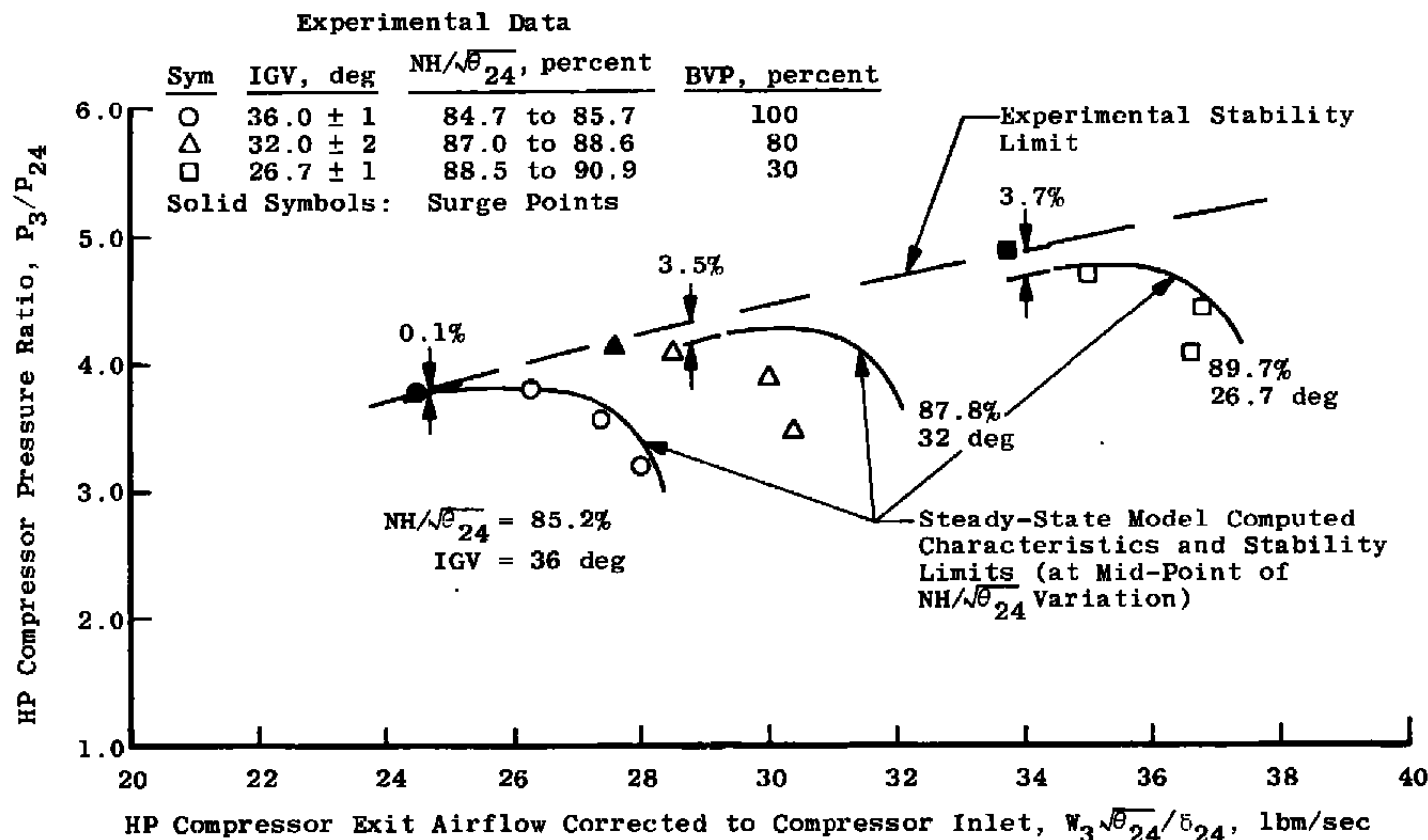
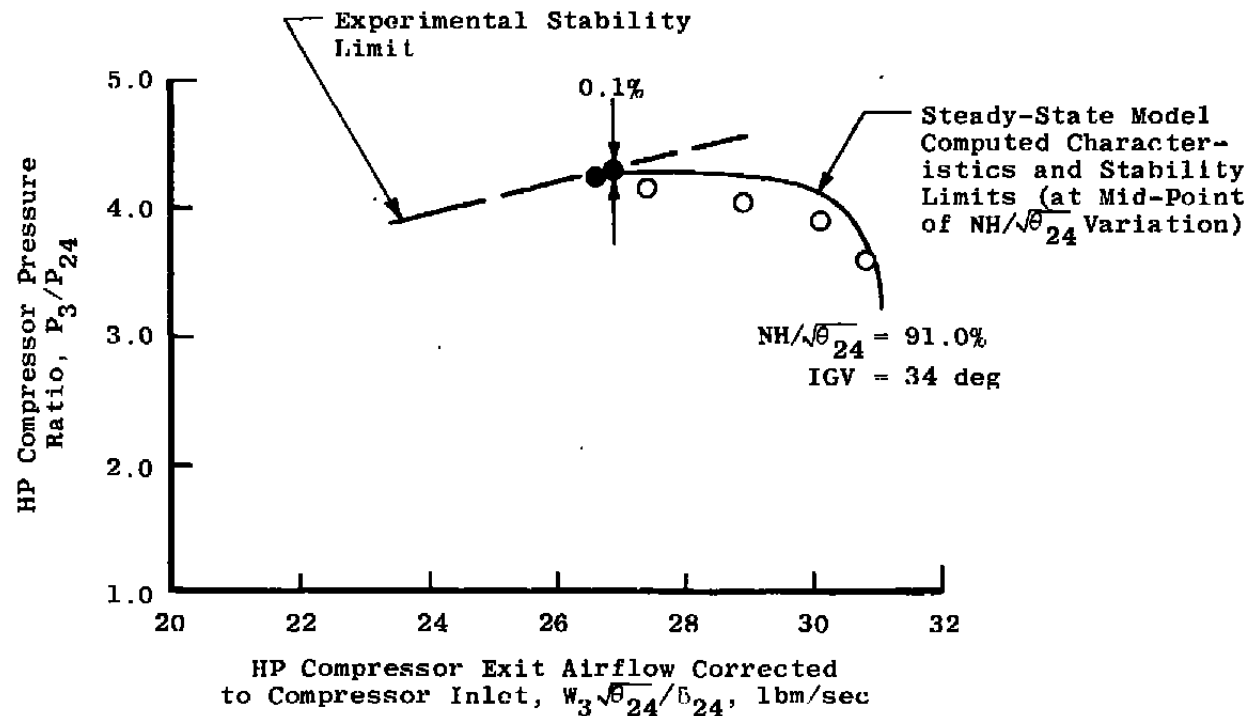


Figure 17. Comparison of model computed speed characteristics and stability limits with experimental measurements with seventh-stage bleed valve open at sea-level-static conditions.

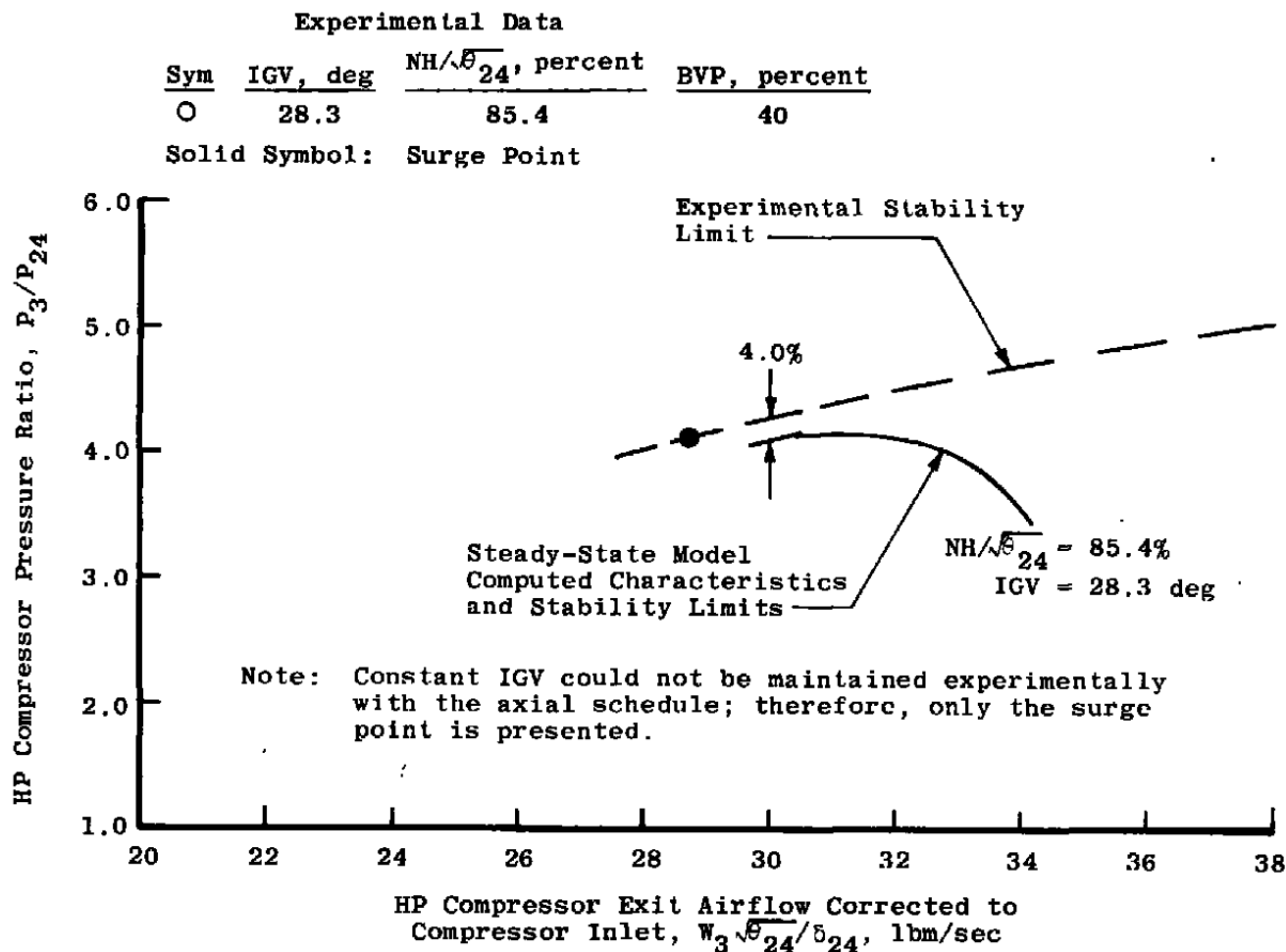
## Experimental Data

Sym	IGV, deg	$NH/\sqrt{\theta_{24}}$ , percent	BVP, percent
O	$34.0 \pm 2.0$	90.0 to 92.0	100

Solid Symbols: Surge Points



b. Cambered schedule  
Figure 17. Continued.

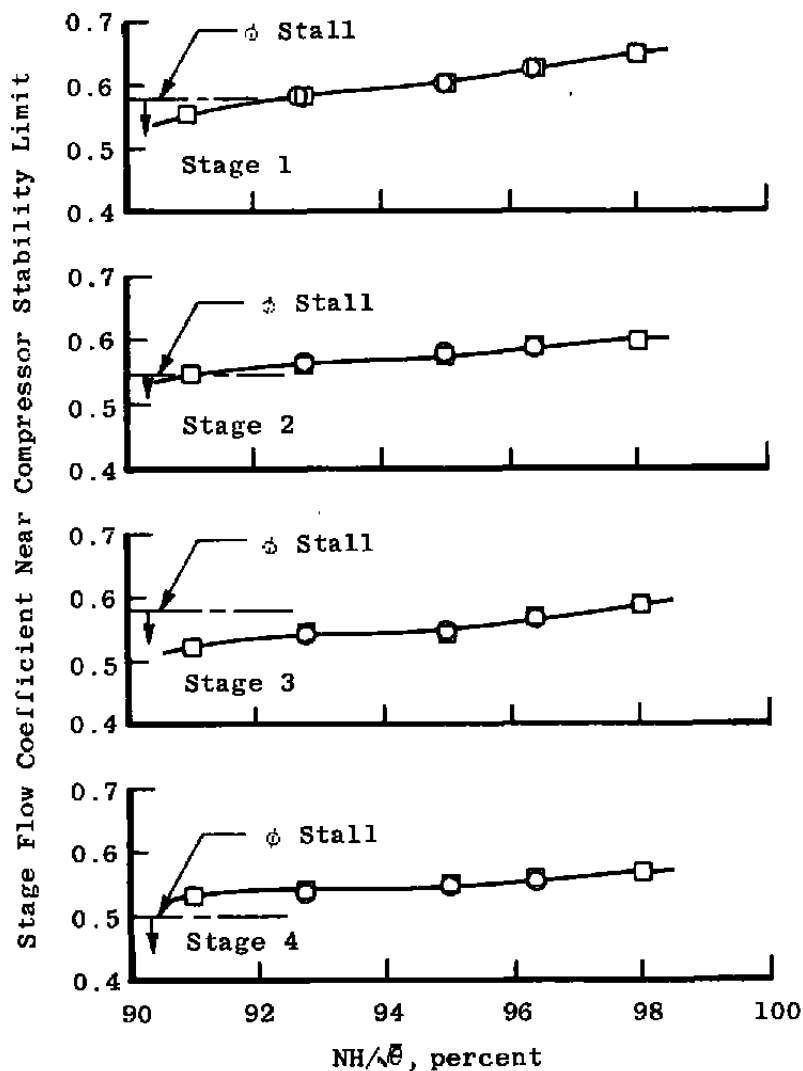


c. Axial schedule  
Figure 17. Concluded.

Altitude = 30,000 ft  
 Mach Number = 0.7  
 Axial IGV Schedule

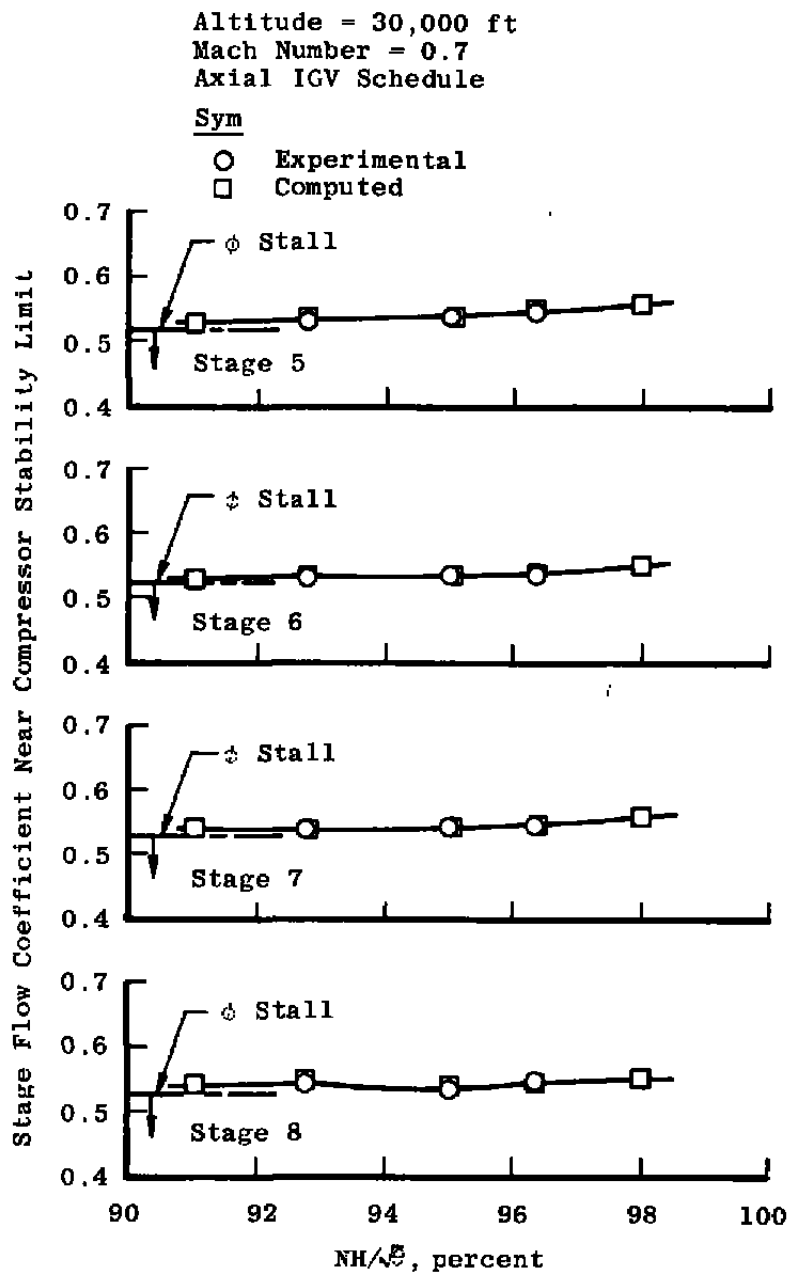
Sym

- Experimental Measurement  
 Nearest Surge Line  
 □ Computed

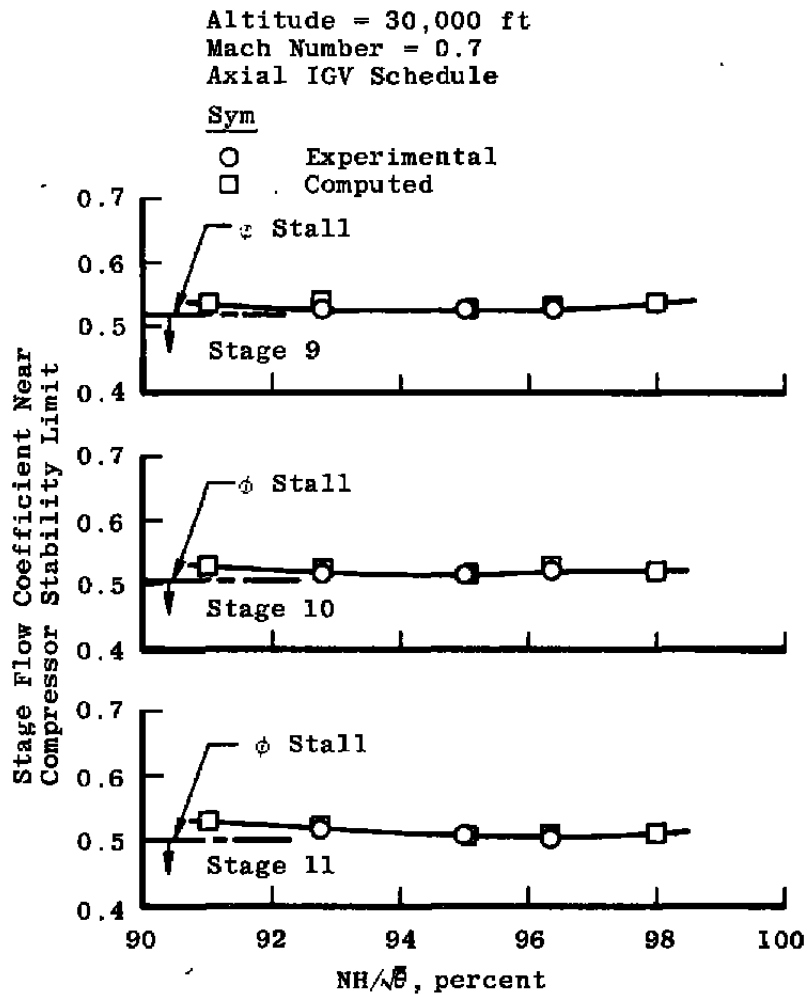


a. Stages 1 through 4

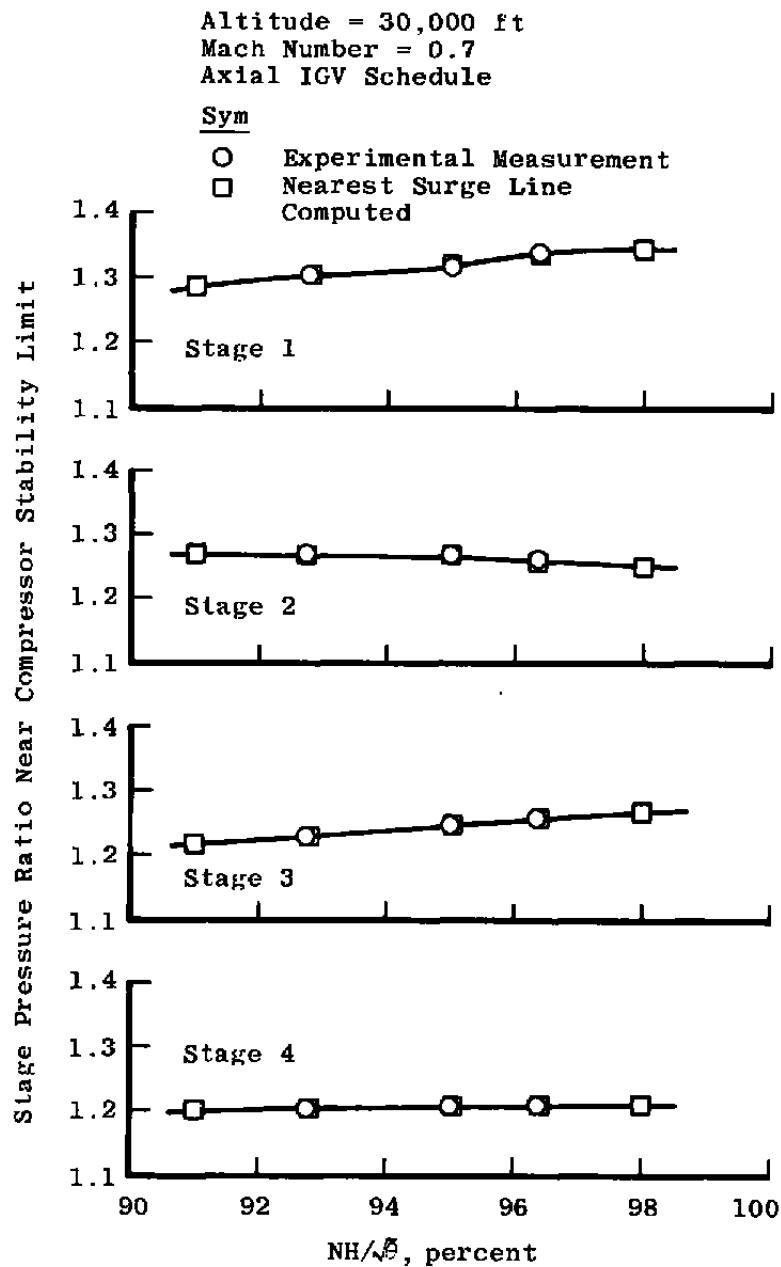
Figure 18. Comparison of model computed stage flow coefficients near compressor stability limit with experimental measurements, IGV at full axial position ( $-5.0 \pm 0.5$  deg).



b. Stages 5 through 8  
Figure 18. Continued.

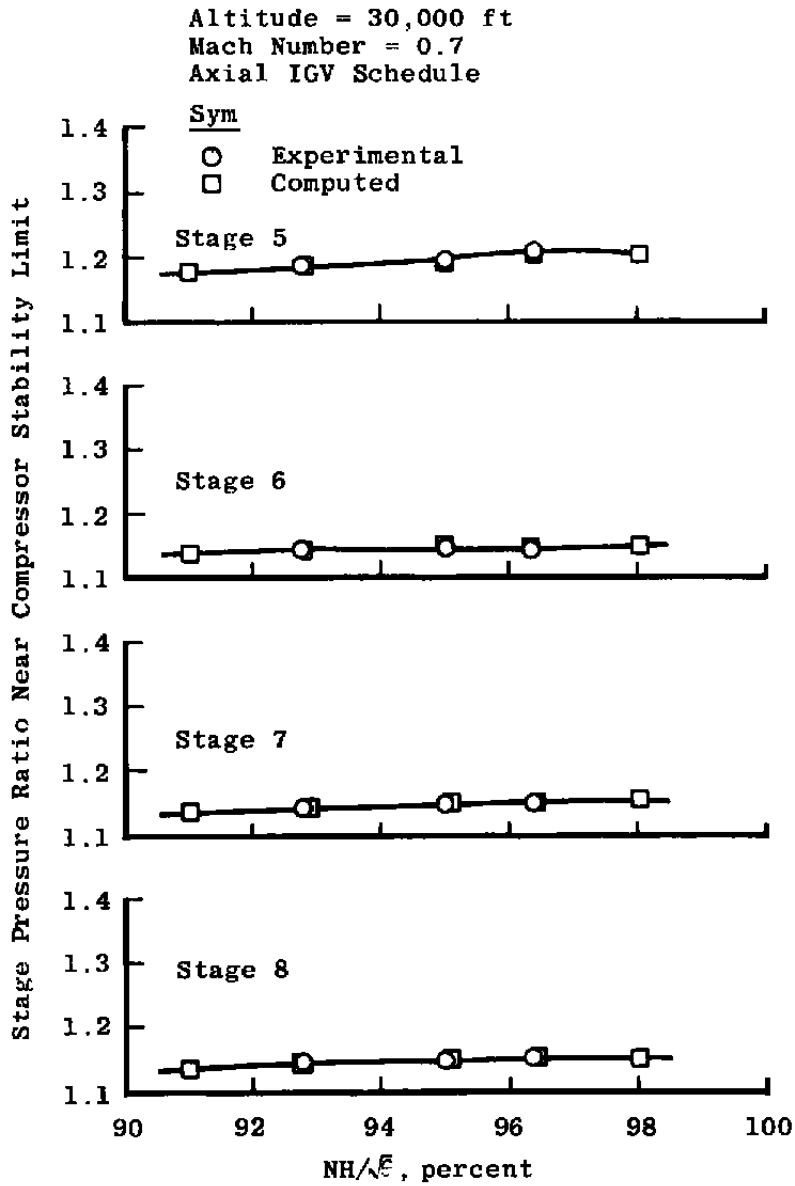


c. Stages 9 through 11  
Figure 18. Concluded.



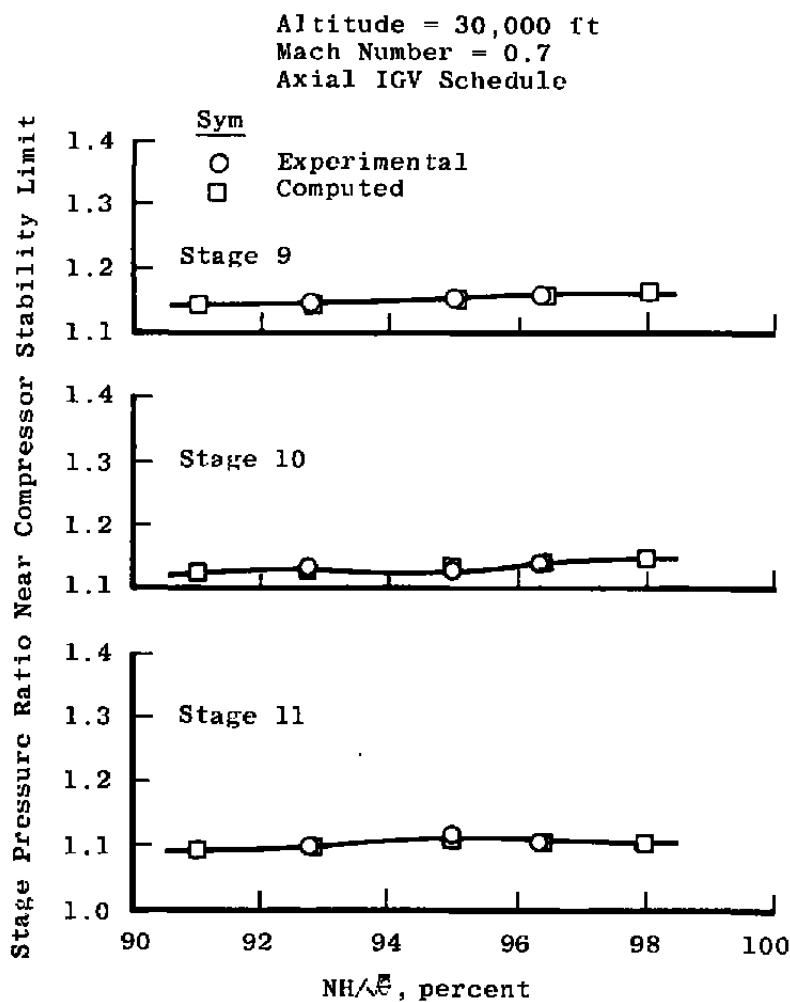
a. Stages 1 through 4

Figure 19. Comparison of model computed stage pressure ratios near compressor stability limit with experimental measurements, IGV at full axial position ( $-5.0 \pm 0.5$  deg).

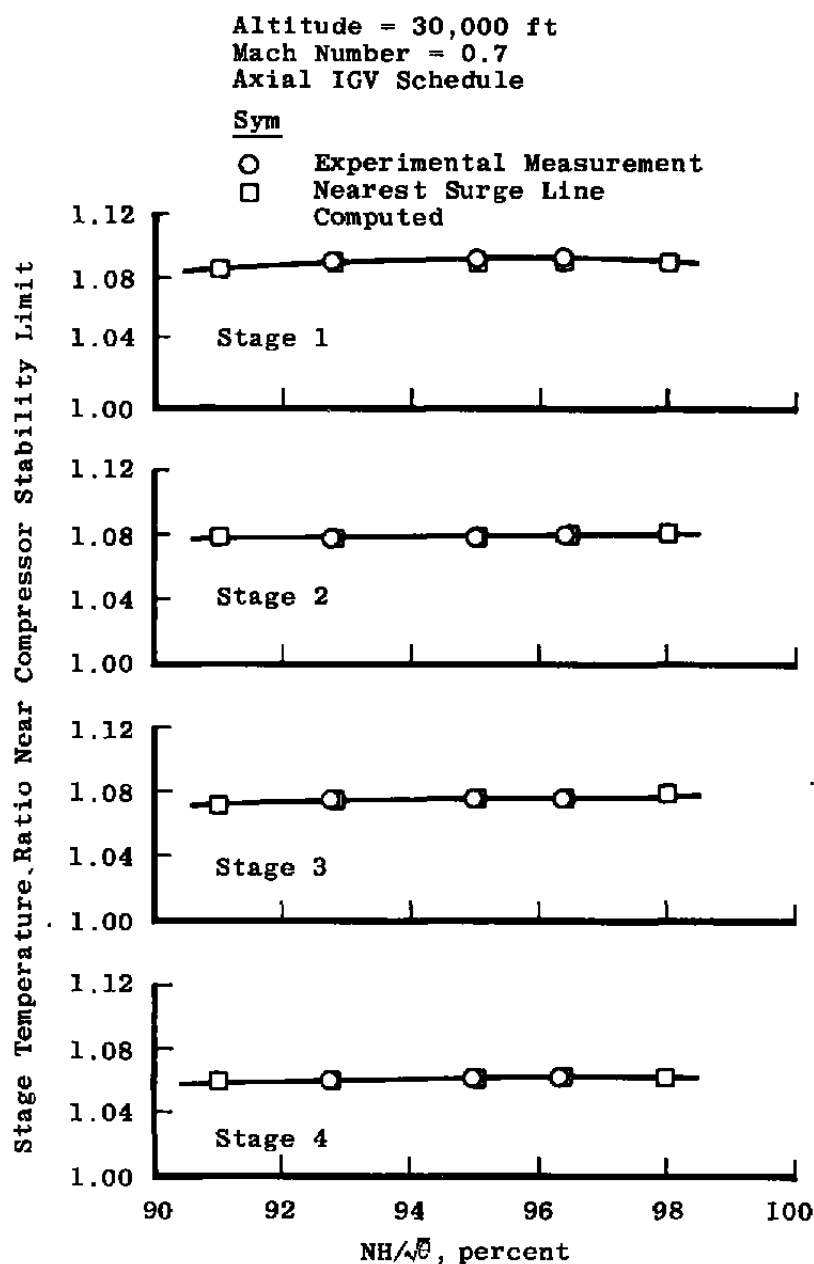


b. Stages 5 through 8  
Figure 19. Continued.



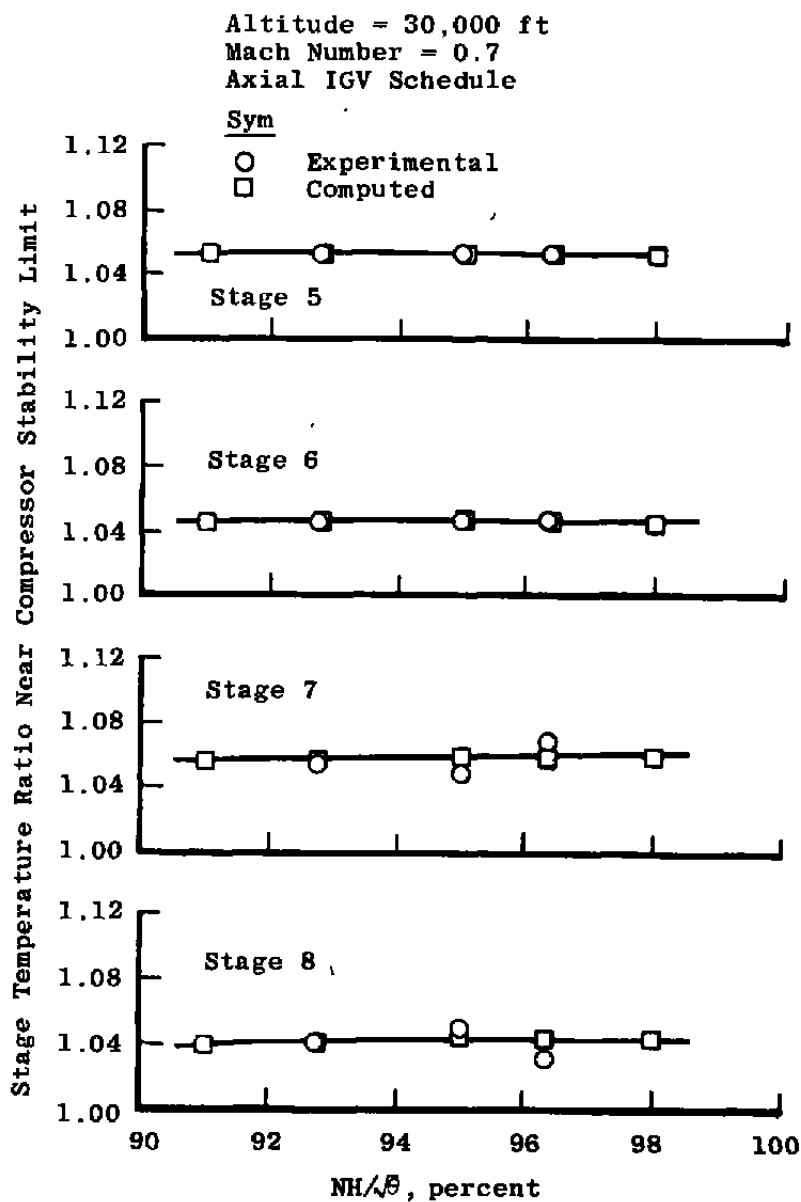


c. Stages 9 through 11  
Figure 19. Concluded.

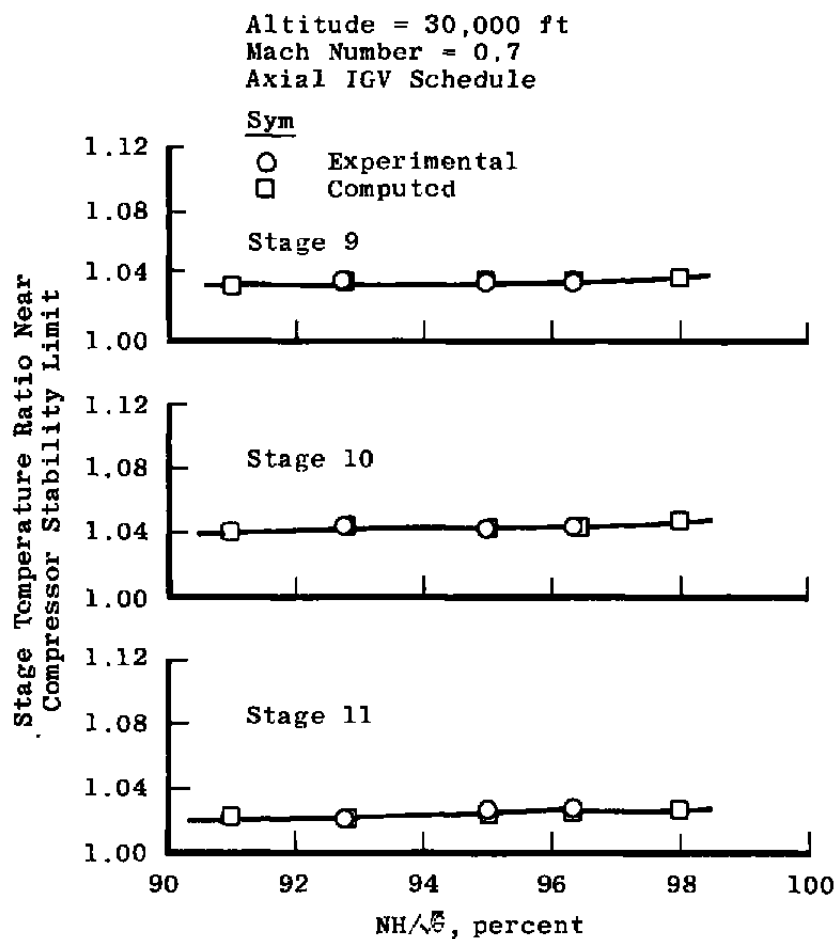


a. Stages 1 through 4

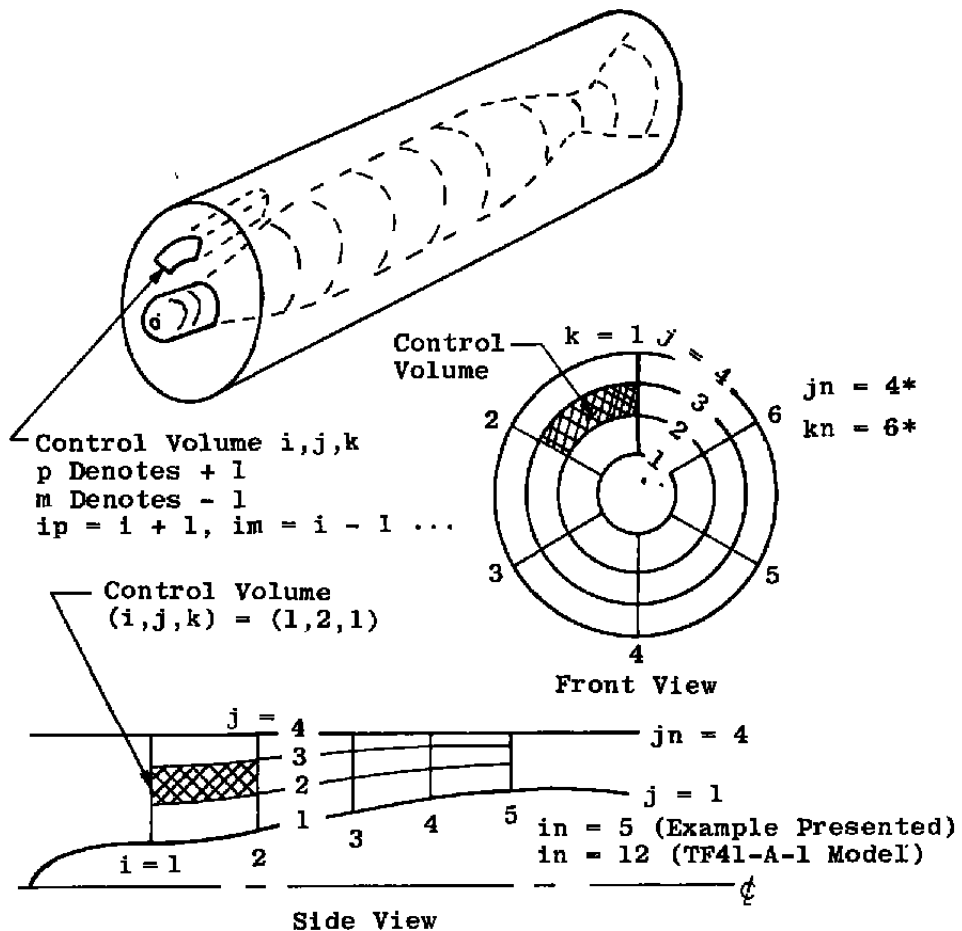
Figure 20. Comparison of model computed stage temperature ratios near compressor stability limit with experimental measurements, IGV at full axial position ( $-5.0 \pm 0.5$  deg).



b. Stages 5 through 8  
Figure 20. Continued.



c. Stages 9 through 11  
Figure 20. Concluded.



\* $j_n$  and  $k_n$  selection is on a case-by-case basis as required to define the distortion pattern under investigation.

Figure 21. Division of compressor into control volumes.

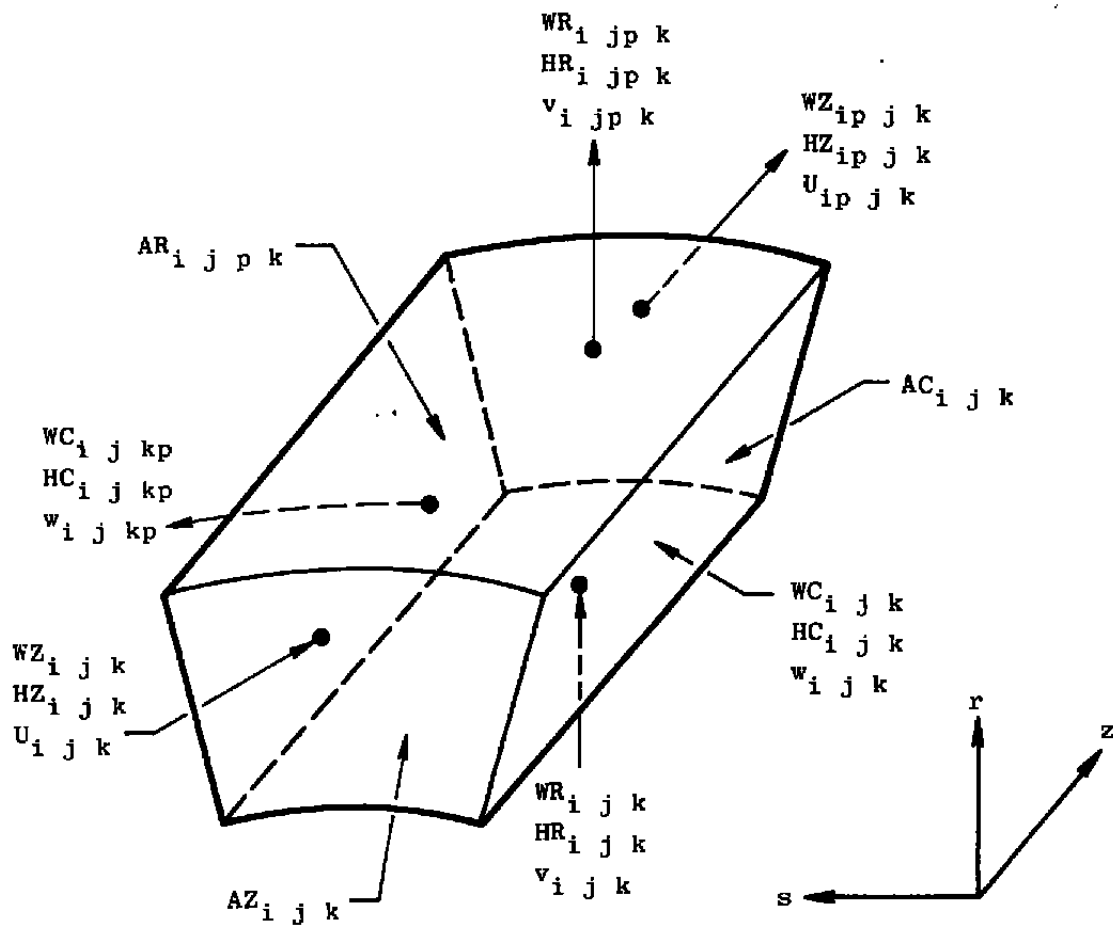


Figure 22. Control volume velocities and fluxes.

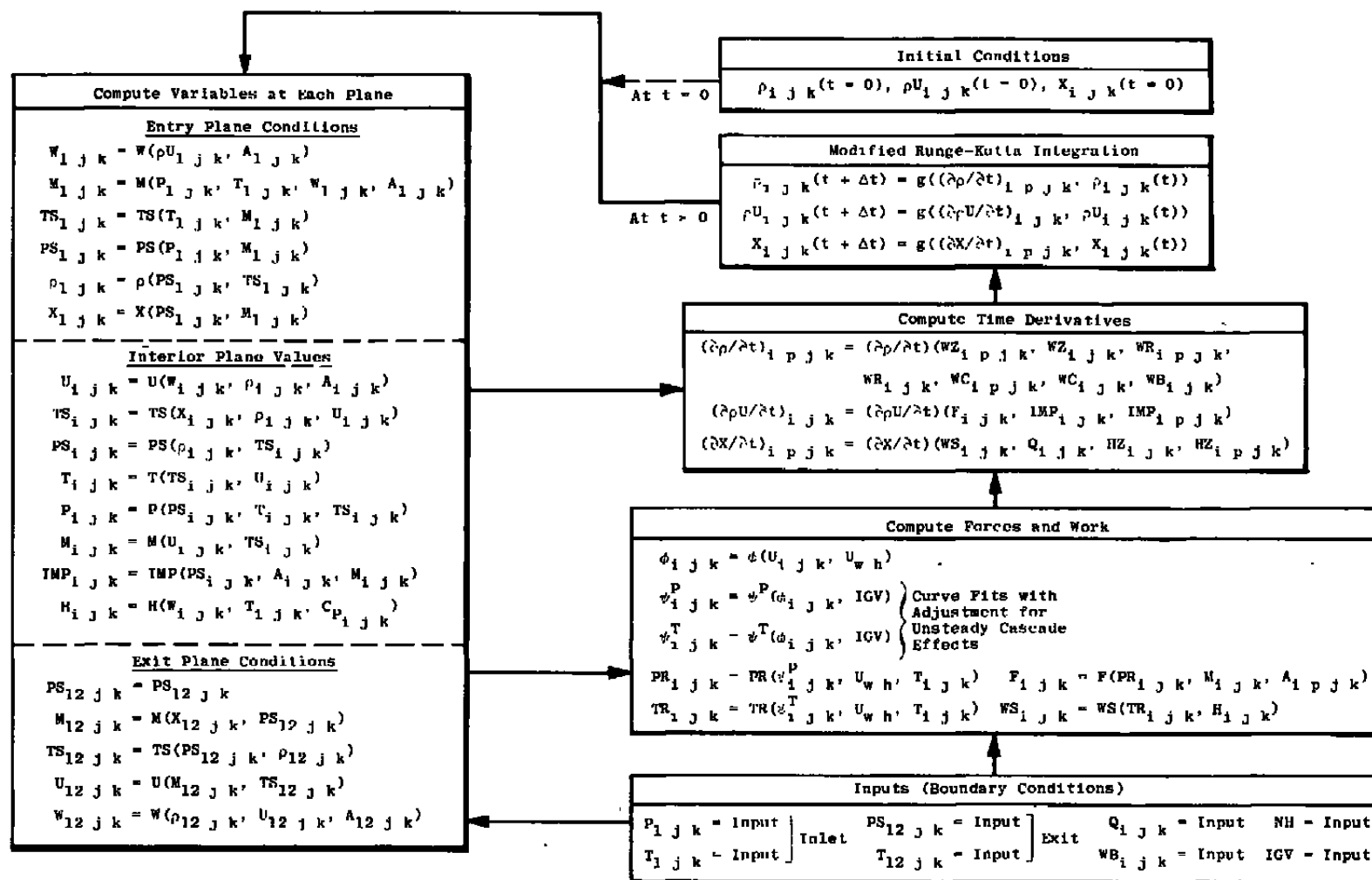


Figure 23. Schematic of three-dimensional, time-dependent solution procedure for TF41-A-1 HP compressor model.

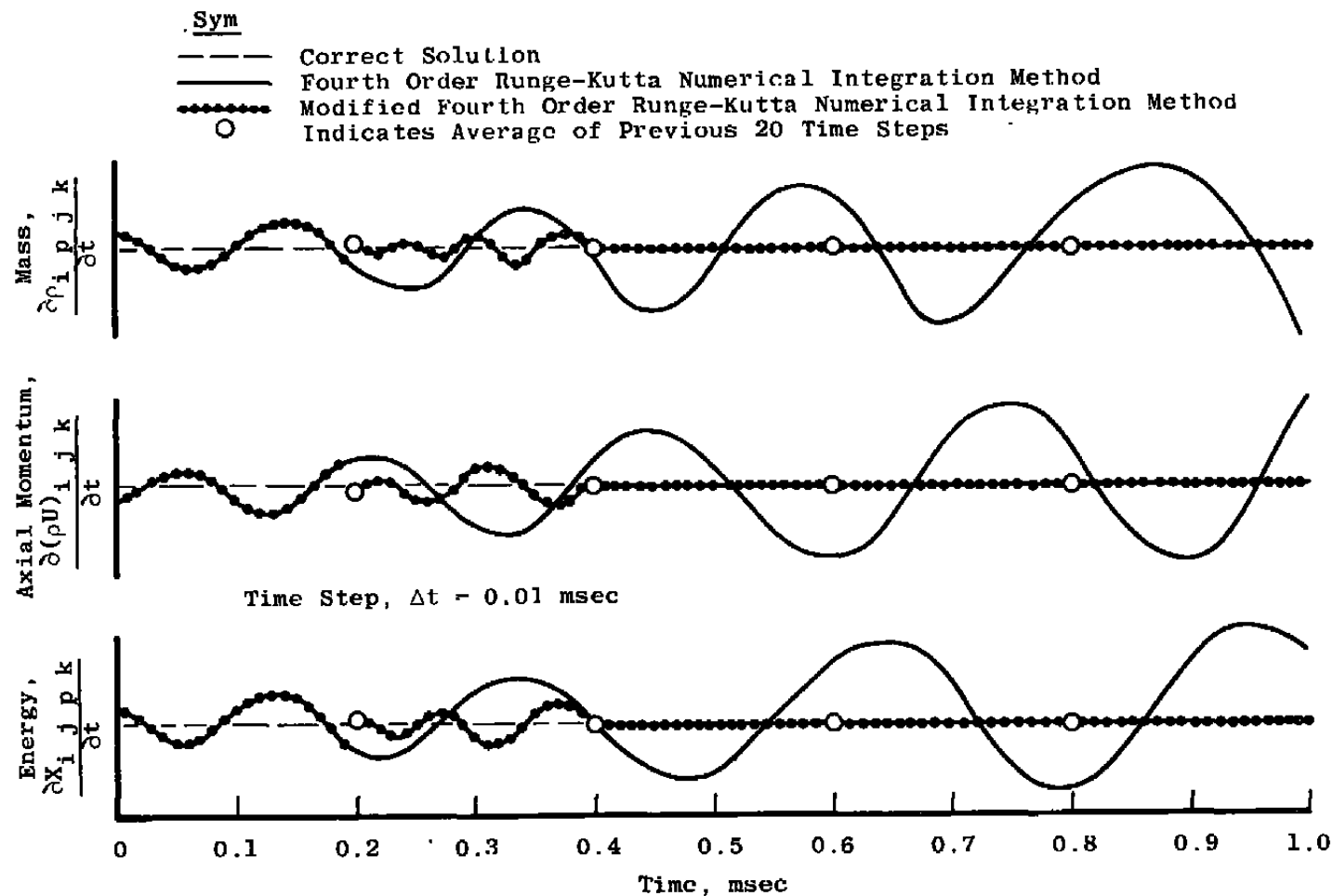


Figure 24. Illustration of effect of incremental averaging on numerical instability.



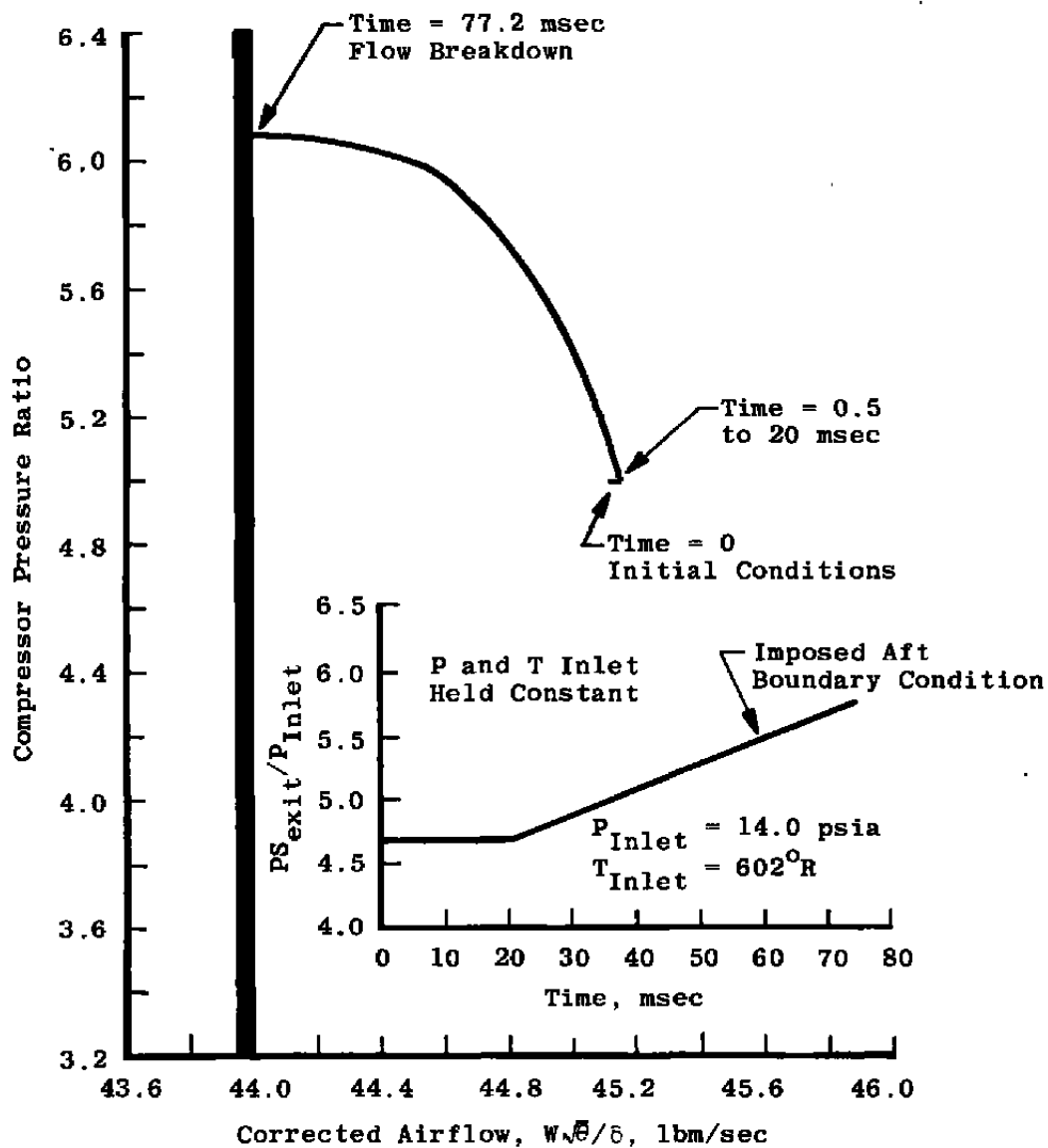


Figure 25. TF41-A-1 HP compressor model loaded to stall,  $NH/\sqrt{\theta} = 92.6$  percent, IGV = 12 deg, no distortion.

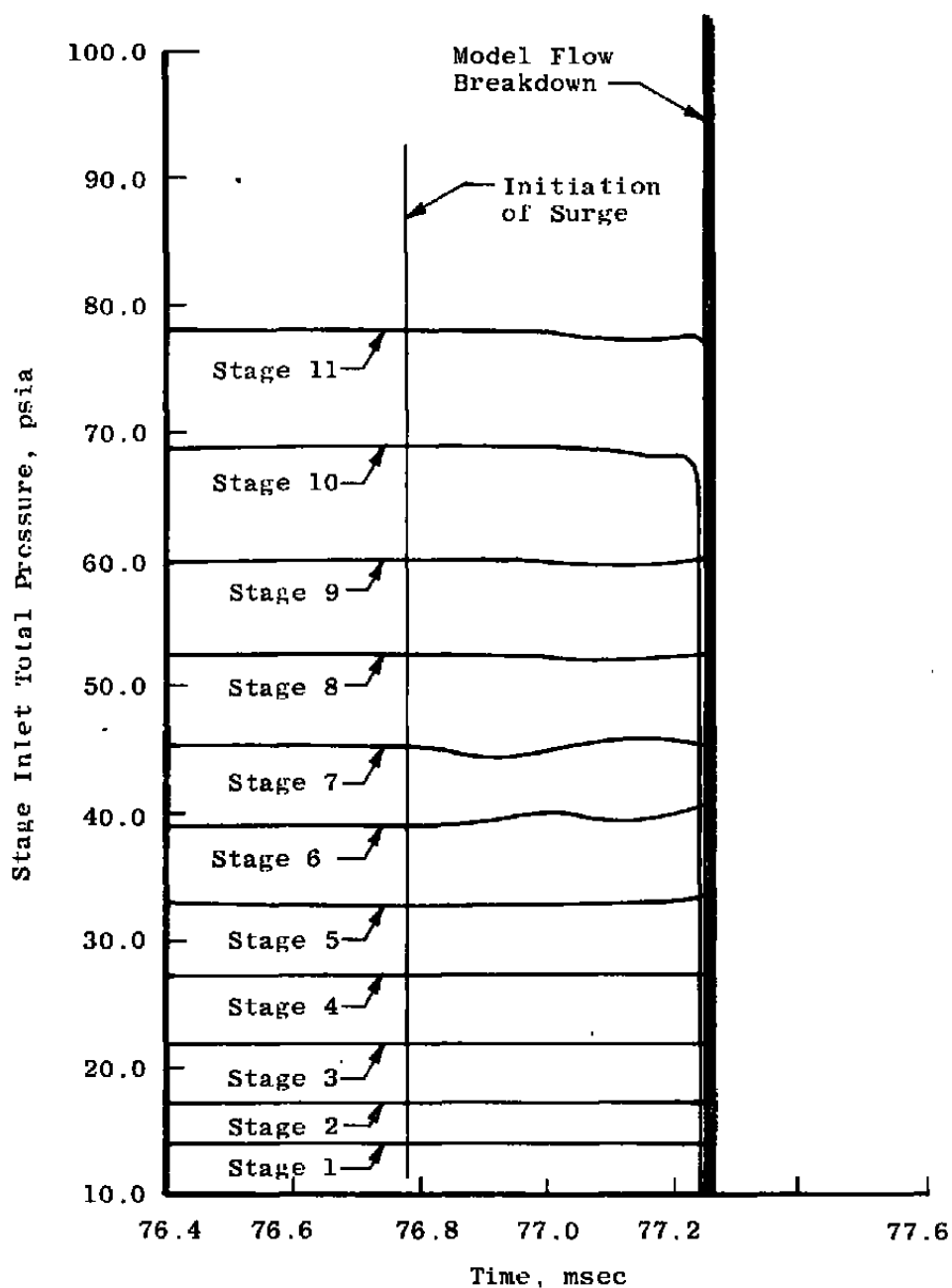
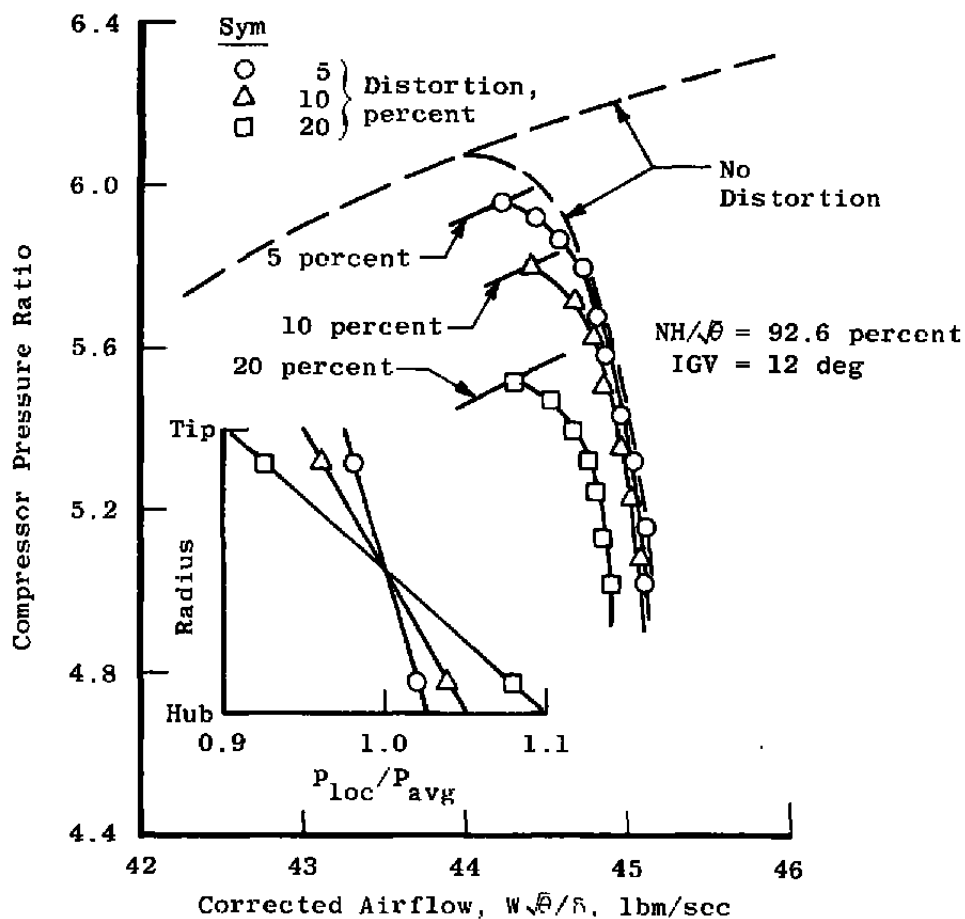
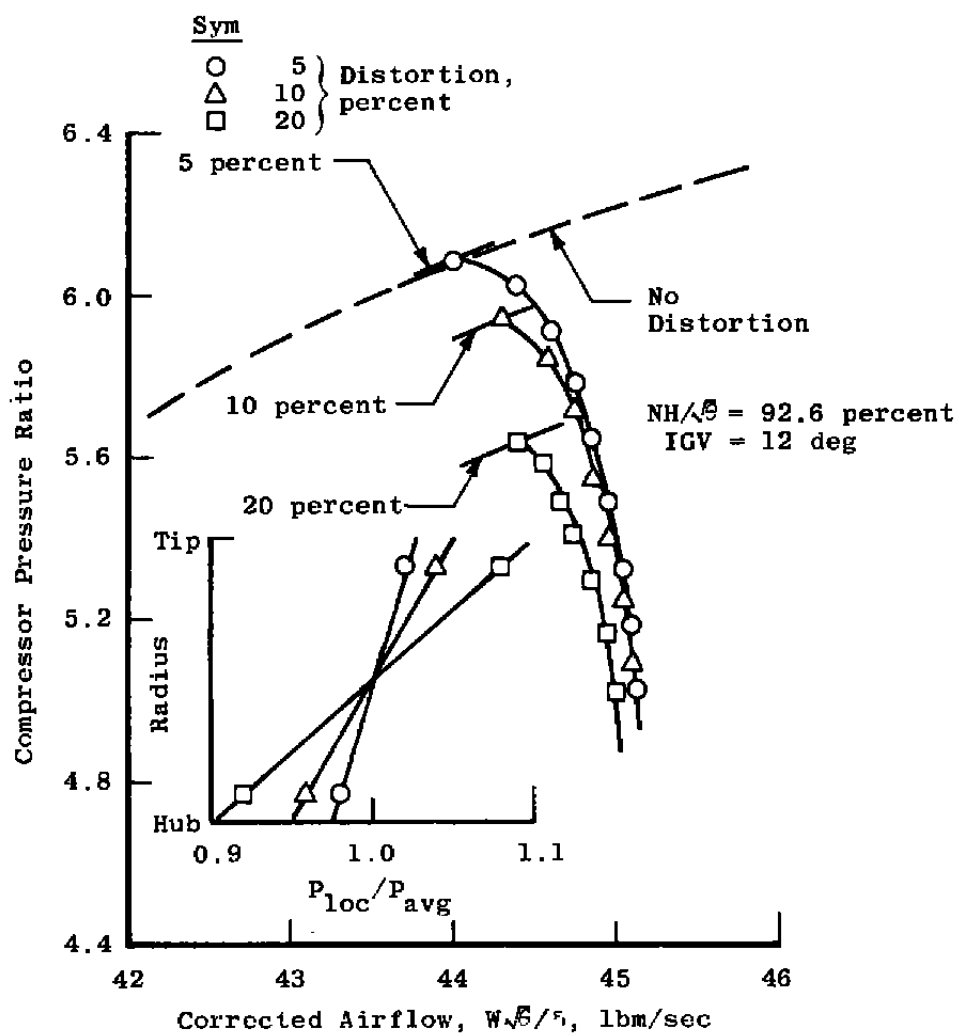


Figure 26. TF41-A-1 HP compressor model flow breakdown in terms of computed stage inlet total pressures leading to instability,  $NH/\sqrt{\theta} = 92.6$  percent, IGV = 12 deg, no distortion.

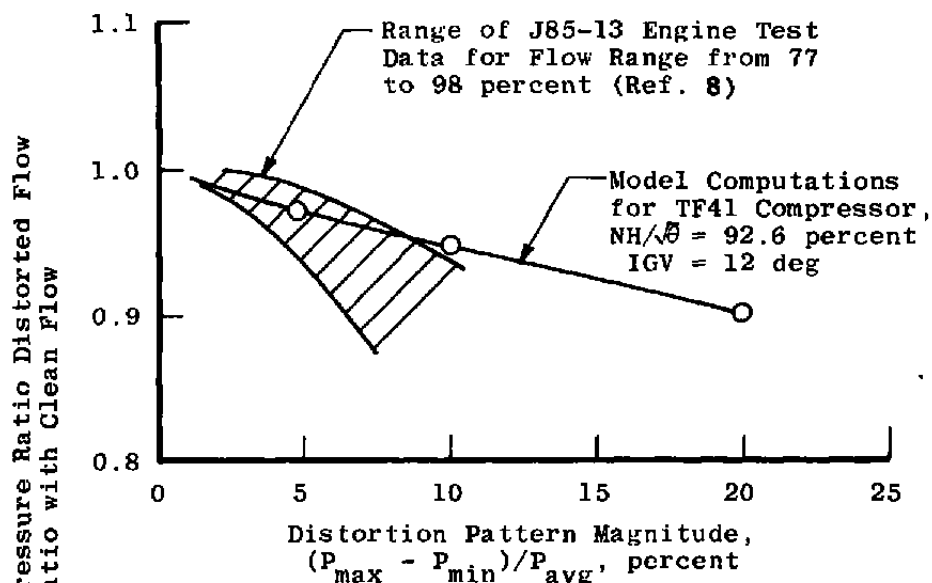


## a. Tip radial distortion

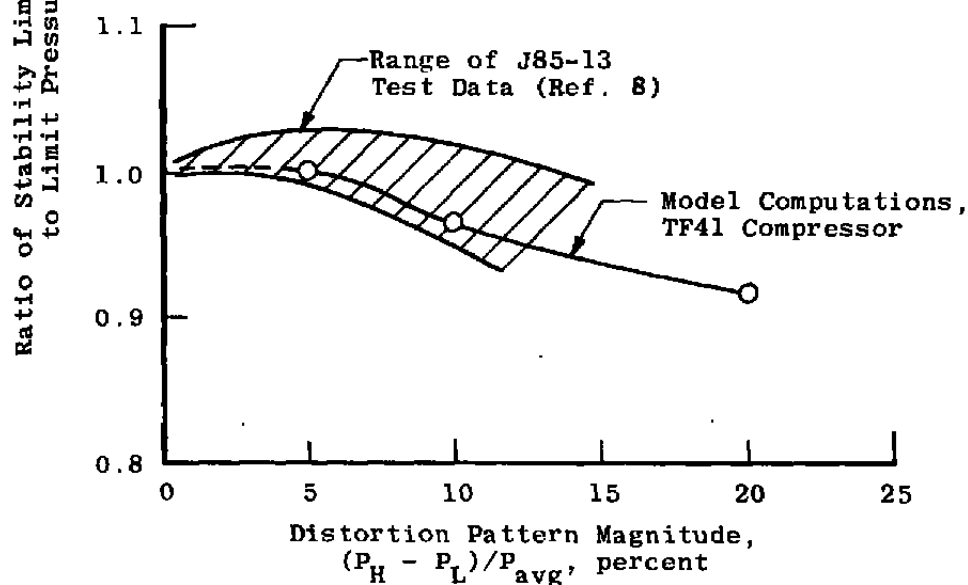
Figure 27. Computed radial distortion influences on stability, TF41-A-1 HP compressor.



b. Hub radial distortion  
 Figure 27. Concluded.



a. Tip radial distortion



b. Hub radial distortion

Figure 28. Comparison of TF41-A-1 HP compressor model radial distortion computations with experimental results.

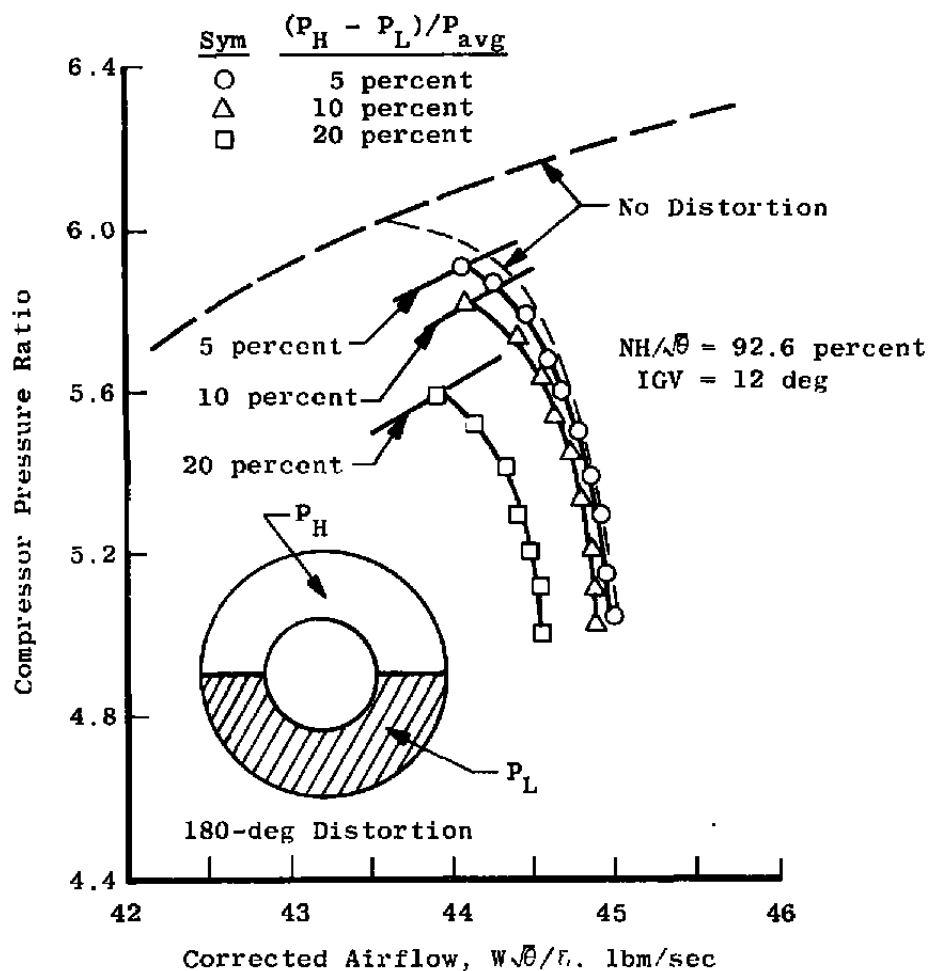


Figure 29. Model computed influence of circumferential pressure distortion on stability, TF41-A-1 HP compressor.

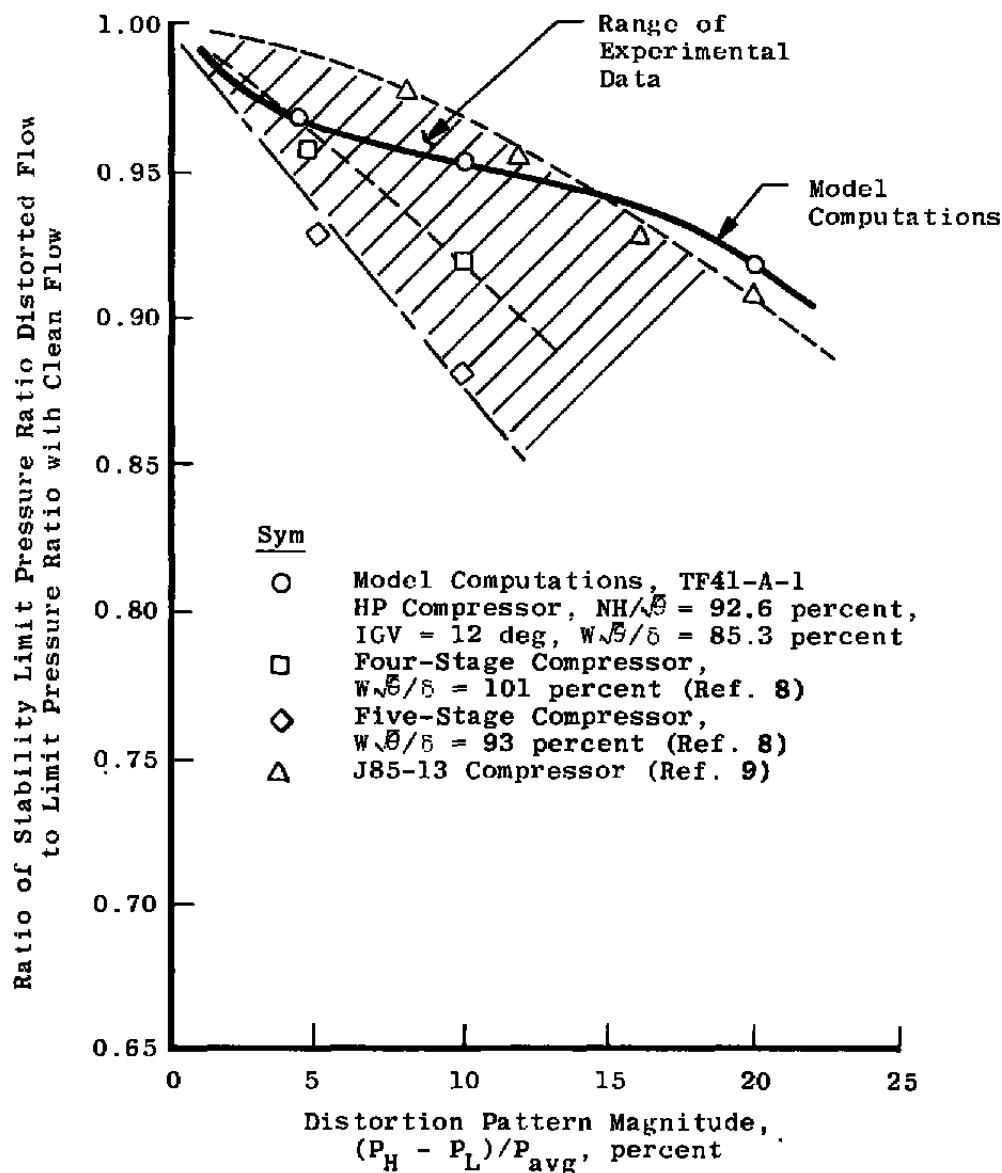


Figure 30. Comparison of TF41-A-1 HP compressor model circumferential distortion computations with experimental results.

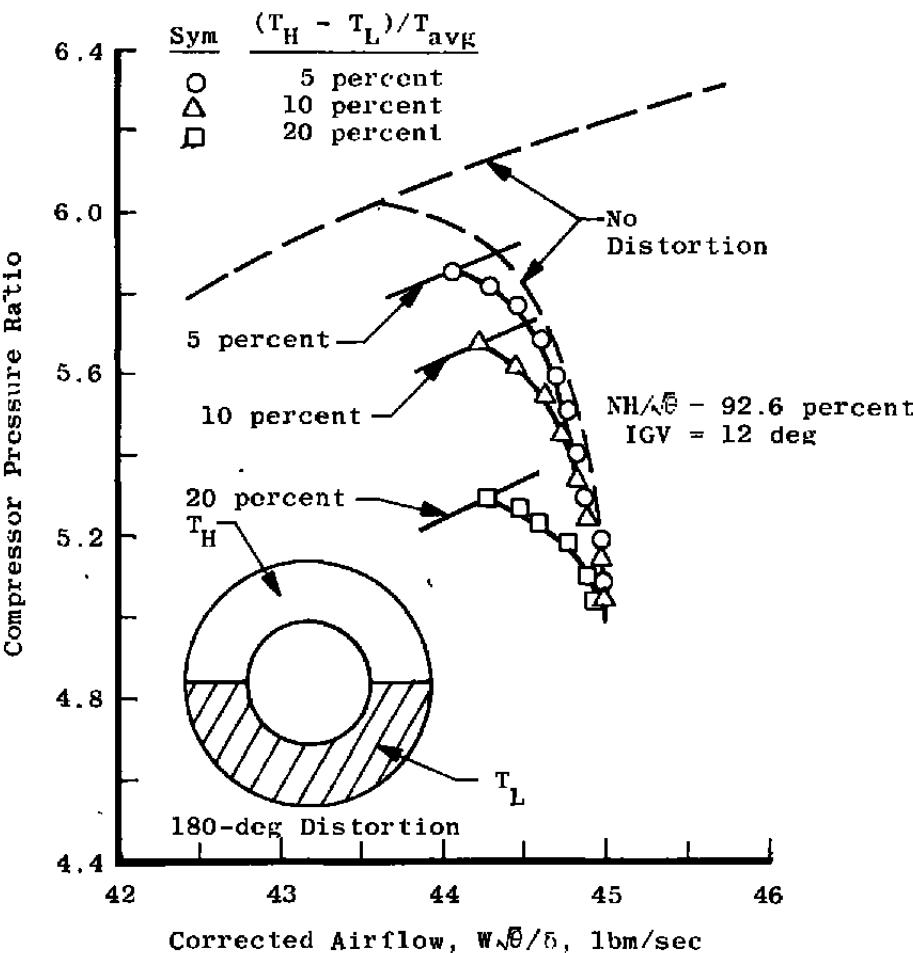


Figure 31. Model computed influence of circumferential temperature distortion on stability, TF41-A-1 HP compressor.



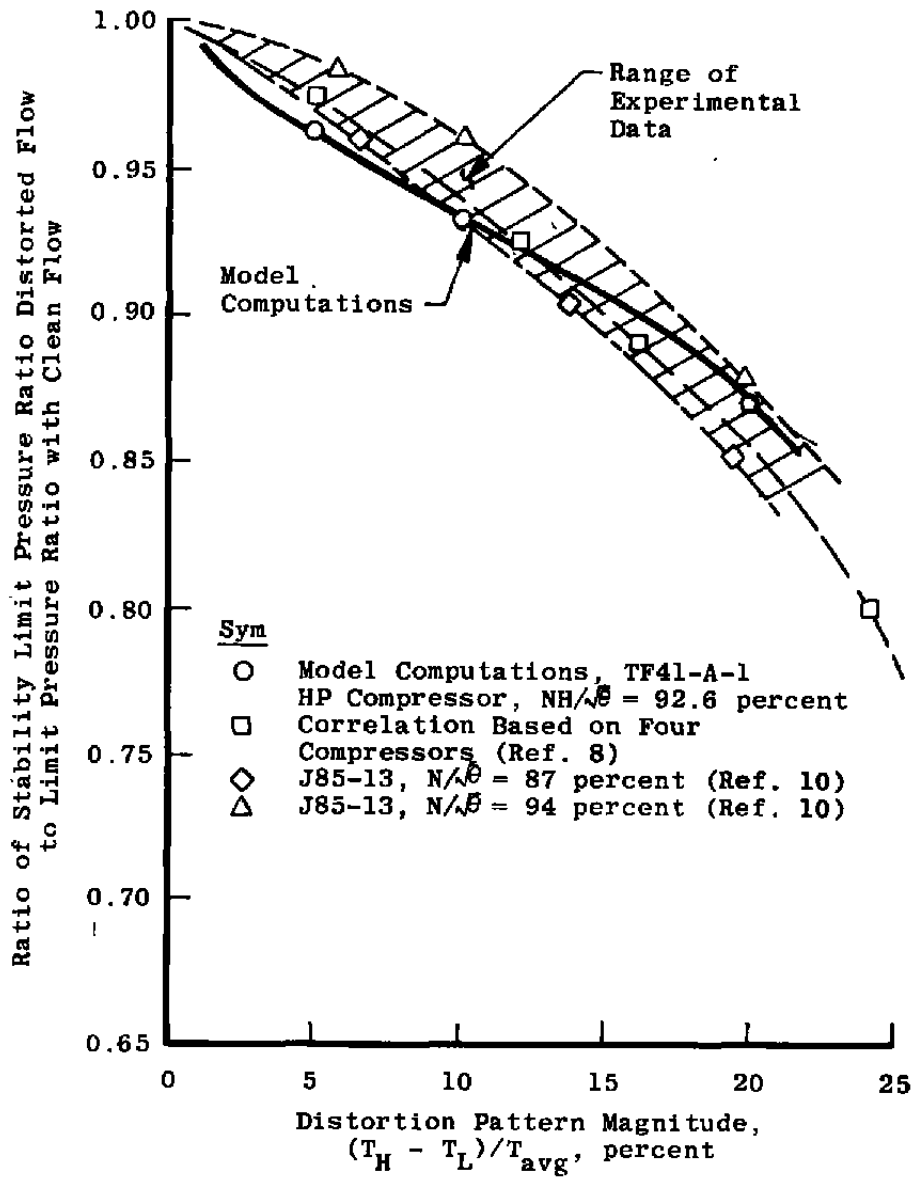


Figure 32. Comparison of circumferential temperature distortion model computations with experimental results.

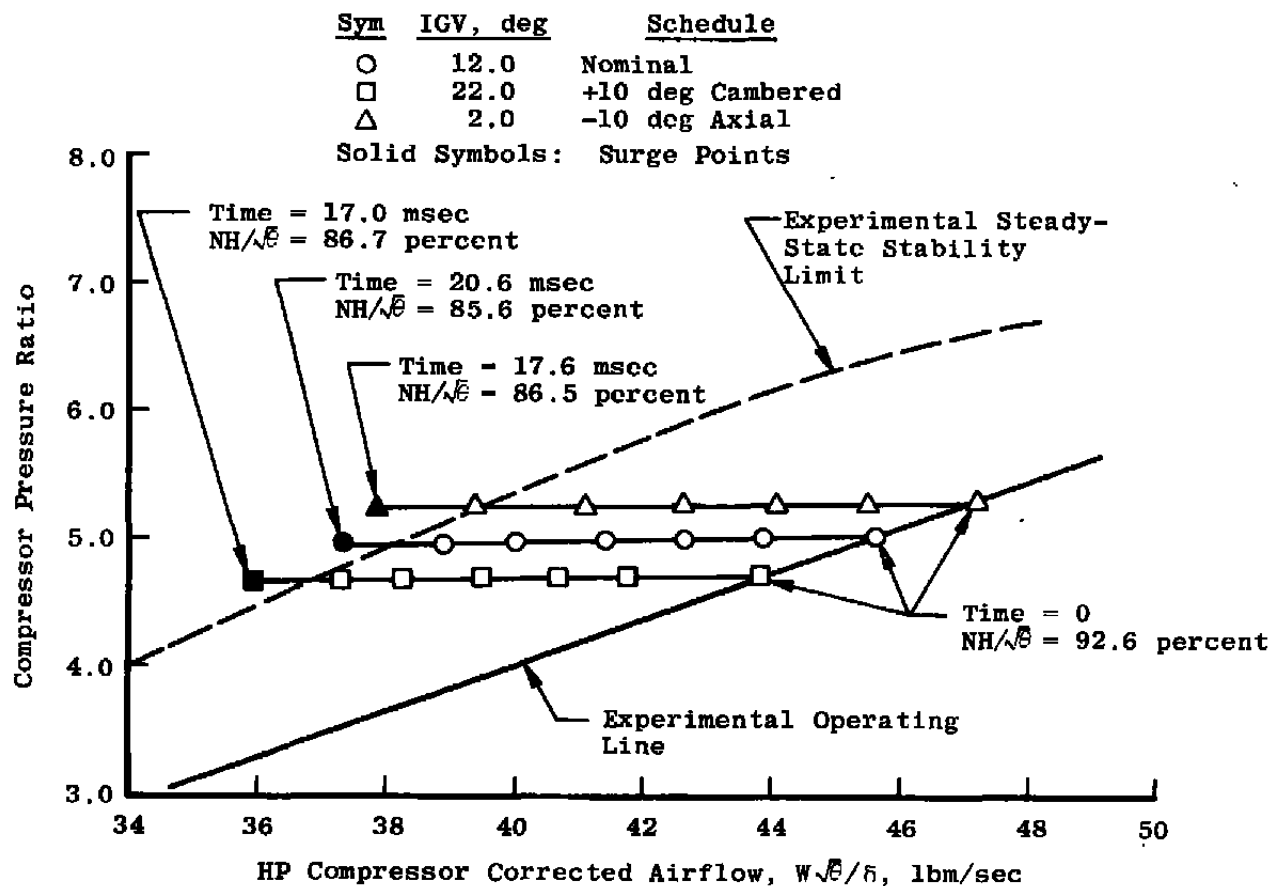


Figure 33. Effect of 5,000°R/sec uniform inlet temperature ramp on compressor stability as computed by TF41-A-1 HP compressor model.

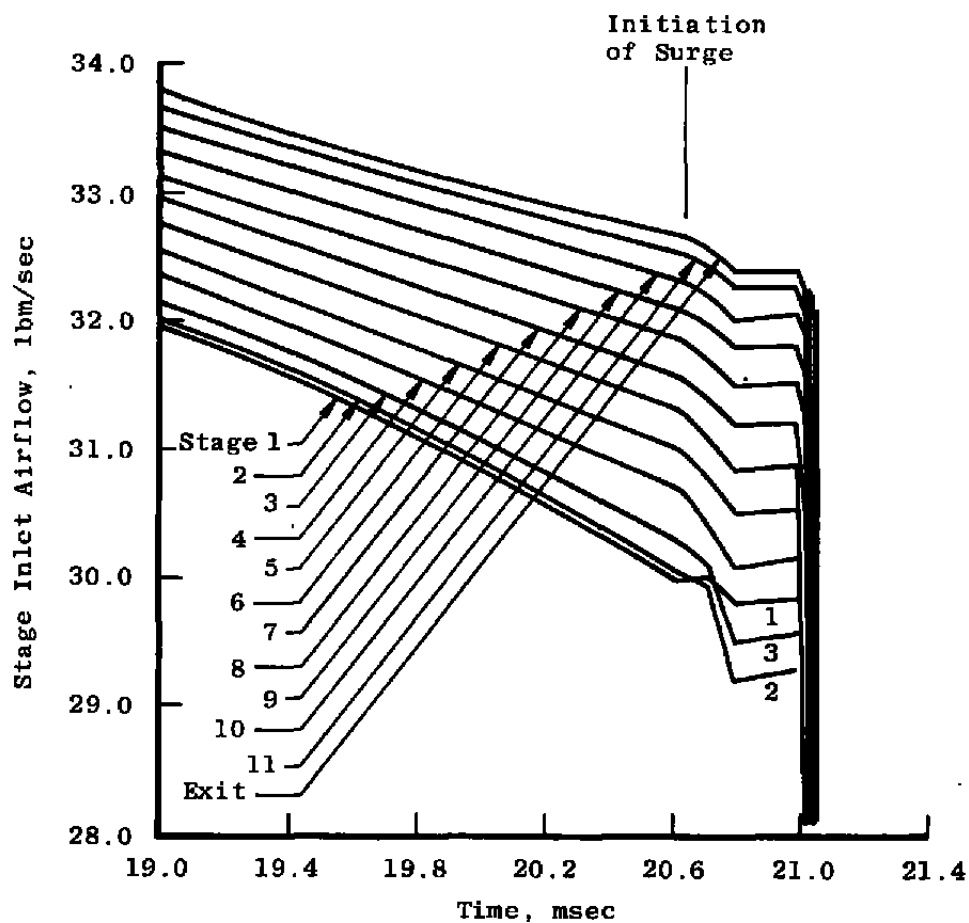


Figure 34. TF41-A-1 HP compressor model flow breakdown with 5,000°R/sec inlet temperature ramp, nominal IGV schedule, no distortion.

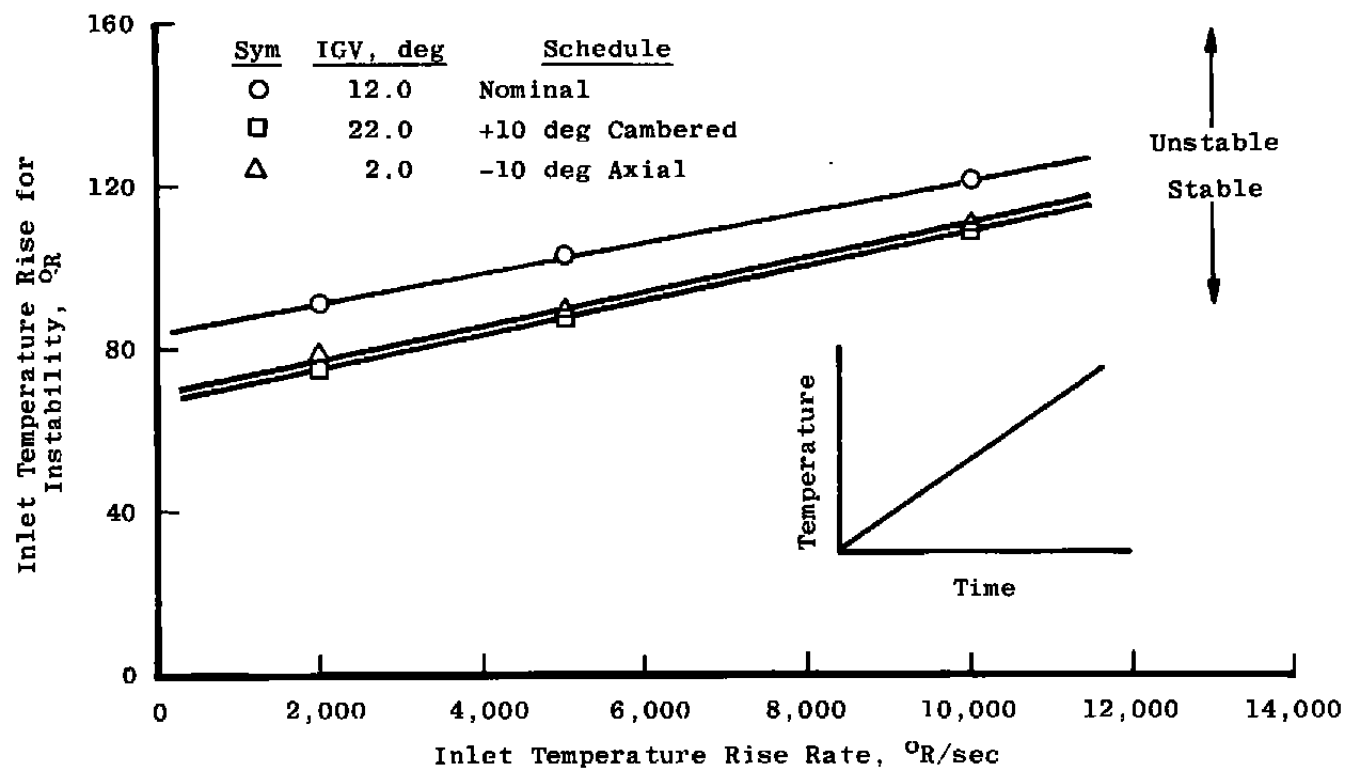


Figure 35. TF41-A-1 HP compressor model computed influence of uniform inlet temperature ramp rates on compressor stability.

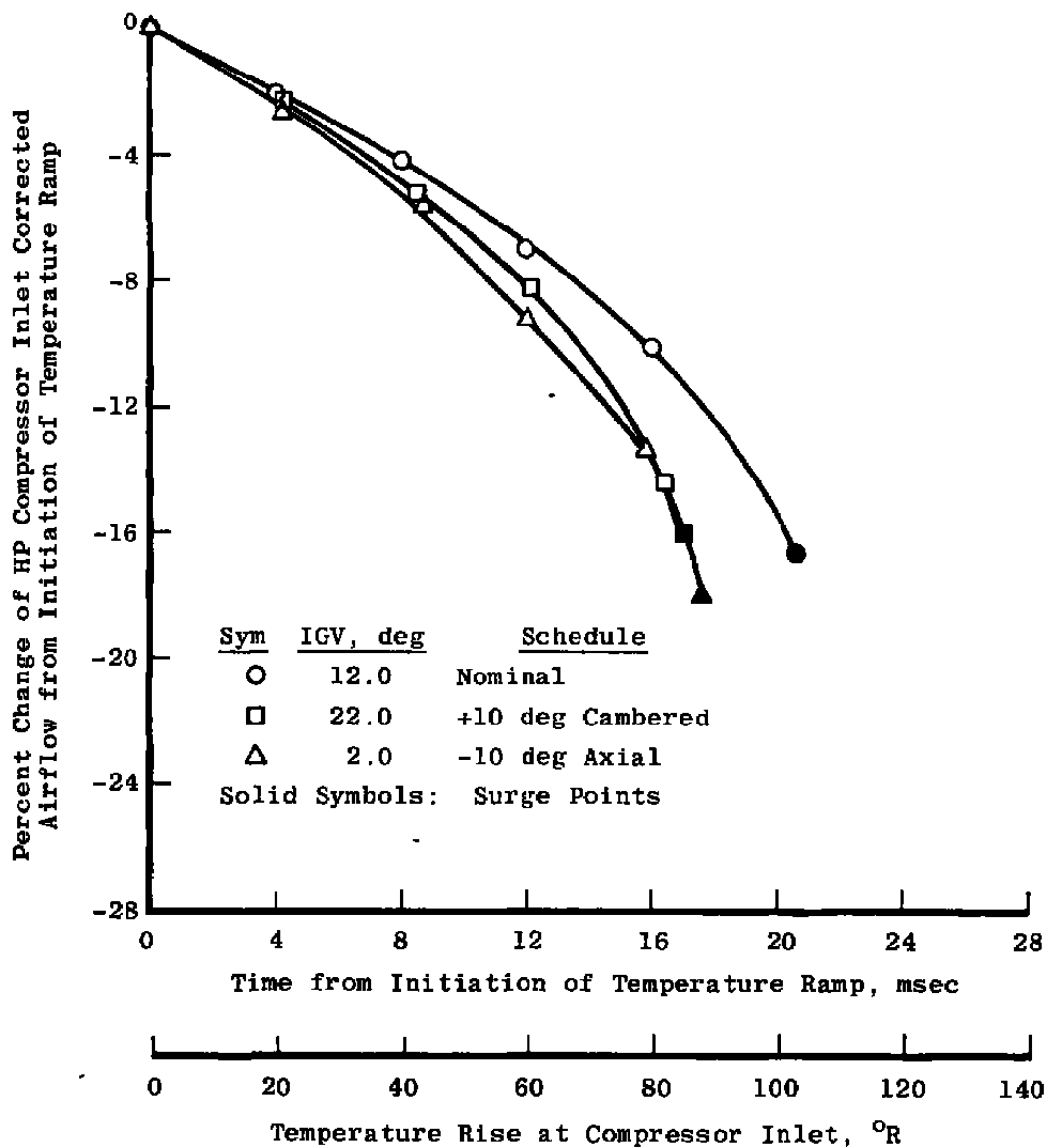


Figure 36. Effect of 5,000°R/sec uniform inlet temperature ramp on compressor inlet corrected airflow as computed by TF41-A-1 HP compressor model.

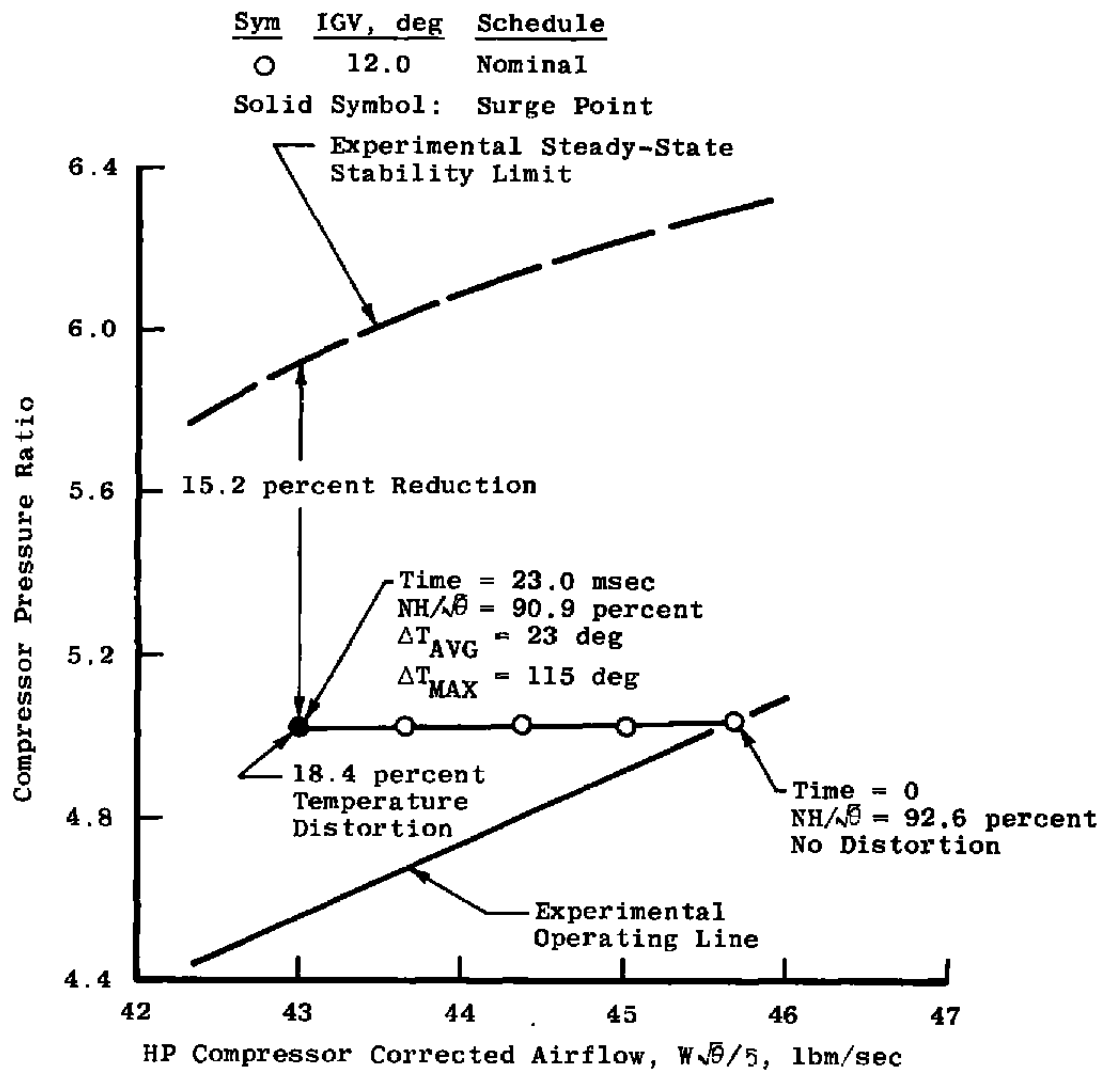


Figure 37. Effect of 5,000°R/sec inlet temperature ramp (imposed on 90-deg-arc circumferential section) on compressor stability as computed by TF41-A-1 compressor model.

## NOMENCLATURE

<b>A</b>	<b>Area</b>
<b>A<sub>z</sub></b>	<b>Control volume area normal to axial direction</b>
<b>a</b>	<b>Acoustic velocity</b>
<b>BVP</b>	<b>Bleed valve position</b>
<b>C<sub>d</sub></b>	<b>Duct pressure loss friction coefficient</b>
<b>C<sub>p</sub></b>	<b>Specific heat at constant pressure</b>
<b>C<sub>v</sub></b>	<b>Specific heat at constant volume</b>
<b>e</b>	<b>Internal energy</b>
<b>F</b>	<b>Force of compressor blading and cases acting on fluid, including wall pressure area force</b>
<b>f (...)</b>	<b>A function of ...</b>
<b>g (...)</b>	<b>A function of ...</b>
<b>H</b>	<b>Total enthalpy flux</b>
<b>HC</b>	<b>Total enthalpy flux transported across control volume circumferentially-facing boundary</b>
<b>HP</b>	<b>High-pressure rotor</b>
<b>HR</b>	<b>Total enthalpy flux transported across control volume radially-facing boundary</b>
<b>HZ</b>	<b>Total enthalpy flux transported across control volume axial-facing boundary</b>
<b>IGV</b>	<b>Inlet guide vane</b>
<b>IMP</b>	<b>Impulse function</b>
<b>IMPR</b>	<b>Ratio of stage exit to stage entry impulse functions</b>
<b>i</b>	<b>Axial location index</b>

<b>ip</b>	<b>Adjacent axial location, <math>i + 1</math></b>
<b>J</b>	<b>Mechanical equivalent of heat</b>
<b>j</b>	<b>Radial location index</b>
<b>jp</b>	<b>Adjacent radial location, <math>j + 1</math></b>
<b>k</b>	<b>Circumferential location index</b>
<b>kp</b>	<b>Adjacent circumferential location, <math>k + 1</math></b>
<b>M</b>	<b>Mach number</b>
<b>N</b>	<b>Compressor rotor speed</b>
<b>NH</b>	<b>High-pressure compressor rotor speed</b>
<b>NL</b>	<b>Low-pressure compressor rotor speed</b>
<b>P</b>	<b>Stagnation (total) pressure</b>
<b>PD</b>	<b>Dynamic pressure measurement</b>
<b>PR</b>	<b>Stage total pressure ratio</b>
<b>PS</b>	<b>Static pressure</b>
<b>Q</b>	<b>Rate of heat addition to control volume</b>
<b>R</b>	<b>Gas constant</b>
<b>r</b>	<b>Radius; coordinate in the radial direction</b>
<b>s</b>	<b>Coordinate in the circumferential direction</b>
<b>T</b>	<b>Stagnation (total) temperature</b>
<b>TR</b>	<b>Stage total temperature ratio</b>
<b>TS</b>	<b>Static temperature</b>
<b>t</b>	<b>Time</b>
<b>U</b>	<b>Axial velocity</b>



<b>v</b>	Radial velocity component in three-dimensional model development
<b>vol</b>	Volume
<b>W</b>	Mass flow rate; airflow rate
<b>WB</b>	Compressor bleed flow rate
<b>WC</b>	Mass flux across circumferentially-facing control volume boundary
<b>WR</b>	Mass flux across radially-facing control volume boundary
<b>WS</b>	Stage shaft work added to fluid in control volume
<b>WZ</b>	Mass flux across axially-facing control volume boundary
<b>w</b>	Circumferential velocity component in three-dimensional model development
<b>X</b>	Energy function
<b>z</b>	Axial coordinate

#### **GREEK SYMBOLS**

<b><math>\alpha</math></b>	Angle of attack
<b><math>\beta</math></b>	Flow direction angle relative to axial direction
<b><math>\gamma</math></b>	Ratio of specific heats
<b><math>\Delta</math></b>	A difference
<b><math>\delta</math></b>	Ratio of compressor entry total pressure to standard day, sea-level-static pressure
<b><math>\theta</math></b>	Ratio of compressor inlet total temperature to standard day, sea-level-static temperature
<b><math>\lambda</math></b>	Blade chord-to-axial direction angle or stagger angle
<b><math>\rho</math></b>	Density
<b><math>\phi</math></b>	Stage flow coefficient

$\psi^P$	Stage pressure coefficient
$\psi^T$	Stage temperature coefficient (stage loading parameter)

## **SUPERSCRIPTS**

<b>P</b>	Pertaining to pressure
<b>T</b>	Pertaining to temperature

## **SUBSCRIPTS**

0,1,2 ...	Location or station designators
avg	Average value
exit	Pertaining to compressor exit plane
H	High
i	Axial location index
ijk	Three-dimensional location index, refers to value at location, i, j, k
ip	Adjacent axial location, i + 1
j	Radial location index
jp	Adjacent radial location, j + 1
k	Circumferential location index
kp	Adjacent circumferential location, k + 1
L	Low
loc	Local value
max	Maximum value
min	Minimum value
n	Last location, e.g., last axial location in control volume
p	Plus one

radial avg	Average value along a radius
ring avg	Average value along a circle, average at constant radius
wh	Wheel
z	Axial component